The University of Southampton
School of Engineering Sciences
Astronautics Research Group

"Development of a Reusable Atomic Oxygen Sensor using Zinc Oxide Thick Films"

Thesis submitted for Doctor of Philosophy

By

Juan Carlos Valer

August 2009

AD ASTRA PER ASPERA
(A ROUGH ROAD LEADS TO THE STARS)

Taken from the Memorial Plaque in
honor of the astronauts who lost
their lives on the fire of Apollo I,
Kennedy Space Center, Florida, USA.

UNIVERSITY OF SOUTHAMPTON

ABSTRACT

FACULTY OF ENGINEERING AND APPLIED SCIENCE
SCHOOL OF ENGINEERING SCIENCES (ASTRONAUTICS)

Doctor of Philosophy

DEVELOPMENT OF A REUSABLE ATOMIX OXYGEN SENSOR USING ZINC OXIDE THICK FILMS

by Juan Carlos Valer

The aim of this project was to develop a thick film sensor made of zinc oxide that would accurately respond to various fluxes of atomic oxygen (AO), allowing it to be regenerated after saturation. The sensors were manufactured using a thick film technique of screen printing over a substrate (alumina) that is inert to the action of AO; some of sensors were developed with pure ZnO while others used a binder to the substrate. The expectation has been that impinging atomic oxygen is captured upon the zinc oxide which will consequently increase its resistance; this change is an indicator of the AO flux. By suitable heating, the adsorbed atomic oxygen atoms are released from the sensor and its original properties are then restored.

This thesis describes the manufacturing of the sensors as well as all the tests conducted so as to characterize and determine the performance of the thick film ZnO sensors. It also includes the relevant conclusions to this work.

It has been concluded that the sensors respond to AO by increasing the overall DC resistance of the sensors; impedance spectroscopy reveals that an increase of the resistance of the grain boundaries of the crystallites that make-up the sensors to be the dominant process. AO flux can be measured by both resistance and impedance spectroscopy measurements. Sensors can be regenerated by suitable heating. However, each sensor needs to be independently calibrated before AO measurements can be achieved. A model to relate the change of DC conductance with AO flux is described, as well as an adaptation to use with impedance spectroscopy. UV radiation does not seem to have an effect on the resistance of the sensors, despite evidence provided by other researchers.

This is the first time that thick film ZnO sensors have been used to measure AO flux, and also the first time that impedance spectroscopy has been used for this purpose and to characterize thick film ZnO sensors for outer space applications.

Screen-printing of pure ZnO has not produced a sensor robust enough for outer space applications; the use of a glass binder shows promise to overcome this limitation.

List of Contents

List of Tables

List of Figures

DECLARATION OF AUTHORSHIP

I, **Juan Carlos Valer**

"Development of a Reusable Atomic Oxygen Sensor using Zinc Oxide Thick Films"

and the work presented in the thesis are both my own, and have been generated by me as the result of my own original research. I confirm that:

- this work was done wholly or mainly while in candidature for a research degree at this University;
- where any part of this thesis has previously been submitted for a degree or any other qualification at this University or any other institution, this has been clearly stated;
- where I have consulted the published work of others, this is always clearly attributed;
- where I have quoted from the work of others, the source is always given. With the exception of such quotations, this thesis is entirely my own work;
- I have acknowledged all main sources of help;
- where the thesis is based on work done by myself jointly with others, I have made clear exactly what was done by others and what I have contributed myself;
- none of this work has been published before submission

Signed:

Date: **20 August 2009**

Acknowledgements

I would like to thanks Graham Roberts and Alan Chambers, for providing me with the opportunity to pursue doctoral studies at the University of Southampton. As my main supervisor, Graham Roberts has gone well beyond the call of duty by his constant and relentless support, guidance, and encouragement, for all the red ink (it made me think that somebody had bled over the pieces of paper!) poured over multiple reports and thesis drafts that taught me how to write properly, and for not giving up on me when facing difficulties.

I also want to thank Marc van Eesbeek and Adrian Tighe from the European Space Technology Centre for making available the resources to finance this present research and for making available their laboratories to expose the sensors I developed to atomic oxygen.

I need to thank Simon Klitz from the University of Southampton for his very valuable technical support, in particular while I have been away from campus working in Rolls-Royce.

Last but by no means least I want to thank Father Mike Ryan OMI, for this support and friendship during his time as university chaplain; I have learnt so much from him. I need to extend my gratitude to all the members of the Chaplaincy, for providing me a home away from home, and for the privilege I had to know them and work with them.

Acronyms and Abbreviations

AC	Alternating Current
AO	Atomic Oxygen
ASTM	American Standard Testing Materials
ATOX	Atomic Oxygen Source at ESTEC
DC	Direct Current
e	electronic charge
e^-	electron
ESA	European Space Agency
ESD	Electron-Stimulated Desorption
ESTEC	European Space Research and Technology Centre
eV	electron-volt
GPS	Global Positioning System
h	Planck's constant
H^+	hole
IS	Impedance Spectroscopy
k	Boltzmann constant
LEO	Low Earth Orbit
m_e	Electron Mass
QCM	Quartz Crystal Microbalance
R	Universal Gas Constant
RF	Radio Frequency
SCL	Space Charge Layer
UV	Ultraviolet
ZnO	Zinc Oxide

A	cross-sectional area	m^2
a	specific outgassing rate after one hour	
a(t)	surface density of adsorbed atoms at time t	$atoms.m^{-2}$
a*	Co/a∞	
a_1	lattice constant	Å
a_3	lattice constant	Å
a_∞	maximum surface density of adsorbed atoms	$atoms.m^{-2}$
b	breath of sensor	b
C	capacitance	F
C_{dl}	capacitance of diffusion layer	F
C_{mo}	resistance of interface between cluster and oxide	F
Co	surface density of adsorbed atoms	$atoms.m^{-2}$
D	diffusion coefficient	$m^{2}.s^{-1}$
d	sensor thickness	m

D^0	frequency factor	$m^{2}.s^{-1}$
E	potential difference	V
E_0	potential excitation signal maximum amplitude	V
E_A	Activation Energy	J (or eV)
E_D	Activation Energy of Desorption	J
E_e	Electron Energy	J
E_t	potential excitation signal at time t	V
F_t	fluence or total flux	$atoms.m^{-2}$
F	flux of impinging atoms on a surface	$atoms.m^{-2}.s^{-1}$
f	excitation signal frequency	Hz
g	conductance	S
I	Current	A
i	surface density of ions	$ions.m^{-2}$
I_t	currrent response at time t	A
j	flux	$atoms.cm^{-2}.s^{-1}$
K	macroscopic dielectric constant	
Ke	rate of escape	
L	lenght	m
l	distance between electrodes	m
m	mass	kg
n	Charge carrier number density	$atoms.m^{-2}$
n_b	electronic concentration in bulk	$electrons.m^{-3}$
N	number of molecules or atoms bonded to surface	
N_b	number of charge carriers in bulk	
N_c	effective density of states	m^{-3}
N_d	density of donor atoms	m^{-3}
n_e	extrinsic charge carrier concentration	m^{-3}
n_o	initial gas surface density	$atoms.m^{-2}$
n_s	surface electronic density	$electrons.m^{-2}$
N_s	number of surface charge carriers	
p	pressure	
P	power	W
P_{O2}	partial pressure of molecular oxygen	Pa
P_T	total air pressure	Pa
q	outgassing rate	$Pa.m^3.s^{-1}$
q_i	individual outgassing rate	$Pa.m^3.s^{-1}$
q_T	total outgassing rate	$Pa.m^3.s^{-1}$
R	resistance	Ω
R_0	Initial Resistance	Ω
R_{dl}	resistance of diffusion layer	Ω

R_g	grain resistance	Ω
$R_{g(core)}$	resistance of pure core of ZnO crystallites	Ω
R_{gb}	grain boundary resistance	Ω
R_{mg}	resistance of CoFe clusters	Ω
R_{mo}	capacitance of interface between cluster and oxide	Ω
r	interatomic distance	m (or Å)
S	pumping speed	m^3s^{-1}
T	absolute temperature	K
t	time	s
Th	thickness	m
Th_0	initial thickness	m
U_i	minimum potential energy	J
W	width	m
w	frequency	$rad.s^{-1}$
x	distance	m
Y	erosion yield	cm^3/atom
y	diffusion depth	m
Z	Impedance	Ω
Z'	real impedance	Ω
Z''	imaginary impedance	Ω
Z_0	total impedance amplitude	Ω

α	fraction of adsorbed atoms that become ionized	
β	non-dimensional coefficient	
γ	scattering coefficient	
ε_d	donor level below conduction band	eV
ζ	non-dimensional exponent of decay	
θ	free charge surface number density	$electrons.m^{-2}$
κ	single crystal conductivity	$S.m^{-1}$
κ_b	conductivity of the bulk	$S.m^{-1}$
κ_s	the conductivity of the surface	$S.m^{-1}$
λ	Mean Free Path	m (or Å)
μ	electronic mobility	$s^{-1}.V^{-1}$
v	Frequency	Hz
v_0	vibration frequency of a molecule-surface bond	Hz
ρ	Resistivity	Ω·m
σ	conductivity	$S.m^{-1}$
τ	residency time	s
τ_i	time constant (relaxation time)	s

Φ	excitation frequency phase shift	rad
ω	frequency	$rad.s^{-1}$
ω_{max}	maximum frequency	$rad.s^{-1}$

1. Introduction

The aim of this research is to develop a thick film sensor made of zinc oxide that would accurately respond to various fluxes of atomic oxygen (AO), allowing it to be regenerated after saturation.

Atomic Oxygen has a concentration in Low Earth Orbit (LEO) high enough to erode and degrade some spacecraft materials. Since the composition of the upper atmosphere, where several manned and unmanned spacecraft operate, is highly variable due to several factors, ways to monitor the concentration of AO in real time have been developed over the years. Recently, there have been attempts to design sensors that can be used for long periods of time without replacement.

Recent experience in the design of sensors of this latter type include the use of thin films of ZnO, a well known semiconductor which has the potential to release upon heating the adsorbed AO acquired during testing. Problems with this design, however, include hysteresis and some erratic response.

The sensors that are the focus of this research are thick films of ZnO that have been developed in an attempt to overcome the limitations of thin films, and to provide a very affordable means to fabricate sensors for atomic oxygen flux measurement. These sensors were manufactured using a thick film technique of screen printing over a substrate (alumina) that is inert to the action of AO. In the ideal case, the impinging atomic oxygen would be adsorbed upon the zinc oxide which would increase its resistance; this change would be measured as an indicator of the AO flux. By suitable heating, the adsorbed oxygen atoms would be released from the sensor and its original properties would be restored.

So as to provide an adequate background for the present work, a brief introduction is presented on the near Earth space environment, and the interactions of AO with spacecraft materials. A summary to the present most important AO measurement techniques is also presented.

Since the testing of sensors in LEO is not always possible or affordable, many techniques to simulate AO in ground laboratories have been developed. These techniques vary significantly in the fluxes, contaminants, and energy of the AO produced, among other factors, which can have an effect in the understanding and response of a measurement technique. Consequently, the most important AO sources are briefly described in this document, together with ATOX source of the European Space Agency which was used to evaluate the sensors of this research.

The basics of semiconductor theory are given in this thesis to as to introduce the basic concepts and vocabulary on this field, followed by a brief description of ZnO crystals. Impedance Spectroscopy has been used to characterize the response of the sensors and to measure it; an introduction to this technique is provided.

The technique used to manufacture the thick ZnO sensors is also described here together with an attempt to characterize the sensors before AO exposure.

The rationale and results of testing the sensors exposed to a flux of AO in ATOX are presented here, followed by an attempt to understand their response. A follow-up research plan is outlined in this thesis.

2. Space Environment and Atomic Oxygen

The term “Space Environment” typically applies to the environment that a spacecraft encounters when it orbits our planet above most of the atmosphere. Although low Earth orbit space is considered to be very close to a vacuum, in reality there are chemical elements that can severely impact the ability of a vehicle to fulfill its mission. Interactions with the space environment are credited with about 20 to 25% of all spacecraft failures *(Tribble, 1995).*

Orbiting spacecraft can encounter significant amounts of neutral molecules and/or atoms, micrometeorites, manmade debris, all ranges of electromagnetic radiation, and charged particles.

The range of orbits between 300 km and 1000 km, where most of the crewed spacecraft and a significant number of other vehicles operate, is called “Low Earth Orbit” or LEO for short. The main constituent of the atmosphere in LEO up to an altitude of 650 km is by far atomic oxygen. In LEO, the atmospheric pressure is about ten orders of magnitude less than at sea-level, and although a small relative value, it is significant enough to take into consideration its effect on spacecraft materials. It should be noted that several factors play in keeping the composition and physical variables of LEO changing; among them are solar cycle variations, Earth albedo, latitude, and others. As a consequence of this, the description of the very high Earth atmosphere should always be considered in terms of average values rather than exact numbers.

The neutral atmosphere, the region where neutral molecules and atoms have a higher concentration with respect to ionized particles, is located between 175 km and 1000 km. At these altitudes, the ultraviolet (UV) radiation from the Sun severs intra-molecular bonds with a low probability of charging the newly independent atoms. Another consideration on the composition of the atmosphere is that gravity makes the heavier particles tend to be closer to the surface of the Earth than the lighter ones. At 175 km the concentration of neutral atomic oxygen takes predominance with respect to N_2. At 650 km of altitude, Helium becomes the

most abundant atom, a situation that continues up to 2500 km where Hydrogen takes its place as the element with the highest concentration.

The flux of AO at an altitude of about 300 km is typically 10^{15} atoms/cm^{2}s, although this value changes according to the eleven year-long solar cycle, and other short-term Sun related phenomena.

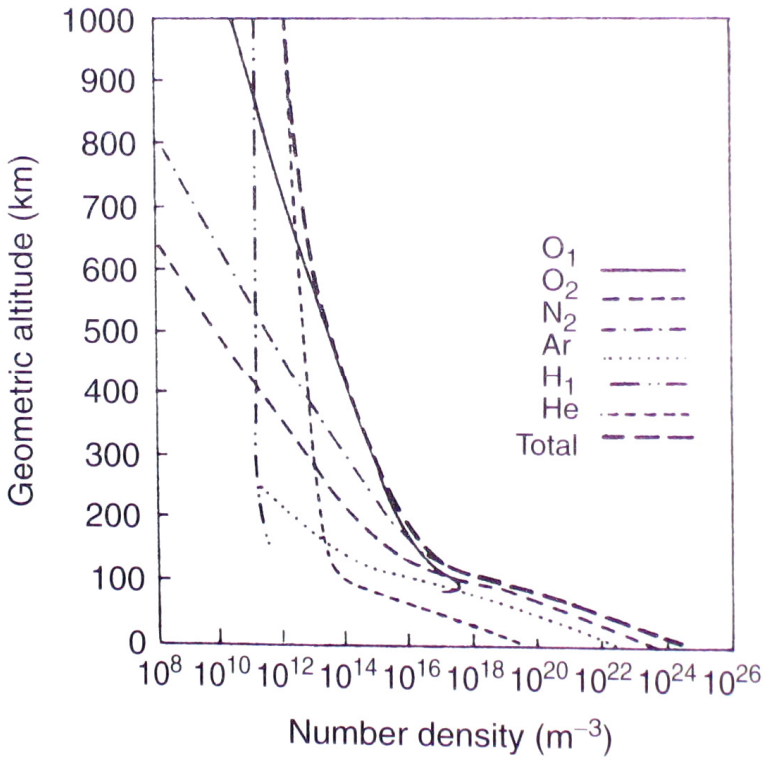

Figure 2.1 Atmospheric Composition as a Function of Altitude *(Fortescue et al., 2003)*

Typically, the Space Shuttle and the International Space Station operate between 300 km and 600 km of altitude, and are thus subject to a continuous attack by atomic oxygen, an element known for being highly reactive. Spacecraft travel at these heights with a tangential speed of about 8 km/s. Since the thermal velocity of the atomic oxygen is about an order of magnitude less than this value, the orbital velocity (8 km/s) can also be considered the relative speed between the ram face of the spacecraft and AO regardless of the direction of motion of the AO; this is equivalent to an energy of 5 eV.

During solar maximum, in which the heated atmosphere expands due to enhanced solar activity, the atmospheric density in LEO can be significantly increased.

Measuring in real time the AO flux in which a particular spacecraft operates becomes then indispensable so as to take the appropriate measures to prevent or diminish the degradation of some of its systems.

3. Effects of Atomic Oxygen on Spacecraft Materials

Atomic Oxygen will interact with spacecraft materials by causing atmospheric drag and the sputtering of surface materials. It will also react chemically with spacecraft causing glow and surface damage *(Tribble, 1995).*

Atmospheric drag occurs due to momentum transfer between the spacecraft and the atomic oxygen neutrals, and results in orbit decay and eventually reentry into the Earth's atmosphere. To prevent this, the fuel budget of the spacecraft has to allow for periodic burns to increase altitude. Drag can increase during a solar maximum in which the heated atmosphere expands and increases its density in LEO.

Sputtering is caused when high energy neutral atoms (or molecules) impact the surface of a spacecraft, severing a chemical and/or surface bond, and in many cases severely damaging or degrading the surface in question. This phenomenon can be enhanced when spacecraft charging is present, in which case it can alter the properties of shields and other equipment.

Optical glow has been reported on numerous spacecraft and on the Space Shuttle. It is attributed to the interaction of the neutral higher atmosphere with the spacecraft's materials, and important research has been done to understand the chemical mechanism of this phenomenon *(Caledonia et al., 1990, 1993; Vierek et al., 1991).* The glow, which peaks at about 680 nm *(Vierek et al., 1991, 1992),* can interfere with remote sensing instruments, and so far the only known way to reduce it is to change the composition of the surfaces exposed to the ram direction. Unfortunately, materials that to do not glow in LEO tend to be susceptible to chemical attack by atomic oxygen.

It is known that fast AO reacts with a variety of materials, causing erosion, oxidation, damage, and degradation of the surface exposed. Due to launch weight restrictions, some of the materials damaged by atomic oxygen are very thin and its effects on the overall spacecraft can be severe and can endanger the mission of the spacecraft or reduce its lifespan; this was the case with the first generation of

GPS satellites due to faster than anticipated degradation of their solar panels *(Tribble, 1995).*

Atomic Oxygen can react with coatings such as silver and osmium by oxidizing them, which can significantly change the properties of the coatings. It can also damage or destroy unprotected silver wire used to interconnect adjacent solar cells. The relative speed of 5 eV of AO is enough to sever many molecular bonds, including that of several polymers *(Packirisamy, et al., 1995).*

AO can also react with the exhaust plumes of main propulsion systems and/or reaction and control systems, creating a cloud of contaminants that will orbit the earth around the source spacecraft. Some of the substances of this cloud can adhere to the surface, causing a change of properties of the material in question or degrading the performance of certain instruments.

Protection of materials that can be damaged by AO in LEO is paramount; any defect of the protective coating or structure may allow the atomic oxygen to attack the material underneath. Atomic-oxygen undercutting is a potential threat to vulnerable spacecraft materials that have atomic-oxygen protective coatings *(Groh et al., 1994).*

Due to the chemical nature of the AO interaction with many spacecraft materials, the potential damage is dependent on the total flux of AO, so the protection of pertinent materials needs to consider the total flux (or fluence) at the end-of-life of the spacecraft.

3.1 Mars and Venus

It should be noted that there is ample evidence of the presence of atomic oxygen in the upper atmospheres of Venus and Mars *(Fox et al., 2000, Hodges, 2000, Kim et al., 1998, Slanger et al., 2001).* With the recent commitment made by the United States to explore and eventually send manned crews to Mars, this planet is going to continue to receive exploration robots to further study the planet.

Observation platforms for both Venus and Mars are likely to be placed in orbits such that they may receive a fluence of AO over time, which could result in

degradation of some of its equipment. Monitoring of the AO presence in their upper atmospheres remains a field in which much development and understanding needs to take place. In this case, the need for reliable AO sensors, suitable for long-duration missions, is clearly important.

4. Overview of Hyperthermal Atomic Oxygen Sources

Clearly, it is not always possible to test spacecraft materials in low Earth orbit, for both practical and economical considerations, as well as the need on occasions to isolate one or more of the environmental effects from the rest. There is also the need to accelerate the testing of some materials, so as to obtain accurate but relatively fast results equivalent to a long orbital exposure.

Many types of AO sources have been developed over the years, all of them with strengths and limitations. A brief description of the most important types of sources will be presented in this chapter; extensive reviews of different types of AO simulation facilities have been published elsewhere *(Kleiman et al., 2003; Kudryavstev et al., 1994).*

It is widely accepted that the atomic oxygen in LEO has the following general characteristics (which actually vary with altitude):

- Kinetic energy of approximately 5 eV
- Flux of approximately 10^{15} atoms/cm^{2}s
- Neutral, ground state (O^3P) atoms
- Very low level of ionized species
- Low level of other species

The AO flux in LEO varies with altitude and time (the latter related to the solar cycle), and this variation can be several orders of magnitude *(Hedin, 1988).* An “ideal” AO source should be able to reproduce all of the above conditions.

Ideally, in addition to the above an AO simulation facility would also be able to replicate the LEO pressure, temperature and (solar) ultra violet (UV) conditions. Also, for accelerated testing of materials in a ground-based facility, a flux higher than that quoted above would be desirable. Unfortunately these requirements are very demanding, and often conflict. Nevertheless Kleiman et. al. *(2003)* identify 14 major AO sources worldwide that are currently being used for testing materials and

carrying out fundamental research into AO-related phenomena; more may exist or are under development.

Most of the various different types of facility that have been developed use molecular oxygen (sometimes in combination with other inert gases) as the feed gas. Hence the first requirement is to supply sufficient energy to dissociate the oxygen; further energy is required to accelerate the atoms to the required speed (≈ 7.8 km/s for LEO simulation). Thus in principle it is possible to distinguish between the different types of sources by noting the methods used for dissociating and accelerating the test gas.

As a very general guide, there is an approximately inverse relationship between AO flux and energy *(Banks et al., 1988):* in early tests, experiments were carried out in ion sources – capable of providing very high energies but low fluxes – or in plasma asher sources, i.e., low energy but high flux *(Kleiman et al., 2003).* Because neither type of source duplicates the LEO conditions well, results were of questionable value. More recently, however, sources have evolved to match better the requirements. In this chapter we will concentrate our discussion on four of the most commonplace – or promising – types of source for LEO simulation.

4.1 Ion Sources

This type of source has been developed extensively during the last decade or so *(Kleiman et al., 2003)*. A beam of positive or negative ions is created by either radio-frequency (RF) excitation or electron bombardment and then accelerated electrostatically. The ions are then neutralized by either charge exchange or surface neutralization. However, gaseous charge exchange is inefficient and surface neutralization presents the complication that the reflected beam does not have a uniform kinetic energy. The 5 eV requirement tends to lie at the lower end of the achievable range and AO fluxes are modest, although in theory LEO-like fluxes can be achieved.

4.2 Microwave or RF Discharge

In this type of device a plasma is created – in this case by microwave or RF discharge – and expanded steadily in a supersonic nozzle. To achieve high velocities helium is used as the carrier gas, with molecular and atomic oxygen minor constituents (AO typically being 2-3% of the beam flux). Materials and pumping limitations restrict the resultant AO beam energy and fluxes to about 3 eV and 10^{16} to 10^{17} atoms/cm^{2}s, respectively *(Kleiman et al., 2003).*

4.3 Laser Discharge

Two types of laser-based sources have been developed. In one, a continuous optical discharge from an infra-red (CW) laser creates a plasma which is then expanded to high velocity in a supersonic nozzle *(Cross et al., 1988).* Conditions can be managed so that ionic recombination takes place in the nozzle, leaving the resultant beam essentially neutral. To obtain the required velocity the molecular oxygen is included as a minor constituent in an inert carrier gas; again pumping limitations usually restrict the beam to low/moderate AO fluxes and energies.

An alternative approach is to use a high-energy pulsed laser to create the plasma *(Caledonia et al., 1987).* In this type of facility molecular oxygen is introduced into the discharge chamber that has a conical nozzle. The laser pulse is fired and the plasma is then expanded through the nozzle by the resultant detonation/blast wave, generating a high velocity beam comprising a mixture of mainly neutral AO with some molecular oxygen. The advantage in comparison with the continuous discharge is that no carrier gas is required and the pumping requirements are lessened. Consequently time-averaged fluxes that can be achieved in this kind of source can be greater than in LEO, allowing the possibility of accelerated testing of materials, with energies in the range of 1-16 eV.

The AO source used in this research uses a high-energy pulsed laser. It is located at the ESA's European Space Research and Technology Centre (ESTEC) in the Netherlands.

4.4 Electron-Stimulated Desorption (ESD)

A radically different approach is adopted in this type of facility: one side of a specially designed ceramic is placed under a high pressure of molecular oxygen, while the other side is exposed to vacuum; the latter side is usually coated with a thin film of silver. The molecular oxygen on the high-pressure side dissociates into negative AO ions and migrates through the ceramic towards the low pressure side; these ions become neutral as they are adsorbed on the internal side of the silver film. Upon reaching the outer surface of the silver film, and before they recombine into molecular oxygen, a beam of electrons impinging on the surface causes the oxygen atoms to desorb and leave with a kinetic energy similar to LEO conditions *(Hoflund et al., 1994).*

This method has provided fluxes similar to LEO for a short amount of time, without a significant production of ions or other contaminants *(Valer, 2000).* Further development efforts are needed to increase the flux of oxygen through the membrane in order to allow the production of higher AO beam densities.

Table 4.1 provides a comparison of some AO sources based on a few of the desired characteristics.

Table 4.1 AO source types and basic characteristics

Technique	Kinetic Energy (eV)	Contaminants	Normalized to LEO Flux
Ion Source	5-80	O ions, VUV	0.1-10
Laser Discharge	1-16	O ions, VUV	0.1-100
Microwave/RF Discharge	1-5	O ions, VUV	1-100
Electron-Stimulated Desorption	4-6		0.01-1

5. Overview of Atomic Oxygen Flux Measurement Techniques

A review of a variety of AO flux measuring techniques for space-based applications is given in Osborne et al. *(2001).* The following section is a brief description taken from Osborne et al. *(2001)* and White et al. *(2004)* on the most relevant AO sensing techniques for ground and space applications. Two highly detailed references to be considered for any serious comparison among techniques by an experimenter are Minton *(1995),* and ASTM standard E2089-00.

5.1 Kapton witness samples

Kapton-H is a polymeric material commonly used in spacecraft thermal insulation. Impinging AO erodes the material by producing volatile reaction products. The resultant mass loss can be used to provide a measure the AO total flux; so far Kapton mass loss is regarded as the standard measure of AO fluence. The erosion yield for Kapton has been well established as $3x10^{-24}cm^3$/atom *(Reddy, 1995; Leger at al., 1986).*

However, it is important to mention that the erosion yield of Kapton-H is believed to be dependant on the energy of the impinging AO, which is a problem when using it to compare results from facilities that produce beams with different energies as described in Osborne et al. *(2001).*

There are some practical difficulties with the use of Kapton-H witness samples. It is not possible to have real time measurements, since the sample has to be taken out from the test chamber to be weighed. Hence the method is not sensitive to local changes of flux. There is also the risk of Kapton being contaminated and even reacting with the atmosphere and thus changing its mass; Kapton is particularly sensitive to humidity. Wolan et al. *(1999)* have described the limitations of Kapton for accurately measuring AO fluxes.

Nevertheless, the use of Kapton-H witness samples provides a simple method for determining AO fluence with order of magnitude accuracy.

It is also important to consider that Kapton-H is in the process of being discontinued, and it has been replaced by Kapton-HN; Miller et al., *(2008),* have made a comprehensive study of the factors relevant to the erosion yield of this material in LEO.

5.2 Quartz Crystal Microbalances

Quartz Crystal Microbalances (QCM) have successfully been used to measure AO fluxes both in ground-based simulation facilities and in LEO. The use of crystals covered with either silver or carbon is considered to be a mature technology. A good review on QCMs can be found in Osborne et al., *(2001).*

QCMs provide an *in situ* measurement of the flux of atomic oxygen that is very specific to atomic oxygen. If the crystal is coated with silver, the AO will chemisorb and therefore its mass will increase; if coated with carbon, the AO flux will erode it with a corresponding decrease in mass.

An especially cut quartz crystal is excited by the control unit and its frequency is measured; a change of frequency can be accurately related to a change of mass of the crystal. With the use of a suitable calibration curve, the rate of change of frequency can be related to an AO flux. It should be noted, however, that the rate of erosion of C-QCMs is dependant on the energy of the impinging AO, which can be a complication if this value is not known or changes significantly.

QCMs can be very small, have high accuracy and repeatability, can have low mass, allow remote operation, and are relatively inexpensive. They have the limitation though that the material that is used to coat the crystal has a limited useful lifetime, after which the instrument is no longer capable of detecting AO.

Further research on silver-coated QCMs needs to be performed to improve their accuracy, since the sticking coefficient between the AO and the silver is not accurately known, and there are some uncertainties related to the chemistry between those two species and the diffusion rate of AO on silver *(Valer, 2000).*

QCMs can also be used to monitor the deposition of contaminants in a vacuum chamber. For this application, it is enough to use an uncoated crystal.

Provided that this crystal is kept at about the same temperature as the chamber, contaminants should deposit on the crystal at the same rate as on the rest of the chamber. The corresponding change in mass would in turn change the oscillation frequency of the crystal, which can be used to accurately determine the deposition rate of contaminants.

5.3 Catalytic Probe

This method is simple, reproducible, and very sensitive. The probe consists of a wire, coil, or foil and it may be movable in the test area. Its highly catalytic surface is heated by the recombination of reactive species.

A method very appropriate to absolute measurements of atom concentrations was applied to the O-atom reactions by Elias et al. *(1959).* The probe is a silver-coated platinum wire coil, large enough so that the temperature rise due to recombination is not large ($\Delta T<100℃$). It is operated isothermally at an elevated temperature and the difference in electrical power to produce the same wire temperature in the presence and absence of O-atoms is measured.

The obvious disadvantage of this method is the lack of specificity to detect AO. It has been reported that oxygen molecules in the metastable state (92.2 kJ/mole above the ground state) will produce an erroneously large heat release in the detector. This error is avoided with the complete absence of O_2 in the system. In this scenario, measurements using this method are in excellent agreement with values obtained by NO_2 titration.

5.4 Electron Spin Resonance

This method is highly specific for the detection of atomic oxygen recombination. The resonance lines are easily identified and other information such as temperature can be obtained for any parametric excited state.

Among its principal disadvantages are cost and complexity. Also, the fact that it gives only space averages of concentration over a considerable length of the flow tube. Absolute or even relative concentrations are calculated with some

difficulty from experimental data. The signal depends on the average collision frequency of the atom and this complicates an experiment with added gases.

The only rate data so far reported by this method are neither qualitatively nor quantitatively reliable.

5.5 NO_2 Titration

This technique is based on the following reactions:

$$NO_2 + O \rightarrow NO + O_2 \tag{5.1}$$

$$NO + O \rightarrow NO_2 + h\nu \tag{5.2}$$

where h is the Planck constant and v is the frequency of the impinging radiation. The titration involves the careful measurement of the flux of NO_2 in a fast flow tube. As the first reaction is about five orders of magnitude faster than the second, no energy emission would take place from the second reaction when the number density of O is less or equal than the number density of NO_2.

When the flux of O is higher than that of NO_2, the second reaction begins to take place and light emission would be present. This emission is a greenish-yellow afterglow that has been well determined by spectral analysis. When the number density of O doubles that of NO_2, the maximum light emission occurs; the concentration of NO remains constant during the peak emission.

This glow can be detected by means of a photomultiplier, so that the end-point of the titration can de determined with precision. This method is highly sensitive and specific. It has been successfully applied to pressures below 133 Pa, and the presence of neutral gases such as Argon does not interfere with the measurements. Unfortunately, the implementation of this method is not easy, since the equipment required is not only bulky, but it is not commercially available and has high demands in terms of vacuum requirements.

A good review on NO_2 titration can be found in Thrush *(1967).*

5.6 Mass Spectrometers

The main principle behind this kind of instrumentation is the ionization of all the species in the beam so as to later divert and detect them. This technique detects mass-to-charge ratios, and as such, would give the same reading for both O^+ and O_2^{+2}.

Mass spectrometers have a virtually indefinite useful detection life and can also be used to detect other species present in the flux. The most common type is the quadruple mass spectrometer, which has been successfully used on numerous occasions for both flight and ground AO measurements. A disadvantage of this technique is that the equipment required may be expensive, consume a large amounts of power, and it is generally bulky. Another difficulty is the possibility of AO recombination before detection.

5.7 Actinometers

These methods have the significant advantages of allowing in-situ measurement, high specificity and sensitivity, low complexity, low cost, remote operation, and high potential for miniaturization.

Suitable in-situ actinometers make use of silver, carbon, and zinc oxide (ZnO). All give a resistance increase when AO is absorbed and/or reacts with the sensor material. Resistance is easily measured in-situ and hence, unlike Kapton, real-time determination is possible.

Silver actinometers use the change in resistance of thin silver films as they are exposed to atomic oxygen. The progressive conversion of the silver into non-conducting silver oxides causes the film resistance to increase, the extent of which depends on the total fluence (integrated flux) of atomic oxygen to which the film is exposed. This method assumes uniform oxidation.

The relation between the resistance, R, of the silver sensing film and its dimensions is simply given by Equation 5.3:

$$R = \frac{\rho(1+\frac{3\lambda}{8\mathrm{T}})L}{WTh} \tag{5.3}$$

where ρ is the resistivity of the conductor, L is the length, W is the width, and Th is the thickness of the sensing element, λ is the mean free path of the conducting electrons, a value that is around 530 Å for silver films between 200 and 4000 Å of thickness.

The silver oxidation process apparently involves three stages. The first stage is linear up to a depth of 340 ± 100 Å. This is typical of a process controlled by surface reaction. The second stage appears to be parabolic, a typical response of a process controlled by diffusion. This suggests that the oxide layer does not inhibit the transport of oxygen atoms until a depth of approximately 340 Å of oxide has formed.

The final stage involves a rapid increase in the rate of change of the resistance with film break up, a process that continues up to a depth dependant on the thickness of the film. This later stage is believed to be an end-effect caused by the breakdown of the very thin conduction films into discrete islands, and the data collected in this range is not reliable.

In Fig. 5.1, the change of resistance of thin silver films of various thicknesses can be seen as a consequence of exposure to an AO source capable of producing a flux of approximately 10^{15} atoms/cm^{2}s. The three steps in the oxidation process on the silver described in the previous paragraph can be seen.

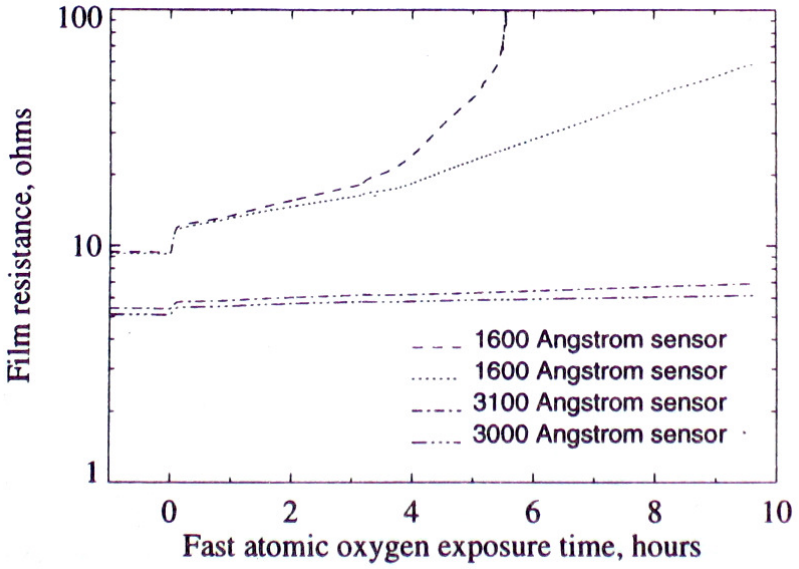

Figure 5.1 Resistance change on thin silver films as a consequence of AO attack *(Harris et al., 1997)*

Unlike silver, carbon releases volatile oxidation products and hence carbon actinometers are not diffusion limited. For carbon actinometers, the resistance (R) can be calculated by using Equation 5.4 *(White et al., 2003):*

$$R = \frac{Th_0 R_0}{Th_0 - F_t\, Y} \tag{5.4}$$

where Th_o is initial thickness in m, R_o is initial resistance, F_t is fluence in atoms/m^2, and Y is erosion yield in m^3/atom. Follows, as an example, the response of a carbon actinometer to the flux of AO, when exposed to a flux of AO (total fluence in the order of 10^{19} atoms/cm^2s); Fig. 5.2 shows that, as the exposure progresses, the resistance of the carbon film increases due to the loss of this material from the sensor.

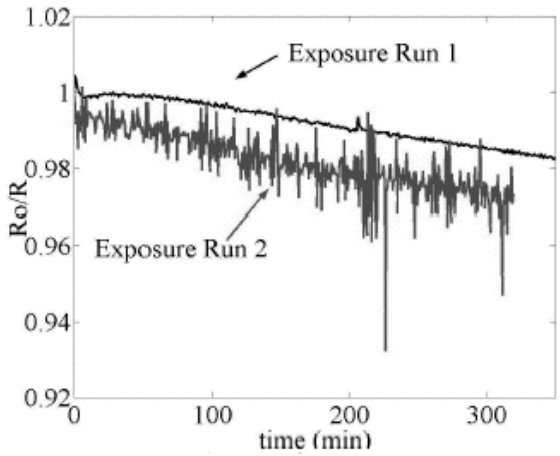

Figure 5.2 Normalized resistance change in a carbon actinometer exposed to an atomic oxygen flux *(White et al., 2003)*

In common with silver, carbon actinometers are consumed by the oxidation process and hence have a limited life. The useful life is further limited by the fact that the diffusion of the AO into the silver is not well understood, and only the first stage of oxidation, when a linear response is achieved, can be used with confidence.

Osborne et al. *(1999)* has demonstrated that thin, sputtered films of ZnO are also sensitive to AO flux. They have the advantage over silver and carbon actinometers that they can be regenerated by heating to moderate temperatures which, in principle, allows their useful lifetimes to be extended indefinitely. Unfortunately, recent experience with these sensors shows a significant hysterisis during regeneration and an un-characterized variability of response to AO with film deposition conditions. A more detailed treatment of the experience so far with ZnO sensors is presented in Chapter 10.

It should be emphasized that actinometers like the ones discussed here have the great advantage of being suitable for miniaturization.

A good review on actinometers can be found in Osborne et al., *(2001).*

6. Basic Semiconductor Physics

As ZnO is a crystalline semiconductor material this chapter provides a brief introduction to Crystallography, Semiconductor Physics, and Surface Physics, in order to make available the basic tools for understanding the development of the present work. An excellent source for more detailed information on these matters and applications is McKelvey *(1966).*

6.1 Crystallography

6.1.1 Basic Atomic Structure

Atoms are classically represented by a positively charged nucleus and a cloud of electrons that orbit the nucleus in a fashion that reminds us of the Solar System. The orbits of the electrons are not random, and only certain distances from the nucleus and trajectories are allowed; this is determined by quantum mechanics. Each orbit represents a particular energy level, and to promote an electron to a higher orbit, it must be provided with a particular amount of energy. In the same way that the planets of the Solar System orbit within a gravitational potential field with the Sun at the center, the electrons' orbit are in a electrical potential field with the nucleus at the center.

These results can be obtained by solving the following one-dimensional time-independent Schrödinger equation *(Smith, 1964)*, Equation 6.1, a task that is beyond the scope of the present work):

$$\frac{d^2\Psi(x)}{dx^2} + \frac{8\pi^2 m_e}{h^2}(E_e - V)\Psi(x) = 0 \qquad (6.1)$$

A solution is:

$$E_e = \frac{n^2 h^2}{8mL^2} \qquad \text{n=1, 2, 3,…,}\infty \qquad (6.2)$$

where: x is distance, m_e is electron mass, h is the Planck's constant, E is electron energy, and V is the potential experienced by an electron. The above equation clearly shows how the energy levels and the distances between electrons and the nucleus in atoms are 'quantized' or determined as discrete values, that is, there are some 'forbidden orbits', energy levels that electrons cannot attain.

6.1.2 Basic Definitions in Crystallography

We normally use the term *solid* to describe substances that, although normally rigid, can display an elastic behaviour when exposed to external or other stresses. Among solid substances, we find two broad categories: amorphous and crystalline. In an amorphous solid there is no regularity or periodicity in the atoms or molecules that make up the bulk of it; we can regard them as supercooled liquids. On the other hand, in crystalline solids, we find regularity in the type of atoms and/or molecules and in their relative position to one another.

Naturally, it is easier to study crystalline solids, and easier to describe them due to their regularity and periodicity in terms of structure. We will deal with this type of solid in this chapter, since ZnO is a crystalline material.

Not all crystalline solids are composed of a single crystal (a group of atoms and/or molecules with the same relative orientation of their constituents), but most are a conglomerate of multiple crystals. Each single crystal in this situation is called a 'grain' and the boundaries between them are called 'grain boundaries'.

6.1.3 Basic Types of Crystals

It can be shown that there are fourteen different ways of arranging atoms or molecules in three dimensions so that all atoms or molecules have the same surroundings. The fourteen basic kinds of crystals are called the "Bravais Lattices."

It should be mentioned that sometimes a relatively small amount of a 'contaminant' (atoms or molecules that do not form part of a crystal) can significantly alter the physical properties of such solid; sometimes this doping of material is intentional to modify the material for a particular use.

There are many ways to characterize crystals, such as according to their mechanical or chemical properties. But for the purpose at hand, it is more convenient to classify solids according to the type of interaction that holds the atoms together within the structure of the crystal. And for this, we need to consider the two basic electrostatic forces that need to be in balance to keep a crystal together: attraction of atoms of different electrostatic charge (ions), and the repulsion between their respective positive nucleus; when the atoms reach such a distance in which both forces are in equilibrium, we have a stable crystal.

According to this criterion, there are four basic types of crystals: ionic, covalent, metallic, and molecular. The main driving force in this classification is the electronegativity of each atom, that is, its ability to attract electrons.

- In *ionic crystals,* where the constituent atoms have very different electronegativities, there is a net transfer of valence electrons (and therefore of electrostatic force) from some atoms to others so as to obtain noble gas configuration, resulting in a strong electric attraction between atoms. A typical example of this kind of crystal is common salt, NaCl.

- In a *covalent crystal,* formed among atoms of similar electronegativity, outer shell electrons are shared so as to obtain the configuration of noble gases, but there is no net transfer of electrostatic charge; the attraction between atoms is not so high as compared to the ionic crystals. A typical example of this is diamond, in which each carbon atom equally shares each of its four valence electrons with four carbon neighbours. It should be mentioned that in many cases, the transfer of electrons between atoms is only partial resulting in crystals that have properties intermediate between ionic and covalent. ZnO is predominantly ionic, but it has some covalent character.

- In *metallic crystals*, the metallic element in free-state is surrounded by free electrons, the crystal being held together by the relatively weak electrostatic force between the negative free electrons and the positive nucleus. These free electrons are responsible for the high electrical conductivity and high temperature conductance characteristic of metals.

- In *molecular crystals* the binding energy between atoms is neither ionic nor covalent, but originates in the instantaneous dipolar moment variations in each particular atom, which in turn come from the instantaneous position of the electrons. These forces are rather weak and are called “van der Waal Forces.” Examples of such material are water ice and dry ice.

6.1.4 Binding Energy of Ionic Crystal Lattices

In ionic crystals (and in some other kinds of crystals as well), the distance between atoms in a crystalline structure is the distance at which the electrostatic attraction forces between atoms of different charge is balanced by the repulsive forces of nucleuses of the same charge. For ionic crystals, the electrostatic attraction between atoms of different charge is the main interaction that keeps the structure together.

One can consider that if two particular atoms are pushed closer together than their equilibrium distance, the repulsive potential energy between the equally charged nucleuses will increase. In the same way, if both atoms are pulled apart a distance r greater than the equilibrium distance d, the potential attractive energy between the ions of different charges will increase. Therefore, the equilibrium distance is such as the summation of both potential energies U_i is the minimum, as can be seen in Figure 6.1.

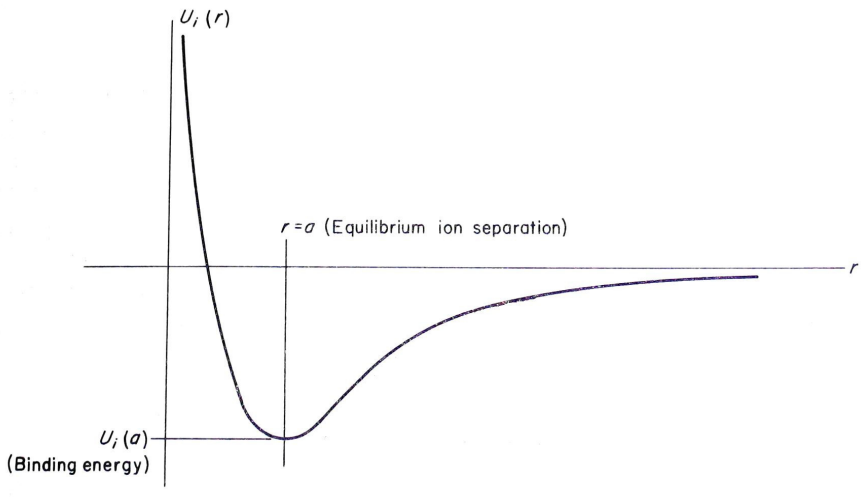

Figure 6.1 Interatomic distance as a function of potential energy *(McKelvey, 1966)*

The lattice energy, or binding energy in a crystal, is the energy required to displace the ions from their position of equilibrium to an infinite distance apart, and it is the 'minimum potential energy' discussed in the previous paragraph.

6.2 Conduction

Quantum theory tells us that for two atoms that are combined within a solid, the wave-vector is found to be as shown in Equation 6.3 *(Somorjai, 1972)*:

$$k = \frac{m_e \pi}{2a}\left\{1 \pm \frac{1}{2\alpha L}\left[1 + 2\exp(-2\alpha c)\right]\right\} \qquad (6.3)$$

The most important result from the above equation is that it shows two different energy levels for each electron. We can expand this result to encompass multiple atoms within a solid, with the resulting multiplicity of energy levels among the combined atoms.

When atoms combine to form oxide crystals, some energy levels of the individual atoms combine into a series of levels that allow the outermost electrons to be shared; the outermost layer is called the 'conduction band'. Each of these levels is in turn subdivided into other energy levels. The same exclusion of individual atoms applies, and electrons are allowed only in certain energy levels, which depend on the nature of the compound. See Fig. 6.2.

At temperatures higher than absolute zero and in the presence of a potential difference, the electrons in the conduction band are free to move in the direction of the electric field applied, and conduction takes place.

Insulators are materials in which the highest energy level (the conduction band) is empty of electrons, while the levels beneath are full, but the energy gap between the empty and the other levels is big enough (of the order of several electron volts) so as to prevent the transfer of electrons. Conduction then is not possible or minimal, even when thermal energy is applied (which should ease the promotion of electrons to higher levels). A conductor presents the reverse situation with their highest energy level rich (but not saturated) in electrons: this makes conduction always possible at temperatures higher than absolute zero.

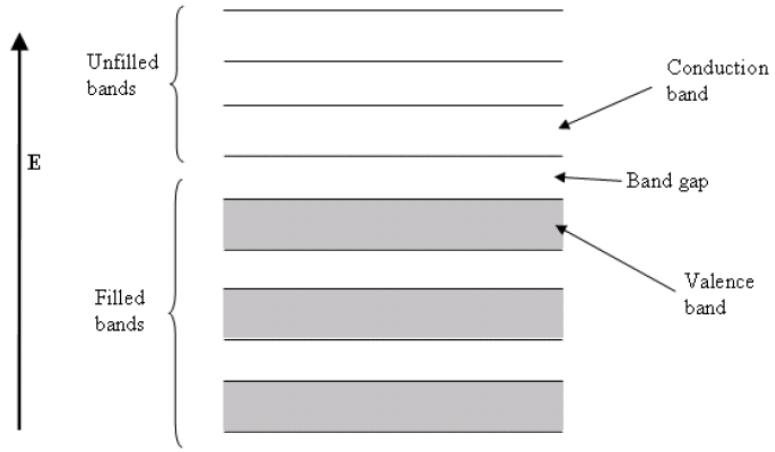

Figure 6.2 Conduction and Valence Bands in a Semiconductor. *(Taken from the online Wikipedia Encyclopedia).*

A semiconductor has intermediate characteristics as compared to a conductor and an insulator: the energy gap is evident, but enough thermal energy can provide sufficient electrons in the upper band to allow conduction. The more thermal energy applied, the more electrons are able to move into the conduction band and the conduction increases accordingly; conduction is therefore strongly dependant on temperature, and the former will experience a strong initial increase when sufficient heat is applied. In addition to this, when an electron in a semiconductor moves into the conduction band, it leaves a positively charged 'hole' in its former lower level (valence) band, which will also allow for conduction in this band by means of a process called 'hole conduction': these 'holes' allow for electrons in the valence band to move to fill them up, creating further holes which will be filled by subsequent electronic displacements in the same band, and therefore increasing conduction in the solid.

The distinction between semiconductors and insulators is one of degree only: all insulators can experience some level of conductance if enough heat is applied, while semiconductors become insulators near or at the absolute zero.

Band gaps depend on temperature because of thermal expansion. Band gaps also depend on pressure.

Statistical mechanical calculations (which are beyond the scope of the present work) indicate that when pressure is applied to a semiconductor, the interatomic distance will decrease while the energy spacing between the valence and the conduction bands becomes larger (and therefore, the energy needed for an electronic transition from the former to the latter increases). This situation will result in a reduction of conductance in a solid when pressure is increased. An example of the increase in energy gap due to pressure (carrying a reduction in interatomic distance) can be seen in Fig. 6.3 for the case of diamond:

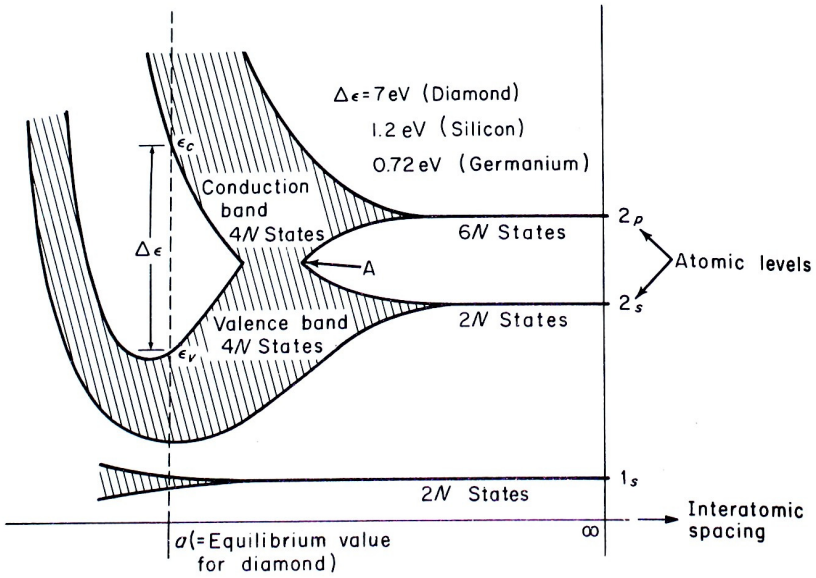

Figure 6.3 Bands arising from the combination of two adjacent carbon atoms in a diamond crystal *(McKelvey, 1966)*

Intrinsic semiconductors are those in which the energetic distance between the conduction band and the lower valence band is not significant (typically about 1 eV or less) and normally there is enough thermal energy at normal room temperature to allow conduction.

In an extrinsic semiconductor, impurities in the lattice structure are responsible for providing charge carriers for conduction. In an ‘n-type’, the impurities provide electrons from donor levels just below the conduction band; these electrons normally have no difficulties in reaching the conduction band and provide conductance. Assuming that the atomic medium in the lattice is similar to a

polarizable uniform continuous medium of macroscopic dielectric constant K, the ionization energy for an electron to leave its atom is smaller by a factor of K^{-2} as compared as that to the atom in isolation.

Zinc Oxide is classified as an ‘n-type’ semiconductor; the impurities come from interstitial Zn atoms.

A ‘p-type’ semiconductor presents the reverse situation of an ‘n-type’: energy (acceptor) levels are created just above the valence band; when electrons are promoted to this new level, positively charged ‘holes’ are left in the valence bands, which are the major contributors for conduction (these holes need to be filled by nearby electrons, which will in turn create further holes and so on, thus allowing conduction).

As it was mentioned before, an increase in temperature will increase the conductance of semiconductors, since more electrons will be promoted to the conduction band. In the case of extrinsic semiconductors, the increase in conductance (which results from an increase in charge carrier numbers [n]), occurs in three steps as seen in Figure 6.4. The following discussion pertains to n-type semiconductors: at absolute zero, none of the electrons reach the conductance band and therefore, there is no conduction; at slightly to moderate higher temperatures, some of the donor atoms are ionized and the charge carrier concentration increases (extrinsic slope); this situation will continue until all atoms capable of being ionized and donating electrons to the conduction band have done so, and therefore the charge carrier number and the conductance remain constant (saturation range); at even higher temperatures, electrons capable of migrating from the valence to the conduction band, giving the crystal some characteristics of an intrinsic semiconductor.

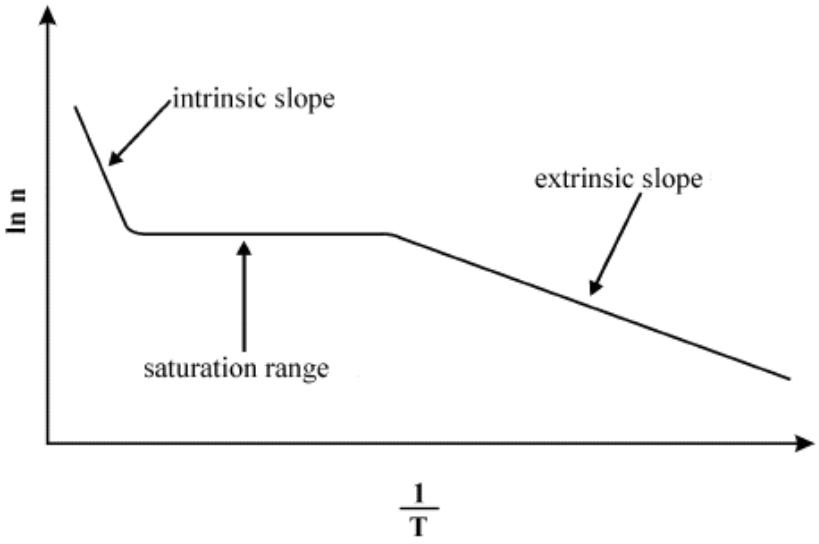

Figure 6.4 Effect of Temperature in the Carrier Number in Extrinsic Semiconductors *(after Smith, 1964)*

From Smith *(1964)* we find that for an n-type semiconductor, with a very low conduction by the holes mechanism, the number of charge carriers is:

$$n_e = \sqrt{\frac{N_d N_c}{2}} \exp\left(-\frac{\varepsilon_d}{2kT}\right) \tag{6.4}$$

where:

n_e = extrinsic charge carrier concentration (m^{-3})
N_d = density of donor atoms (m^{-3})
N_c = effective density of states (m^{-3})
ε_d = donor level below conduction band (eV)
k = Boltzmann's constant ($J.K^{-1}$)
T = absolute temperature (K)

Under these conditions, it can be found that the conductivity (σ) of the sample is:

$$\sigma = n_e e \mu \tag{6.5}$$

being μ the electronic mobility. Using the fact that sample's conductivity and conductance (g) are related by Equation 6.6:

$$g = \frac{\sigma A}{l} \tag{6.6}$$

where A is the cross-sectional area of the sample [m^2], l is the distance between measurement electrodes [m], and the conductance is measured in Ω^{-1}, we can find that the following dependence between conductance and temperature:

$$g = \sqrt{\frac{N_d N_c}{2}} \left(\frac{e\mu A}{l} \right) \exp\left(-\frac{\varepsilon_d}{2kT} \right) \tag{6.7}$$

where μ is the charge mobility in $m.s^{-1}.[V.m]^{-1}$.

After suitable rearrangement, it can be found that the Resistance R can be found by plotting it against temperature:

$$\ln R = \frac{\varepsilon_d}{2kT} - \ln\left(\frac{e\mu A}{l} \sqrt{\frac{N_d N_c}{2}} \right) \tag{6.8}$$

6.3 Photoconductivity

Excess charge carriers, that is, electrons and holes, can be created in many semiconductors by illuminating the material with light of enough intensity such that the photon's energy equals or exceeds the energy gap of that particular crystal. In such circumstances, it is said that the semiconductor is 'photosensitive'; the increase in conductivity can be regulated by using light of the required intensity.

Photoconductivity needs therefore to be taken into consideration when using sensors that react to particular wavelengths, since not only the Sun is an electromagnetic radiation source in LEO, but also some AO sources.

6.4 Semiconductor Surfaces

The discussion so far on semiconductors has assumed an infinite crystal. We need to refine this model to include the consequences for the break in symmetry that a finite solid introduces.

One of these consequences is the existence of surfaces in the solids, which create energy levels called ‘surface states’. These levels will be located in the so-called ‘forbidden gap’ under the conduction band. Electrons from the latter will be captured in the former, with the corresponding decrease in conductance in the solid. A depletion layer of electrons at the surface and immediately under it is created; this is clearly a surface phenomenon that will not extend beyond a depth of about 10μm. Some semiconductors which are not very thick can have a significant portion of their volume affected by this surface phenomenon, which can then be one of the most important drivers in the resistance of the semiconductor.

When conduction electrons are captured by surface states, a ‘layer’ of negative charge forms on the surface of the semiconductor. As a result, a positively charged space charge layer (SCL) develops in the near surface regions of the material due to the presence of immobile, ionized atomic donors (it was from these atoms that the electrons in the conduction band originally came from). These two oppositely charged layers form a dipole in which the positive charge of the ionized donors is compensated by the negative surface charge. The zone from which the electrons were removed is commonly known as the ‘depletion layer’. The negative layer at the surface composed of electrons, and a positively charge region of ionized atomic donors (who gave the electrons at the surface) create an electric potential between those two regions.

This situation of ‘surface states’ changes the electronic band structure of the solid. At the surface of the material, the conduction and valence bands are increased to higher energies by an amount proportional to the surface potential; this is call ‘band bending’. The negative charging of the surface increases the energy requirements (as compared to the bulk) for electrons to migrate to the conduction band near the surface; the surface charge also increases the energy requirements for an electron to migrate from the bulk to the surface. This last two combined effects are called ‘surface barrier’ (sometimes known as ‘Schottky’ barrier).

6.5 Single Crystals

In the case of some single crystals, like that of ZnO *(Jacob, 1975)*, the conductivity is relatively simple to study and measure. In such cases, the

conductivity of the whole single crystal κ can be approximated to be the summation of the conductivity of the surface κ_s plus the conductivity of the bulk κ_b:

$$\kappa = \kappa_s + \kappa_b \tag{6.9}$$

The conductivity of the bulk is practically independent from surface effects, and mainly varies as a function of temperature. If single crystals are small enough that at significant portion of their volume is under the influence of surface effects, the conductivity of the surface will have preponderance over that of the bulk; the former is given by Equation 6.10:

$$\kappa_s = e\mu\theta \tag{6.10}$$

where e is the elementary electric charge, μ is the electron mobility in the crystal, and θ is the free charge surface number density [electrons.m^{-2}]. This result makes it obvious that a ZnO single crystal will have more 'electric' affinity to an atom rather than to a molecule of oxygen given its nature of the former as a donor of electrons (see Chapter 10 for further details on this); the surface conductivity will vary as a function of θ.

At the beginning of an exposure (the flux surface density [atoms.m^{-2}.s^{-1}] being n), a fraction dn of the impinging species will chemisorb to the surface with the corresponding decrease in surface density of free carriers, equal to the increase in the fraction of chemisorbed atoms:

$$\delta n = -\frac{d\theta}{dt} \tag{6.11}$$

The rate of change at the beginning of the exposure of the surface conductivity is given by Equation 6.12:

$$\left(\frac{d\kappa_s}{dt}\right)_{t=0} = e\mu\left(\frac{d\theta}{dt}\right)_{t=0} = -e\mu\delta n \tag{6.12}$$

Since we have assumed that the bulk conductivity is not affected by the change in surface conductivity, the following relation can be concluded, which

relates the initial flux surface density of species to the change of conductivity of the crystal:

$$\left(\frac{d\kappa}{dt}\right)_{t=0} = \left(\frac{d\kappa_s}{dt}\right)_{t=0} = -e\mu\delta n = -(cons\tan t)n \tag{6.13}$$

6.6 Piezoelectricity

Deformation (as a consequence of an applied force) on certain electrically neutral crystals—those not having a centre of structural symmetry—polarizes them by slightly separating the centre of positive charge from that of the negative charge; equal and unlike charges on opposite faces of the crystal result. This charge separation will create a potential difference, or voltage, between the opposite crystal faces. This phenomenon, also called the piezoelectric effect, has a converse: the production of a mechanical deformation in a crystal across which an electric field or a potential difference is applied. A reversal of the field reverses the direction of the mechanical deformation. See Fig. 6.5.

The piezoelectric effect is exploited in a variety of practical scientific and commercial applications.

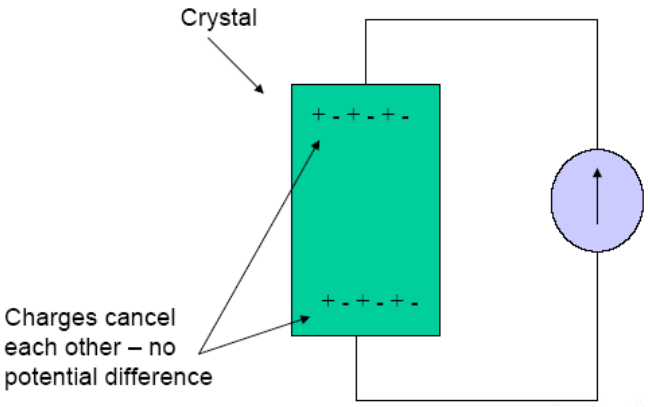

Figure 6.5 Piezoelectric Effect: Crystal before deformation

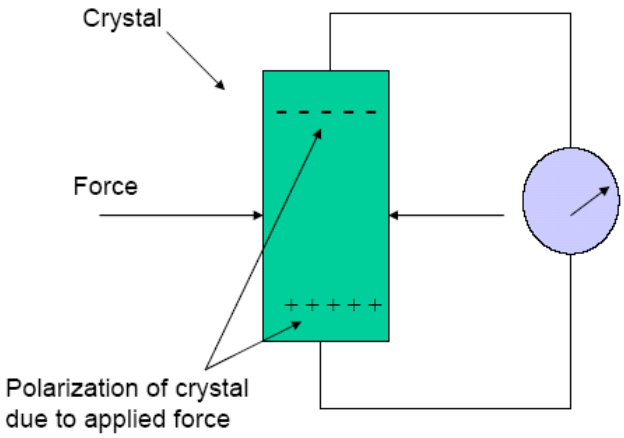

Figure 6.6 Piezoelectric Effect: Crystal after deformation

7. Basic Outgassing Theory

The purpose of this chapter is to provide a basic introduction to outgassing theory, paying attention in particular to outgassing of water molecules and atmospheric gases in vacuum systems.

Any material manufactured in the atmosphere or exposed to it, is going to have gas molecules adsorbed on its surface, or absorbed or dissolved in its bulk. When this material is exposed to a pressure lower than atmosphere, the gases in it may outgas at different rates and mechanisms, depending on numerous factors. Another process of outgassing is by decomposition of the original materials. Surface gas sensors, like the ones being investigated, may alter their response depending on their outgassing characteristics and status: this makes considering outgassing of pivotal importance in understanding the response of the sensors.

One fundamental factor in understanding a particular outgassing process is to understand the nature of the interaction of the gas and the material it is attached to.

It is not possible to predict with total confidence the outgassing mechanism of a particular gas from a particular material, even when the chemical compositions and surface characteristics are known in detail. The experimentally determined outgassing rate of a particular gas from a particular material at constant temperature can be approximated by the following equation *(Hucknall et al, 2003):*

$$q = \frac{aA}{t^{\varsigma}} \tag{7.1}$$

where q [$Pa.m^3.s^{-1}$] is the throughput due to outgassing, a is a fit parameter identified as the specific outgassing rate after one hour, A [m^2] is the geometrical surface area outgassing, t [s] is time and ζ is the non-dimensional exponent of decay. For metals, glasses, and ceramics, this equation can be applied to times up to 100 hours.

The exponent of decay is an indicator of the type of mechanism of outgassing. Experimental data suggest that outgassing varies either exponentially as a function of time, inversely as a power of time, or independently of time, depending on the mechanism that is taking place.

An examination of the previous equation indicated that the bigger the area of the material exposed to vacuum, the more gas that will be released, since more gas can become attached to the surface or bulk of the material. This is a reason why vacuum chambers are designed to keep their internal surfaces to a minimum. This also indicates that a porous material will be, in principle, more prone to outgassing that one that is not, keeping all other variables constant. Outgassing decreases with time.

Pumping speed in a chamber S [m^3s^{-1}] and final pressure p [Pa] are related to q by the following equation:

$$S = \frac{q}{p} \tag{7.2}$$

If in a particular vacuum chamber there are many materials capable of outgassing at the same time and by different mechanisms, a good approximation to the total outgassing rate q_T will be the summation of the individual outgassing rates q_i, that is, we are assuming that each outgassing process is independent of each other:

$$q_T = \sum_{i=1}^{i=n} q_i \tag{7.3}$$

The activation energy of desorption (to be explored in more detail later) gives an idea of the amount of energy in the bond between the material and the gas, and it is also an indicator of the type of mechanism involved in outgassing. Table 7.1 provides approximate values for exponents of decay and activation energies. Water has an activation energy of about 0.737 eV on clean metal surfaces.

Extensive reviews of experimental methods to determine outgassing rates can be found in Kutzner *(1972),* Elsey *(1975),* Messer *(1977),* and Komiya *(1979).*

Table 7.1 Parameters of Outgassing Mechanisms *(modified from Tribble, 1995)*

Mechanism	Activation Energy (eV)	Exponent of Decay
Desorption	0.043-0.434	-1 to -2
Diffusion	0.217-0.650	-0.5
Decomposition	0.867-3.468	n/a

7.1 Outgassing to due Adsorption

Gas molecules can adsorb to a surface either by a physical or chemical process. In the first case, the interaction with the surface and the adsorbed species is due to the weak Van der Walls force, while in the second case, a much stronger chemical bond takes place.

For a physisorbed molecule, the rate of escape (Ke) from the surface can be evaluated by an Arrhenius-type equation provided the activation energy (E_A) is known *(Hucknall et al, 2003):*

$$Ke = B\exp(\frac{-E_A}{RT}) \tag{7.4}$$

where R is the Universal Gas Constant, E_A is the activation energy, and T is the absolute temperature. To outgas, the molecules of a certain chemical species requires a particular minimum activation energy. A very important result of the above equation is that an increase of temperature will increase the outgassing rate, and therefore, decrease the time required to achieve a particular pressure in a vacuum chamber.

The desorption of physically-attached molecules being a surface process, its rate will be proportional to the number of surface sites occupied by the outgassing species. According to Boltzmann, the desorption flux j is given by the following equation *(Hucknall et al, 2003):*

$$j = \nu_0 N\exp(\frac{-E_A}{RT}) \tag{7.5}$$

where v_0 is the vibration frequency of the molecule-surface bond, R is the Universal Gas Constant, and N is the number of molecules bonded to the surface.

7.2 Outgassing by Diffusion

Depending on the nature of the solid, its bulk is possible to absorb gases during its manufacturing (for example, when the material is melted or before being sintered) or later on. Gases absorbed in the bulk can alter the physical and/or chemical characteristics of many materials; therefore, baking before placing them in a vacuum chamber is a common procedure to remove absorbed gases.

A simple procedure *(Hucknall et al, 2003)* to treat outgassing by diffusion follows. We can assume a sheet of a material in which its length is significantly longer than its width 2x (see Fig. 7.1). In this scenario, two sides of this sheet of material are exposed to vacuum conditions. The number density of the gas absorbed n varies in the transversal axis X.

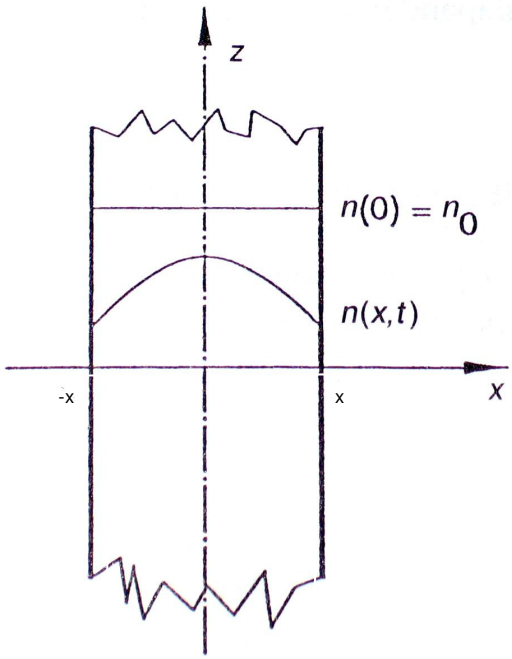

Figure 7.1. A model for diffusion-controlled outgassing *(Hucknall et al, 2003)*

The flux j will start after an initial increase in temperature to provide enough activation energy to the process, and will be symmetrical on both sides of the sheet, according to Fick's Law:

$$\frac{dn}{dt} = D\frac{d^2n}{dt^2} \tag{7.6}$$

where D is the diffusion coefficient, and the flux j is:

$$j = -D\frac{dn}{dx} \tag{7.7}$$

For long outgassing times, the following approximate solution can be obtained assuming that n_0 is the initial gas density in the solid surface:

$$j = \frac{2D}{x} n_0 \exp\left(-\frac{D\pi^2}{4x^2}t\right) \tag{7.8}$$

The temperature dependence in diffusion-controlled outgassing becomes very obvious in the following equation, in a similar fashion to the surface-controlled outgassing *(O'Hanlon, 1980):*

$$D = D_0 \exp\left(-\frac{E_D}{RT}\right) \tag{7.9}$$

In the above equation, the activation energy E_D is the term that accounts for the mechanism by which the absorbed gas enters or leaves the material in question. The amount of mass loss can by represented by the relation *(Tribble, 1995):*

$$\frac{dm}{dt} = \frac{q_e \exp\left(\frac{-E_D}{RT}\right)}{\sqrt{t}} \tag{7.10}$$

where q_e is an experimentally determined constant.

7.3 Outgassing by Decomposition

This process occurs when a compound divides into two or more simpler chemical substances, which then may outgas by any of the mechanisms described before. The chemical reaction that leads to decomposition can be triggered by a

number of factors, which include vacuum, temperature changes, and radiation. This kind of process can severely alter the characteristics of the material subject to it.

7.4 Water Outgassing

A major concern for metallic equipment designed to operate in the high to ultrahigh vacuum range is the outgassing from the walls and other surfaces inside the vacuum chamber. Whenever a vacuum system is opened to the atmosphere, all the internal surfaces will be covered with layer upon layer of water molecules. The thickness of the layer will depend on temperature, relative humidity of the air, the exposure history, conditions of the walls (porosity, cleanness, other contaminants), etc. Water molecules will bond to the surface of the chamber walls by strong chemical adsorption forces with change of a valence electron. The water molecules coming directly after will bond to the first adsorbed layer of water by physical (van der Waals intermolecular forces) adsorption forces; this bonding is facilitated by the polar nature of water. The strength of the bonding for subsequent layers of water molecules will decrease as more layers are added one on top of the other. Up to 10^{15} molecules/cm^2 of real surface area *(Berman 1996)* can absorb at the surface, but some molecules will diffuse into the passivation oxide layer, the ones that can later desorb as well.

The water layers mentioned above are present not only in the flat surfaces, but in particular in the porous ones, which have a high *surface roughness factor* (the ratio of the real to geometric surface area). This presents a problem when dealing with porous metallic and non-metallic materials, like the ZnO thick films investigated in this research, which are highly porous: the large amount of water can take a significant amount of time to outgas.

The process for a complete removal of water by outgassing in a vacuum chamber can be very long. Dylla (1993) reported that after 50 hours of pumping, the predominant species (85%) being outgassed by his chamber was water. A common procedure to reduce the amount of water in a vacuum system (and therefore to reduce the time required to reach a certain desirable pressure) is to 'bakeout' the materials and instruments that will operate that will operate under

such conditions so as to remove as much water as possible before operations begin.

The removal of the water vapor from the surfaces of the vacuum system may be considered a three-step process of: desorption, transport and pumping. At the beginning of the pump-down process, the water that is contained in the air within the chamber is mechanically removed by the action of the pumps. When a regime of free-molecular flow is reached, the process is going to be dominated by desorption of water molecules from surfaces, which can travel to another surface (and therefore resorbed) or to the pump port (and therefore removed from the chamber). If the pumping system provides enough speed, the water vapor pressure will continue to fall until equilibrium is reached, that is, the desorption rate of water from the walls and other surfaces is matched by the available pumping speed. The removal of all remaining water molecules at that point will occur at a much reduced rate, mostly when molecules in free-flow reach the pump port.

Humidity permeation from elastomers and polymeric materials such as O-rings, valve seats, etc., is a serious source of moisture. Therefore, these kinds of materials are avoided whenever possible for high vacuum applications.

A comprehensive review of the issues associated with the presence of water in vacuum systems can be found in Berman (1996). An interesting method to analytically determine the amount of water outgassed by non-metallic crystals is discussed by Mizushima (2004).

8. Basic Impedance Spectroscopy

Impedance Spectroscopy (IS) is a technique widely used to characterize sensors, and to understand their behavior; this takes advantage of its ability to measure the individual contributions to resistance and other electrical phenomena of the particular contributors to conductance, namely: grain bulk, grain boundaries, connectors, etc. In the present work, IS will not only be used for these purposes but an attempt has been made to use it to measure AO flux. A particular quality of IS is its suitability to study high resistance elements.

8.1 Introduction to Impedance Spectroscopy

Electrical resistance is the ability of a circuit element to resist the flow of electrical current. Ohm's law defines resistance (R) in terms of the ratio between voltage (E) and current (I); see Equation 8.1:

$$R = \frac{E}{I} \tag{8.1}$$

However, this relationship is valid only when dealing with one circuit element, the ideal resistor. An ideal resistor has several simplifying properties: it follows Ohm's Law at all current and voltage levels, its resistance value is independent of frequency, and AC current and voltage signals though a resistor are in phase with each other.

More complex systems require the use of impedance (Z), a more general circuit parameter. Like resistance, impedance is a measure of the ability of a circuit to resist the flow of electrical current. Unlike resistance, impedance is not limited by the simplifying properties listed above.

Impedance is usually measured by applying an AC potential to the specimen under study and measuring the current through it. Suppose that we apply a sinusoidal potential excitation. The response to this potential is an AC signal, containing the excitation frequency.

Impedance is normally measured using a small excitation signal. This is done so that the specimen's response is pseudo-linear. Linearity is described in more detail later. In a linear (or pseudo-linear) system, the current response to a sinusoidal potential will be a sinusoid at the same frequency but shifted in phase. See Figure 8.1:

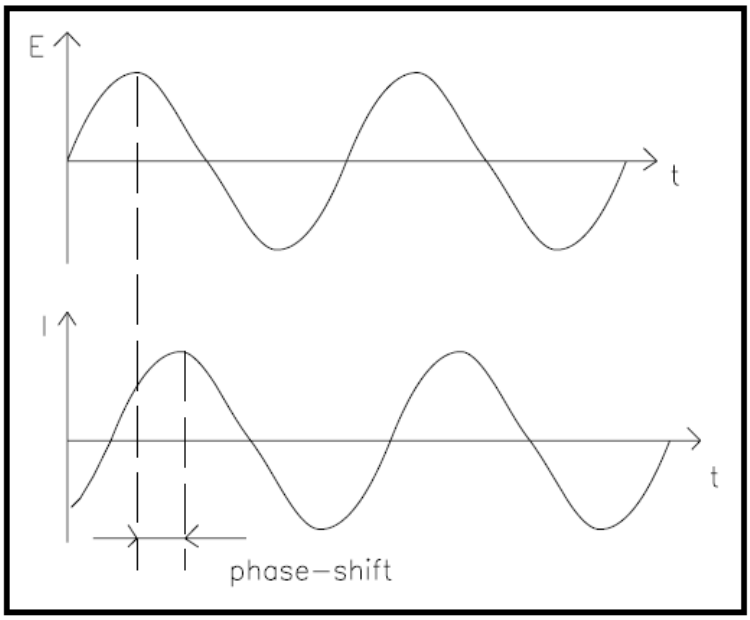

Figure 8.1 Potential (E) and Current (I) Response in a Linear System. *(Gamry Instruments, 2007).*

The potential (excitation) signal E_t can be described by the following equation, where t is time, E_0 is the maximum amplitude, and ω is the frequency (in radians per second):

$$E_t = E_0 \sin(wt) \tag{8.2}$$

The current response I_t is described by the following equation in an analogous way to the excitation signal, noting that this may be shifted in phase (Φ), and that I_0 is the maximum amplitude:

$$I_t = I_0 \sin(wt + \phi) \tag{8.3}$$

So the Impedance Z is given by the following relationship:

$$Z(\omega) = \frac{E_t}{I_t} = \frac{E_0 \sin(\omega t)}{I_0 \sin(\omega t + \phi)} = Z_0 \frac{\sin(\omega t)}{\sin(\omega t + \phi)} \tag{8.4}$$

where Z_0 is:

$$Z_0 = \frac{E_0}{I_0} \tag{8.5}$$

The solution in the time domain for Equation 8.4 is very complex, and normally requires the solution of a system of differential equations. However, the use of Fourier transformation allows the simplification of the solution in the frequency domain:

$$Z(w) = Z_0 \exp(j\phi) \tag{8.6}$$

where $j = \sqrt{-1}$. Using the Euler's formula (Equation 8.7),

$$\exp(j\phi) = \cos\phi + j\sin\phi \tag{8.7}$$

we find that:

$$Z(\omega) = Z_0(\cos\phi + j\sin\phi) \tag{8.8}$$

The real and imaginary parts of Z, the modulus, and the phase angle are therefore:

$$\mathrm{Re}(Z) = Z' = |Z(\omega)|\cos\phi \tag{8.9}$$

$$\mathrm{Im}(Z) = Z'' = |Z(\omega)|\sin\phi \tag{8.10}$$

$$\phi = \tan^{-1}\left(\frac{Z''}{Z'}\right) \tag{8.11}$$

$$|Z(\omega)| = \sqrt{(Z')^2 + (Z'')^2} \tag{8.12}$$

The frequency dependant real and imaginary components of the Impedance can then be plotted in a diagram such that of Figure 8.2 (a 'Nyquist

Plot'). In such a plot, the modulus of the impedance is shown as an arrow starting at the origin. The horizontal axis represents the real part while the vertical is the negative of the imaginary component. It is clear that to have a complete plot one has to run a frequency ω sweep from lower (right hand side) values to higher frequencies (left hand side). Impedance becomes just resistance, that is, it only has a real component, when Φ is 0; in this situation, the impedance is independent from frequency.

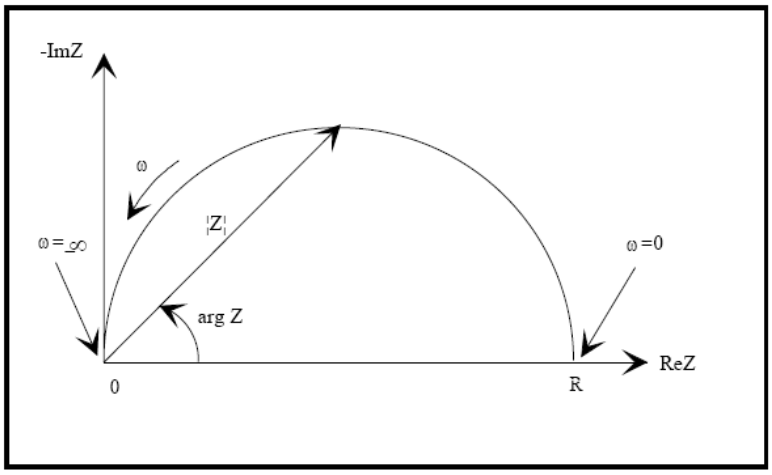

Figure 8.2 Real and Imaginary Impedance Plot. (*Gamry Instruments, 2007).*

The Nyquist plot shown in Figure 8.2 is representative of a resistor and a capacitor in parallel. More complex systems would have much more complex Nyquist plots.

A linear system is one that possesses the property of superposition: if the input consists of the weighted sum of several signals, then the output is simply the superposition, that is, the weighted sum, of the responses of the system to each of the signals. Most specimens that are studied with Impedance Spectroscopy are not linear; however, their response is approximately linear (pseudo linear) if the current response to the voltage is analyzed over a small portion of the response envelope. Experience shows that when a low voltage (less than 10 mV) is applied to a solid specimen, the response is pseudo linear in the vast majority of cases. For an electronic component, the input signal is the potential difference, and the

output signal is the measured current; therefore, if one operates IS within the linear range of the voltage to current plot (that is, under the breakdown or threshold voltage), the system will be linear.

The question that follows is how to use impedance spectroscopy to model the behavior of a particular specimen? The answer is to try to put together an equivalent circuit of resistors, capacitors, and inductors whose combined response over the same frequency range used for the impedance determination would give the same plot. This would allow to assign different elements (say a resistor and a capacitor for a grain boundary) to represent the different contributors to the total impedance.

To put together such equivalent circuit, some relationships and definitions are presented in Table 8.1:

Table 8.1 Equivalent Circuit Elements.

Element	Symbol	Impedance
Resistor	R	Z=R
Inductor	I	Z=jωL
Capacitor	C	$Z=(j\omega C)^{-1}$

It follows from the above table that the impedance equals the resistance when the former does not have an imaginary component, and therefore is independent of frequency and the response remains in phase all the time. Besides this, it is necessary to note that the impedance of different components in series and parallel combine in a fashion similar to that of resistance, as shown in equations 8.13 and 8.14:

$$Z_{series} = \sum Z_i \tag{8.13}$$

$$Z_{parallel}^{-1} = \sum Z_i^{-1} \tag{8.14}$$

Care should be taken when applying the above equations to group the imaginary and real components of the equivalent circuit to allow a Nyquist plot.

Once an equivalent circuit is being put together and the associated equations that relate the resistances and capacitances of each of the components with the real and imaginary parts of the impedance of the whole sensor are obtained, it is possible to make a plot in the complex plane, which should resemble that obtained by Impedance Spectroscopy. It should be noted that sometimes it is possible to find more than one equivalent circuit to mimic the impedance response of a specimen; in this situation, further investigation would be required to discern which equivalent circuit is best suited.

In some simple instances it is possible to directly obtain the values of the individual components and capacitances from the plot provided by the instrument; this is the case shown in the Figure 8.3 *(Asokan, et. Al., 1993),* where R_g is the resistance of the grain, R_{bg} is the resistance of the grain boundary, C is the capacitance of the grain boundary, ω is the frequency, and ω_{max} is the frequency at which the imaginary component of the impedance is maximized.

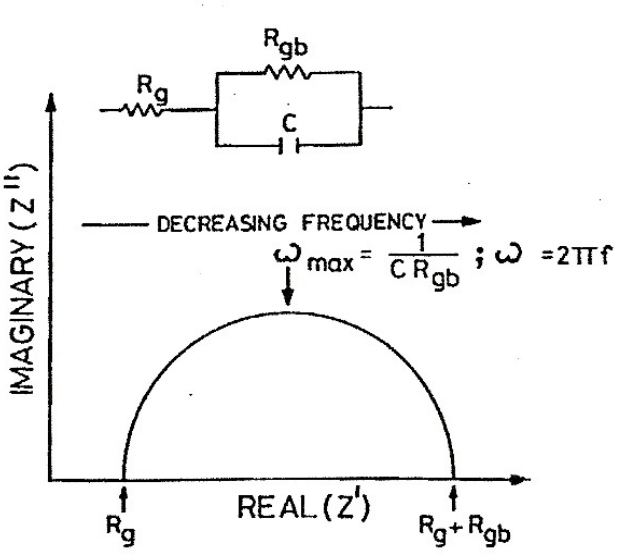

Figure 8.3 Equivalent circuit and Impedance plot for a typical ZnO varistor (*Asokan, et. al., 1993).*

A limitation of this technique is that the time constants τ' (given by the product of resistance, R and capacitance, C) of the various components in the model should differ by more than about one decade to allow reliable measurements to be made *(Andres-Verges et. al., 1997).*

There is considerable versatility, and complexity, in the analysis of AC data because the data can be analyzed in any of four interrelated basic models: impedance, admittance, electric modulus, and permittivity (the data does not differ among the different models, but just how these data are calculated and presented). The use of combined impedance and modulus spectroscopic plots can be useful for separating components with, for example, similar resistances but different capacitances or vice versa, similar capacitances with dissimilar resistances. Thus, in cases where one of the components is much more resistive than the other(s), it dominates the impedance response whereas the components that are seen most clearly in the modulus response are those with the smallest capacitance values. As an example, Andres-Verges *(1997)* report that a second pair of resistor-capacitors is only discernible when the modulus is also plotted (see the two peaks in Figure 8.4 right):

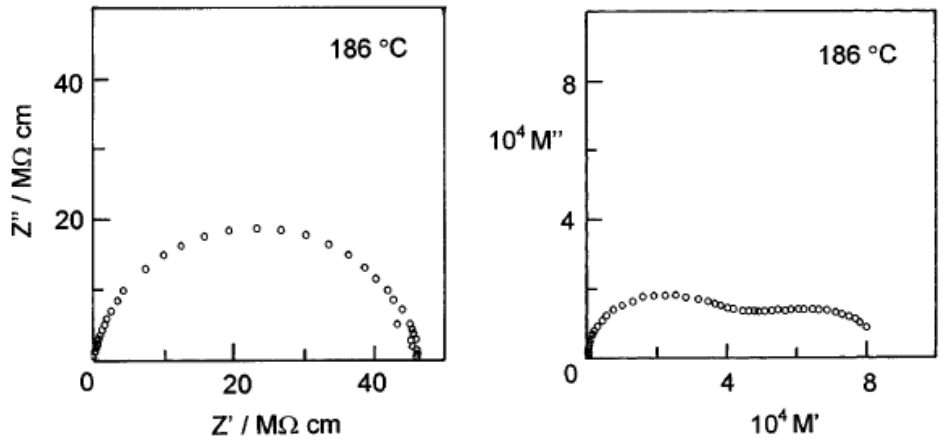

Figure 8.4 Impedance (left) and Electric Modulus (right) plots in the complex plane for ZnO varistors *(Andres-Verges, 1997).*

Another useful parameter that can be obtained from Impedance Spectroscopy, often after an equivalent circuit is found, is the activation energy; this value for either the whole specimen under study or for just of one of the

components of the equivalent circuit (for example, the grain boundary or the crystallite's grain), can be obtained by using the following equation:

$$R = R_0 \exp(\frac{E_A}{kT}) \tag{8.15}$$

where R is the resistance, R_0 is a constant, E_A is the activation energy, k is the Boltzmann's Constant, and T is the absolute temperature. If the resistance has been measured against several temperatures, the activation energy can be found by means of plotting ln(R) versus T^{-1} using Equation 8.16 (an Arrhenius plot):

$$\ln R = \ln R_0 + \frac{E_A}{kT} \tag{8.16}$$

In such a plot, the gradient is E_A/k, and the intersect with the vertical axis is $\ln(R_0)$. Examples of the use of Equation 8.16 are to be found in the literature review presented in this chapter (Section 8.2). Since resistance values will depend on absolute temperature, it follows that impedance results will also be temperature dependent in the complex plane; an example of such situation is shown in Figure 8.5 for doped ZnO varistors:

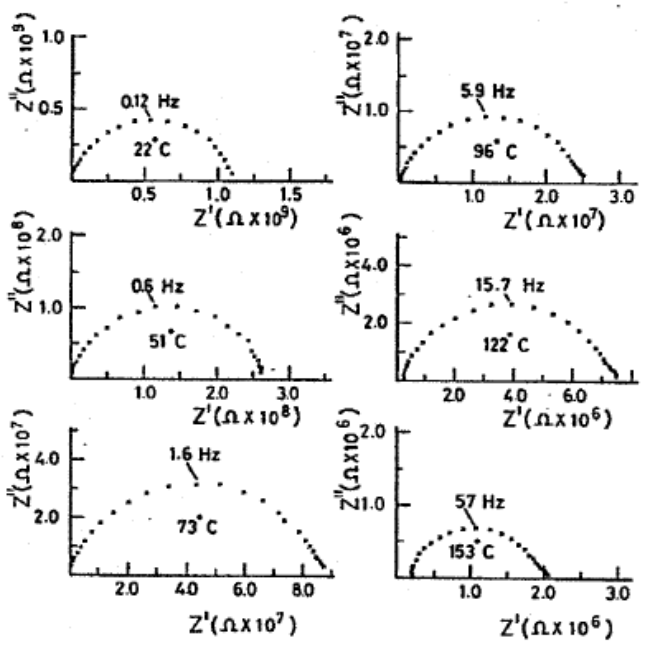

Figure 8.5 Impedance dependence on temperature for a doped ZnO varistor *(Asokan et. al., 1993).*

8.2 Literature Review

Review of the literature suggests that polycrystalline semiconductors, such as the thick film sensors investigated in this research, can be generally modeled by using an equivalent circuit such as the one shown in Figure 8.6:

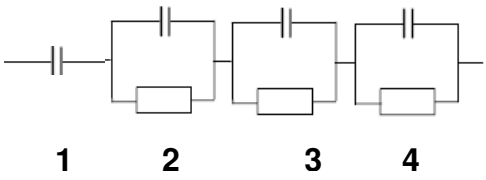

Figure 8.6 One possible electrical representation of a resistance sensor.

where:

1) Capacitance 1 represents the electrode-electrolyte interface capacitance
2) Resistance 2 and Capacitance 2 model the bulk impedance
3) Resistance 3 and Capacitance 3 model the grain boundary impedance
4) Resistance 4 and Capacitance 4 model the surface impedance

There is ample consensus in the literature that polycrystalline ZnO variable resistors have a high degree of non-linearity, that is, of non-ohmic behavior. This is attributed to double Schottky barriers (a potential barrier in a semiconductor) between adjacent grains as a result of electrons being captured in the grain boundaries *(Binesti et . al., 1986),* creating depletion regions.

In zinc oxides, initially the current increases linearly with voltage (ohmic response) and above a critical voltage called 'breakdown voltage', the current increases drastically with voltage in a highly non-ohmic behavior *(Viswanath et. al., 2001).* The non-ohmic character of this semiconductor can be expressed by means of the following empirical relationship:

$$I = kE^{\beta} \tag{8.17}$$

where I is the current, k is the Boltzmann's constant, E is the applied voltage, and β is a non-linear coefficient (which is between 25 and 50 in the breakdown region).

Conduction activation energies are an important parameter to characterize a gas semiconductor sensor, since they give the energy required for conduction and can help determine the mechanism of conduction. The activation energy of pure ZnO crystals is 0.3 eV; this value goes to 0.55 eV for grain boundaries in microphase ZnO and 0.066 eV for grain interiors *(Seitz, et. al., 1983).* However, Jose et al., *(2001)* have found that conduction activation energies for nanophase ZnO to be around 0.29eV.

Conduction and therefore the activation energy, can be altered due to physical or chemical processes in the sensor, or due to adsorption of species. Asokan et. al., *(1993)* report in their investigation of electrical-induced degradation of doped ZnO varistors that if these are exposed to a DC current density of 25mA/cm^2 for 50 hours at 150°C, the grains experience an increase in their activation energy from 0.023eV to 0.104eV (see Fig. 8.7) possibly due to migration of interstitial Zn towards the grain boundary as a consequence of the applied electric field; however, this conclusion requires further confirmation and may include causes due to the elements used to dope the varistor. They also report the grain boundaries experience a decrease in their activation energy from 0.55eV to 0.25eV possibly due to migration of adsorbed O^{-1} and O^{-2} due to the electric field away from the grain boundaries. If Zn migrates from the grains to the grain boundaries, this may lead to the formation of neutral lattice ZnO. The research carried out by Binesti et. al. *(1986)* at 115°C for 410 hours at 76% of the varistor's threshold voltage (when the device is damaged or destroyed) supports these conclusions.

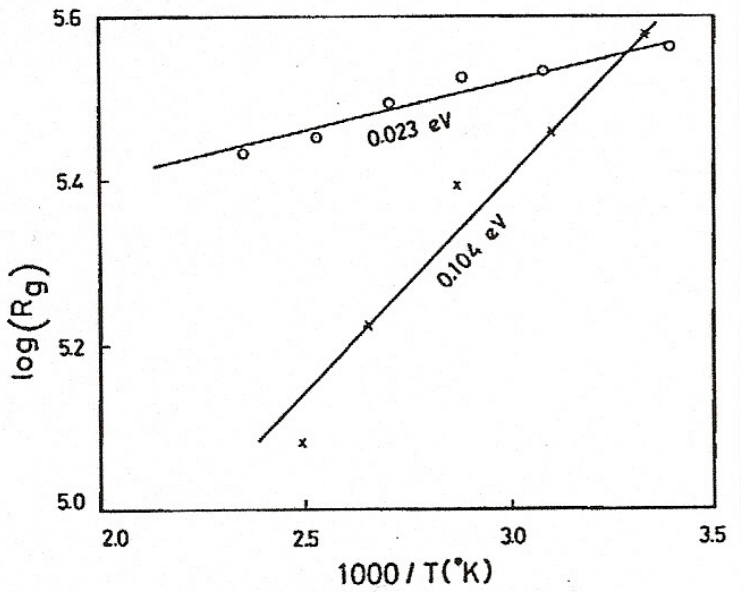

Figure 8.7 Activation Energies of the grain of doped ZnO varistors before (o) and after (x) prolonged DC current *(Asokan et. al., 1993).*

Relaxation time τ' (or time constant) is the time required for any system to reach a steady-state equilibrium; in the case of Impedance Spectroscopy, it can be considered the time required for a particular component of the equivalent circuit to provide a stable response to a change of conditions. For a resistor R and capacitor C pair, the relaxation time can be found from Equation 8.18:

$$\tau' = RC \tag{9.18}$$

Dhananjay et. al. (2007) studied the Impedance Spectroscopy profile of ZnO thin films grown on p-type Si substrates by thermal oxidation. It is reported that the relaxation time in the grain boundary is very high as compared to that of the grains, since the former is highly resistive by virtue of surface grain depletion of electronic charge, due to adsorption of other species and surface effects. The measured impedance and the proposed equivalent circuit are shown on Figure 8.8, with R_s being the resistance of the grain bulk, and R and C representing the grain boundary.

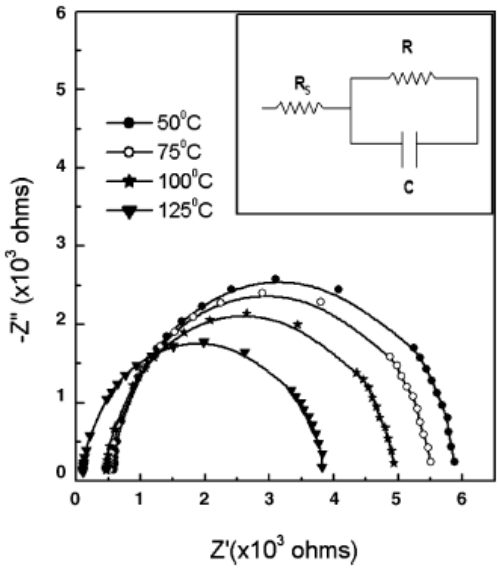

Figure 8.8 Impedance Spectroscopy profile of ZnO thin film on Si substrate at different temperatures and equivalent circuit. *Dhananjay et. al. (2007).*

Huang et. al., *(2005),* carried out studies on 5% and 10% CoFe-doped ZnO films. The results for each of the compositions of the films can be seen in Figure 8.9. For the 5% case, two pairs of resistance and capacitor in parallel (one for the grain and one for the grain boundaries), in series with each other, provide an adequate representation of the films behavior. However, for the 10% case, in addition to the above pairs, R_{mg} represents the formation of CoFe clusters, while the pair in parallel R_{mo} and C_{mo} suggests the existence of an interface between these clusters and the host oxide. See Figure 8.9.

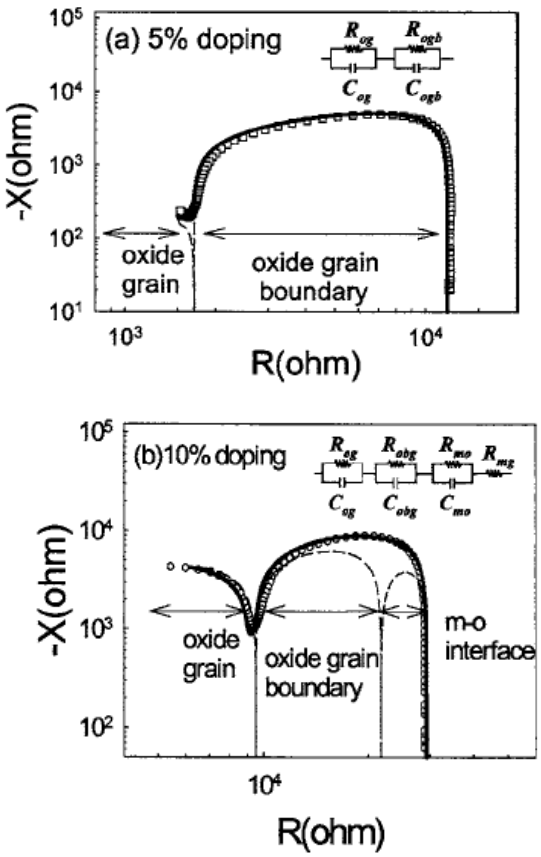

Figure 8.9 Impedance Spectroscopy of 5% and 10% CoFe-doped ZnO films. *Huang et. al., (2005).*

Hong et. al. *(2004),* in their research on Mn_3O_4-doped ZnO varistors, maintain that a suitable equivalent circuit is two parallel resistor-capacitor elements connected in series. The same findings have been published by Shao et. al., *(2003).*

Viswanath et. al. *(2001)* have studied ZnO varistors with an insulating layer around each crystallite created by means of the diffusion of other elements into the grain boundary (see Figure 8.10).

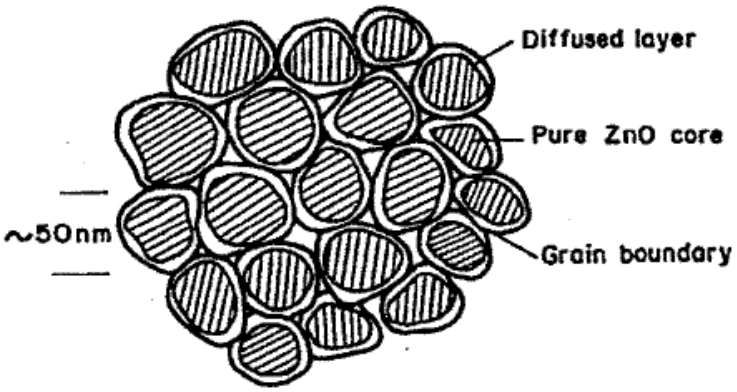

Figure 8.10 Crystallite structure of diffusion-doped ZnO varistors. *Viswanath et. al. (2001).*

These varistors were studied under both molecular oxygen and molecular nitrogen atmospheres; the resistance values obtained in the former were significantly higher than those in the later as seen in Figure 8.11.

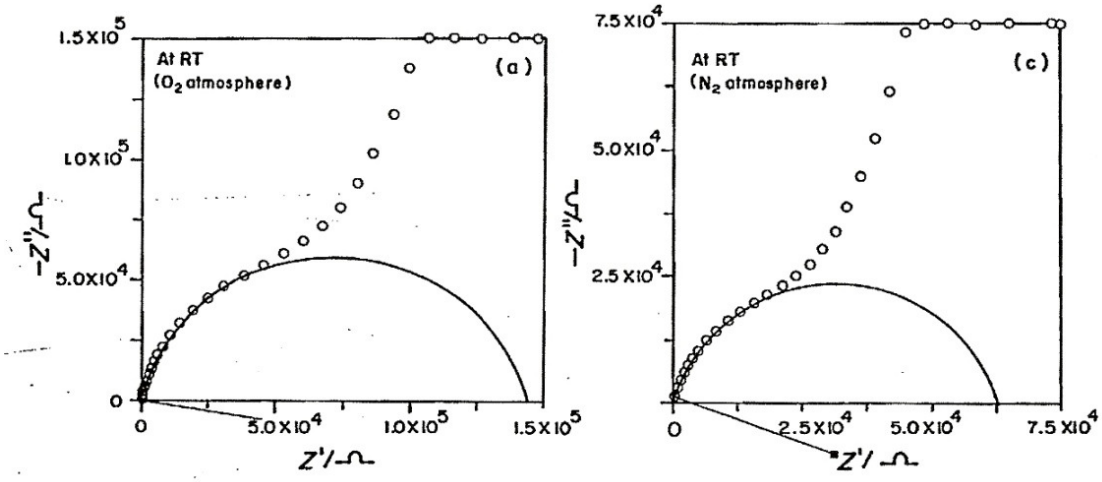

Figure 8.11 Effect of different gases on Impedance Spectroscopy on diffusion-doped ZnO Varistors. *Viswanath et. al. (2001).*

The corresponding equivalent circuit was found to be $R_{g(core)}$ for the pure ZnO grains, a resistor and capacitor pair in parallel for the diffused layer (dl), and another pair for the grain boundary (gb); see Figure 8.12.

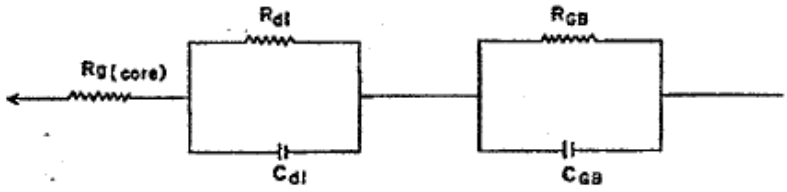

Figure 8.12 Equivalent circuit for diffusion-doped ZnO Varistors. *Viswanath et. al. (2001).*

Lee et. al., (1995), report in their study of nanophase ZnO that a suitable equivalent circuit is two parallel resistor-capacitor elements connected in series, as found by other researchers, and that an increase of the partial pressure of molecular oxygen increase the resistance of the grain boundaries (which have the dominant effect); this latter effect is attributed to the adsorption of the oxygen at the surface. The value of grain boundary resistance found was in the $10^7\Omega$ range, for the diffusion layer was in the $10^5\Omega$ range, while the value for the bulk grain can be neglected compared to these two former values. The activation energy for the grain boundary has been found to be 0.57 eV independent of the O_2 partial pressure. See Figure 8.13.

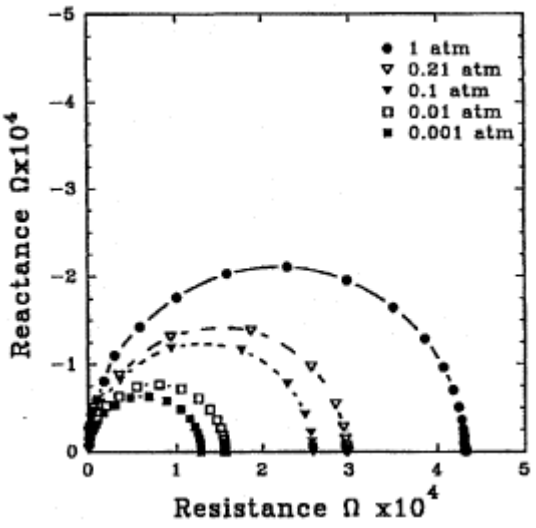

Figure 8.13 Effect of molecular oxygen partial pressure on grain boundary resistance in nanophased ZnO. *Lee et. al. (1995).*

Dachun et. al. *(1999)* indicate that the resistance between the ZnO grains and the electrode interface can normally be neglected if compared to the total resistance in between grains.

It has been shown that surface barriers can form in between ZnO grains and gold connectors *(Mead, 1965; Fabricius et al., 1986).* But there is also ample evidence *(Freer, et al., 2004)* that the effect of those surface barriers can be isolated from the resistance of the bulk and grain boundaries by means of impedance spectroscopy.

9. Development of a Semiconductor Gas Sensing Model

The purpose of this research is to develop of basic ZnO thick film sensor capable measuring AO flux. For this purpose, a model that explains the change of resistance as the AO impinges on the sensor is required.

9.1 Basic Model Formulation

The model described in this section relies heavily on the adaptation of Osborne *(1999)* for ZnO thin films of the model developed by Langmuir et al. *(1918),* which has been called 'the balistic model'. This model is formulated from first principles.

Let Co be the surface density of atoms [atoms/m^2] at the surface of the crystal, and a_∞ is the maximum density of adsorbed atoms that the surface of the crystal can take. So the maximum fraction of surface sites occupied by adsorbed atoms is:

$$\frac{a_\infty}{Co} \tag{9.1}$$

Now, let a(t) represent the density of atoms adsorbed at the sensor surface at a given time t; therefore, the fraction of surface sites at a time t in the sensor is given by:

$$\frac{a(t)}{Co} \tag{9.2}$$

The fraction of empty surface sites in the sensor at a particular time t is then:

$$\left[\frac{a_{\infty}}{Co}-\frac{a(t)}{Co}\right] \tag{9.3}$$

It is also known that not all atoms that reach the surface of the sensor will adsorb. Let us then define a scattering coefficient γ representing the fraction of impacting atoms that reflect from the surface. Let us also define the flux of impinging atoms into the surface as F [atoms.s^{-1}.m^{-2}]. Therefore the rate of adsorption is determined by:

$$\left[\frac{a_{\infty}}{Co}-\frac{a(t)}{Co}\right]\left((1-\gamma)F\right) \tag{9.4}$$

It is also necessary to describe the rate of desorption of atoms. So if τ is the mean residency time of atoms at the surface, then the rate of desorption is given by:

$$\frac{a(t)}{\tau} \tag{9.5}$$

At equilibrium, the rate of desorption and of adsorption are the same. In a non-equilibrium status, the rate of change of surface atom density may be found by the difference between equations (9.4) and (9.5):

$$\frac{da(t)}{dt}=\left[\frac{a_{\infty}-a(t)}{Co}\right](1-\gamma)F-\frac{a(t)}{\tau} \tag{9.6}$$

Now one must integrate equation (9.6) for a definitive time t, and for the density of adsorbed atoms a:

$$\int_0^a\left\{\frac{Co\,\tau}{\left[a_{\infty}(1-\gamma)F\tau\right]-a(t)\left[(1-\gamma)F\tau+Co\right]}\right\}da=\int_0^t dt \tag{9.7}$$

By means of formula (9.8) we can find equation (9.9).

$$\int\frac{A}{B-Dx}dx=-\frac{A}{D}\ln(B-Dx) \tag{9.8}$$

$$t = \frac{Co\tau}{(1-\gamma)F\tau + Co} \ln\left\{\frac{a_\infty}{a_\infty - \left(1 + \frac{Co}{(1-\gamma)F}\right)a(t)}\right\} \tag{9.9}$$

It is possible to find the atomic concentration at the surface at time t from equation (9.9):

$$a(t) = \left(\frac{a_\infty}{1 + \frac{Co}{F\tau(1-\gamma)}}\right) * \left(1 - \exp\left[-t\left(\frac{F(1-\gamma)}{Co}\right)\left(1 + \frac{Co}{F\tau(1-\gamma)}\right)\right]\right) \tag{9.10}$$

If we differentiate equation (9.10) with respect of time, we find the rate of change of adsorption evaluated at t=0 is directly proportional to the flux:

$$\frac{da}{dt}_{t=0} = \left(\frac{a_\infty}{Co}\right)(1-\gamma)F \tag{9.11}$$

The above equation relies on several assumptions. For purposes of measuring the flux impinging on the sensor, one has to determine the initial change of adsorption rate, which in turn requires that no previously adsorbed atoms or molecules of any kind. This also requires the flux to be constant, the average atomic residence time at crystallite surface to be constant, surface geometry of sensors not changing in time, and the scattering coefficient (fraction of impacting atoms that reflect) of impinging species does not change (this assumption will only be valid at the very beginning of the exposure, since after time passes, some positions in the surface will be occupied and therefore the probability of adsorption decreases with time).

The question that remains is how to measure the rate of change of adsorbed atoms at the surface of the sensor at time=0? We will now attempt to relate this change with resistance or impedance, which can be easily measured.

To reduce the number of constants to work with let us define a* as Co/a_{∞}. Therefore equation 9.11 becomes, after suitable rearrangement:

$$F = \frac{a^*}{(1-\gamma)} \frac{da}{dt}\Big|_{t=0} \tag{9.12}$$

In the particular case of ZnO and adsorption of AO, only the adsorbed atoms that become ionized (by accepting one electron from the sensor) will affect the conductivity of the material. If we define α as the fraction of adsorbed atoms that become ionized, and i as the surface density of ions, we get:

$$\frac{di}{dt}_{t=0} = \alpha \frac{da}{dt}_{t=0} \tag{9.13}$$

But we also need to take into consideration that the increase of ionic atoms in the surface will decrease the surface electronic density n_s:

$$\frac{di}{dt}_{t=0} = -\frac{dn_s}{dt}_{t=0} \tag{9.14}$$

Using equations 9.13 and 9.14 into 9.12 we get:

$$F = -\frac{a^*}{\alpha(1-\gamma)} \frac{dn_s}{dt}_{t=0} \tag{9.15}$$

The conductivity in a semiconductor σ is given by:

$$\sigma = n_b e \mu \tag{9.16}$$

where e is the electronic charge and μ is the mobility of the charge carriers, in this case, the electrons, and n_b is the density of electrons in the bulk. Therefore the change in conductivity with time is:

$$\frac{d\sigma}{dt} = e\mu \frac{dn_b}{dt} \tag{9.17}$$

The number of electrons removed from the surface due to adsorption ΔN_s is the same as the decrease in the number of electrons available for conduction (in the bulk) ΔN_b, and we find that:

$$\Delta N_s = \Delta N_b = \Delta n_b V \tag{9.18}$$

where V is the volume of the sensor. If d is the sensor thickness, b the breadth of the sensor, and l the distance between electrodes we find, after differentiating against time:

$$\frac{dN_s}{dt} = \frac{b}{d}\frac{dn_b}{dt} \tag{9.19}$$

So the change of conductance with time is given by replacing 9.19 into 9.17:

$$\frac{d\sigma}{dt} = \frac{e\mu d}{b}\frac{dN_s}{dt} \tag{9.20}$$

Since N_s and n_s are related by volume, after differentiation by time we get:

$$bl\frac{dn_s}{dt} = \frac{dN_s}{dt} \tag{9.21}$$

we can replace 9.21 into 9.20 and then into 9.15 to get:

$$F = -\frac{a^*}{\alpha e\mu l d(1-\gamma)}\frac{d\sigma}{dt}_{t=o} \tag{9.21}$$

Now since the conductivity σ is related to resistance R and resistivity ρ by:

$$\sigma = \frac{1}{\rho} = \frac{l}{RA} = \frac{l}{Rbd} = \frac{gl}{bd} \tag{9.22}$$

where A is the cross-sectional area, and g is conductance. Replacing equation 9.22 into 9.21:

$$F = -\frac{a^{*} l}{\alpha b e \mu (1-\gamma)} \frac{dg}{dt}_{t=o} \tag{9.23}$$

Equation 9.23 will therefore allow the determination of AO flux by measuring the resistance change at the beginning of exposure, and then converting that value to change of conductance with time at the beginning of the exposure. However, each sensor would need to be calibrated before actual flux determination with a source of a known flux so as to determine the magnitude of the constants in equation 9.23.

A limitation of this model is that a precise measurement of resistance is required. This may not be possible for films on ZnO in which gold is used for the contacts. As mentioned in Section 10.2, surface barriers may form in the interface between the gold and the ZnO, which could preclude accurate measurements by the sensors matter of this research, if such barriers are present. The following section tries to overcome the limitation of this model.

9.2 Ballistic Model modified by the use of Impedance Spectroscopy

It has been shown that surface barriers can form in between ZnO grains and gold connectors *(Mead, 1965; Fabricius et al., 1986).* But there is also ample evidence *(Freer, et al., 2004)* that the effect of those surface barriers can be isolated from the resistance of the bulk and grain boundaries by means of impedance spectroscopy. It is also known that if the resistance readings of a sensor obey Ohm's Law, those barriers are not present. Therefore, sensors that obey Ohm's Law can use the ballistic model described in the preceding section.

However, it is typical that sensors only show ohmic behavior for a limited voltage range (from zero up to the threshold value) for a number of reasons; so after this threshold value, the measurement of resistance can be compromised by the appearance of surface barrier. And it is even possible that those barriers are present at all voltages. So it is required to find the means to isolate the effect of contact to sensor surface barriers.

The obvious choice is to use impedance spectroscopy to find an equivalent circuit of resistances and capacitances to model the resistance in the contact to

sensor inter phase, the bulk, and grain boundaries. Once this surface barrier effect is isolated, the change of bulk and grain boundary resistance can be used (depending on the nature of the sensor) to measure flux. In sensors where the overall change of resistance with time is dominated by the resistance of the grain boundaries, the former parameter can be used to estimate flux in place of overall resistance rate of change as long as the magnitude of the error introduced is known and acceptable.

Using impedance introduces another form of error: it takes from a few seconds to a few minutes to complete a frequency sweep with enough detail to obtain impedance measurements. Each data point in the resistance versus time plot will require a complete frequency sweep. The AO flux will have to be blocked or assume this as an error during the sweep, but regardless of the technique used, the margin of error will increase by the length of time it takes to make an impedance measurement.

10. Zinc Oxide Gas Sensors

The purpose of this chapter is to present a brief description of Zinc Oxide and to provide an overview of the variables that influence its electrical resistance. This review will include references to work done in single crystals, as well as both thin and thick films. Zinc oxide films have successfully been used as sensors for flammable gases like hydrocarbons, alcohols, hydrogen gas and carbon monoxide *(Nunes et al., 2001)*, but these applications are beyond the scope of the present work.

The first and most important characteristic of a semiconductor like ZnO is that it is of an n-type; it is under investigation that under some exceptional circumstances like heavy doping with other components and temperatures between 573 and 1000 K *(Chandra et al, 1967)* this can change, but this is not expected to occur within the scope of this research. Charge-carrier providers are Zn atoms that occupy interstitial positions *(Royal et al., 1968).*

10.1 Zinc Oxide

Zinc oxide is a chemical compound with formula ZnO. It is nearly insoluble in water but soluble in acids or alkalis. It occurs as white hexagonal wurzite lattice crystals, with lattice constants (dimensional lengths) a_1 = 3.25 Å, a_3 = 5.19 Å (*Heiland et al., 1959*).

It remains white when exposed to ultraviolet light. Crystalline zinc oxide exhibits the piezoelectric effect (the ability of certain crystals to generate a voltage in response to applied mechanical stress), is luminescent under the bombardment of electrons, and is light sensitive. These properties have led to the employment of ZnO in a diverse range of scientific and technological applications. Zinc oxide occurs in nature as the mineral zinctite.

Zinc oxide has a molar mass of 81.37 g/mol, a density as a solid of 5.606 g/cm^3, and a melting point of 1975°C. It is a semiconductor with a band gap of 3.2

eV (387 nm, deep violet/borderline UV). A common application is in gas sensors. Its crystalline structure is depicted in Figure 10.1.

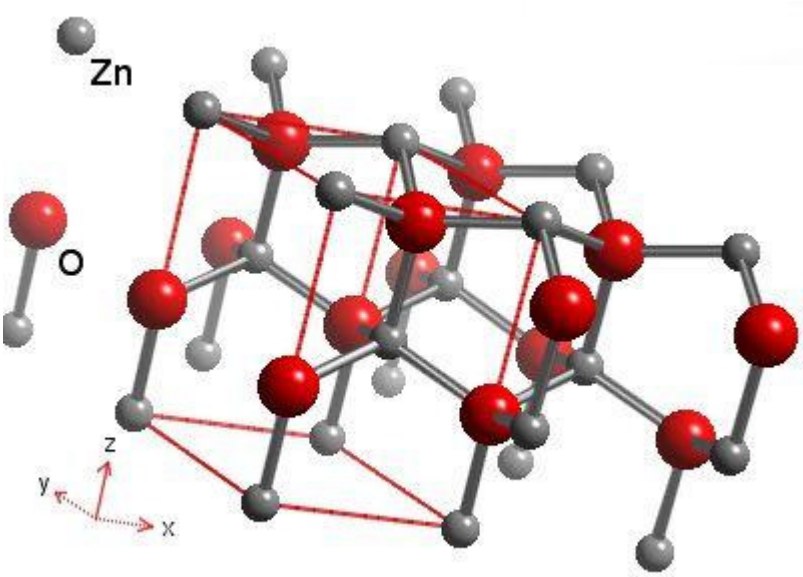

Figure 10.1 Zinc Oxide Crystalline Structure *(picture taken from Webelements.com)*

10.2 Relationship between Voltage and Resistance

Osborne *(1999)* reported in his work, that the thin film ZnO sensors respond to different DC voltages following a linear relationship between voltage and current measured under vacuum conditions in accordance with ohms law. A typical result from his experiments can be found in Fig. 10.2.

These results indicate that the resistance of the thin film sensors would not vary with different voltages applied to them (ohmic behavior). It has been reported *(Mead, 1965; Fabricius et al., 1986)* that gold can form a surface barrier when in contact in ZnO, a condition that would preclude an ohmic response on a sensor.

Polycrystalline sensors of ZnO may be modified by the presence of additives so as to perform in a specific manner. Routbort et. at., *(1995)* report that the response of these sensors may deviate from a linear and ohmic response when a voltage is applied to them.

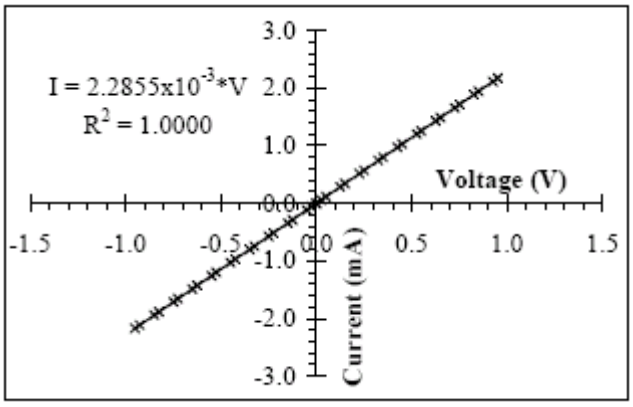

Figure 10.2 I-V plot for thin ZnO sensors *(Osborne, 1999).*

10.3 Ultraviolet Radiation

It has been widely reported, that UV causes surface lattice oxygen atoms to leave the surface of the oxide; because of the significant band gap (about 3.2 eV) most radiation absorption will take place in the UV region; thin zinc oxide films have been used as UV detectors *(Fabricius et al., 1986).* The process is described by the following reaction *(Thomas et al., 1958),* where h is the Plank's Constant, and v is the radiation frequency:

$$ZnO^{2+} + O^{2-} + 2h\nu \rightarrow \tfrac{1}{2}O_2 + Zn \qquad (10.1)$$

Subsequent ionization of interstitial zinc provides electrons that increase the conductivity of the crystal:

$$Zn \rightarrow Zn^{+} + e^{-} \qquad (10.2)$$

It has been reported *(Kohl, 1996)* that once an important loss of oxygen atoms on the surface of a film has occurred due to exposure to UV radiation, and provided the temperature is at least of 900°C, some of the atoms of oxygen from the bulk of the film will migrate towards the surface to replace the ones lost from the surface; this process irreversibly changes the resistance of the film. This being a temperature significantly higher than those encounter in the present research, migration should not be of concern for the present work.

Zinc oxide can also absorb UV light directly, and when this energy is higher than the band gap energy, an electron(e^-)-hole(H^+) pair is created *(Melnick, 1957):*

$$h\nu \rightarrow \mathrm{H}^+ + e^- \tag{10.3}$$

The above reaction will cause the concentration of charge carriers to increase which will in turn increase the conductance of the material. This process is entirely reversible, and reverses once the radiation ceases to reach the ZnO.

It should also be mentioned that UV radiation can increase the temperature of a film of ZnO crystals and as a result decrease its resistance.

It has been reported that thin films have a significantly larger and faster photoconductivity response than thick films *(Takahshi et al. 1994),* due to the limited penetration of UV radiation, which Heiland *(1961)* found to be about 0.1μm; this is consistent with a surface effect. This penetration depth should be understood as the maximum depth on a particular sensor where the availability of negative charge carriers increases due to UV radiation impinging on the sensor's surface.

10.4 Adsorption of Molecular Oxygen

In the absence of UV radiation, molecular oxygen can be adsorbed in the surface of ZnO according to the following equation *(Takahashi et al., 1994):*

$$O_2(gas) + e^- \rightarrow O_2^-(ad) \tag{10.4}$$

The gaseous molecular oxygen would adsorb by capturing an electron from the surface of the oxide, which should be available in an n-type semiconductor; this phenomenon will increase the resistance of the material, since it will create a depletion zone of charge carriers near the surface. The process can be reversed by UV radiation of sufficient energy, according to:

$$h^+ + O_2^-(ad) \rightarrow O_2(gas) \tag{10.5}$$

10.5 Adsorption of Atomic Oxygen

Upon impinging the surface of a sensor, AO may get physisorbed, and therefore stay in the surface by means of a weak physical attraction of the van der Waals type, of an order of magnitude of a fraction of an electron-volt; there is not a proper chemical bond in this type of interaction, but the force is of a long range and may allow the build-up of several layers of adsorbed atoms.

After some time, an oxygen atom may become chemisorbed, a process that involves the transfer of some of the negative electric charge to the adsorbed atom, which will create a strong chemical bond. This will create a situation similar to the surface states discussed in Chapter 6, decreasing the availability of charge carriers for conduction (and therefore increasing the resistance of the crystal); some of the electrons will transfer to an energetic position under the conduction band of the oxide. This strong attraction is of short-range type; the number of positions available for chemisorption is limited, and it is unlikely that more than one layer of adsorbed atoms will form; therefore, it is said that the surface has ‘saturated’.

The adsorbed atoms will ionize due to the negative charge transfer, which explains the strong ionic bond to the surface and the reduced likelihood of desorption, which can nevertheless take place by suitable heating. But adsorption will also create a depletion layer of electrons, with a depth in between 0.1 to 10 μm, that although small, affects the conductivity of the crystal; a consequence of this is that the thicker a sensor is, the less sensitive it will be to chemisorbed AO, since the conductivity of the bulk of the sensor may shunt the observation of the reduced conductance due to the adsorption; consequently, thin films will be more sensitive than thick ones of the same surface area, depending as well on crystallite sizes.

It should also be mentioned that resistance response due to AO chemisorption is very dependant on crystallite size and the porosity of the film, since these variables can significantly change the amount of surface exposed to AO.

Different techniques *(Arshak et. al., 2005; Caillaud et.al., 1991; Fabricius et. al., 1986)* have been developed over the years for the deposition of zinc oxides on different substrates so as to be used in a variety of ways. Grain sizes can vary dramatically from technique to technique. If the grain size is small enough that depletion layers due to adsorbed oxygen affect a significant amount of the volume of the conducting material, the number of electrons available for conduction can significantly decrease, while the sensitivity of the sensor increases.

It is interesting to compare the results of the chemisorption of molecular vs. atomic oxygen. Nahr et al., *(1971)* found a response between 10^2 to 10^3 times higher for the latter than the former on single ZnO crystals. This may be explained by the fact that atoms of oxygen wish to acquire a couple of electrons to achieve a noble gas electronic configuration, while the atoms in a molecule of oxygen have already attained that configuration.

10.6 Atomic Oxygen Migration

The diffusion of oxygen and zinc atoms in ZnO has been studied in depth; Newman *(1981)* provides a good review on this matter. Just a general overview will be presented here.

Equation (7.9) can be reformulated and expressed in terms of the Boltzmann's constant to obtain a "diffusion coefficient', which is defined by Equation 10.6:

$$D = D^0 \exp(\frac{-E_A}{kT}) \tag{10.6}$$

where D is the diffusion coefficient [m^2/s], D^0 is the frequency factor [m^2/s], Q is the activation energy [J], k is the Boltzmann's constant, and T is the absolute temperature [K]. The time for a species to diffuse can be found by using Equation 10.7

$$t = \frac{y^2}{D} \tag{10.7}$$

where y is the diffusion depth [m].

Research by Erhart, et. al., *(2006)* has shown not only that interstitial atomic oxygen migrates in the structure of ZnO oxides, but also that the atoms with a single negative charge are those favourite for such migration to occur, as depicted in Figure 10.2. It has been reported by Tuomisto, et. al., *(2005)* that the activation energy for the neutral oxygen vacancy is 1.8 eV.

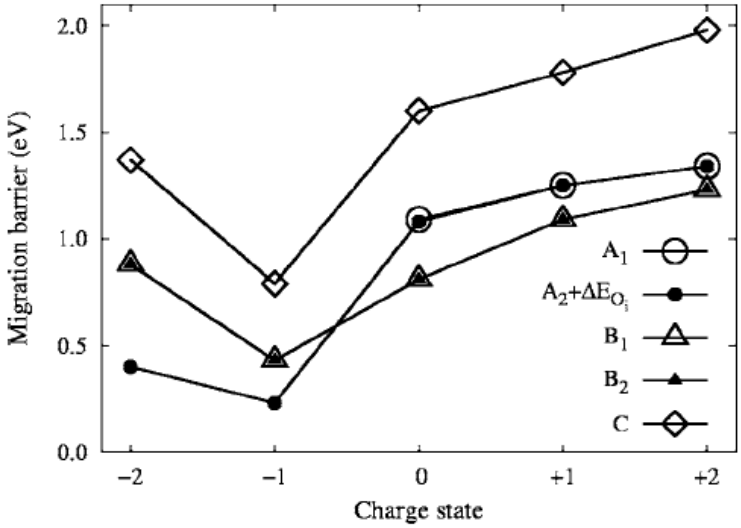

Figure 10.2 Charge state dependence of oxygen interstitial migration enthalpies. Graph shows this dependence for different migration patterns. Erhart, et. al., *(2006)*

10.7 Response to Changes in Pressure

Wortman et. al., *(1972)* performed a detailed work on the response of thin films of ZnO (deposited by RF sputtering over a substrate) to atmospheric gases at different pressures. The film's resistance will change according to Equation 10.8:

$$R = R_0 \exp(\frac{E_A}{kT}) \tag{10.8}$$

where R is the resistance, R_o is temperature independent constant, E_A is the activation energy for the process, k is the Boltzmann's constant, and T the absolute temperature. Wortman et. al., *(1972)* found that R_o and E_A increase with an increase of the partial pressure of molecular oxygen in air. The decrease in the concentration of charge carriers, and hence a further increase in resistance, is a consequence of the trapping of electrons at the surface by the adsorption of

oxygen, both molecular and atomic (there a negligible concentration of AO in air). Equation 10.8 also shows that an increase in temperature will cause a decrease in resistance, keeping all other variables constant.

Figure 10.3 provides a clear exposition of the relationship between partial pressure of air and resistance; the temperature dependence is also demonstrated. The activation energy measured in the curve with the lowest resistance (and lowest pressure as well), was measured to be 0.047 eV; published values for the first ionization energy for interstitial zinc atom (which would transfer an electron to adsorbed molecules of oxygen) range from 0.040 eV to 0.050 eV depending on the structure of the grains.

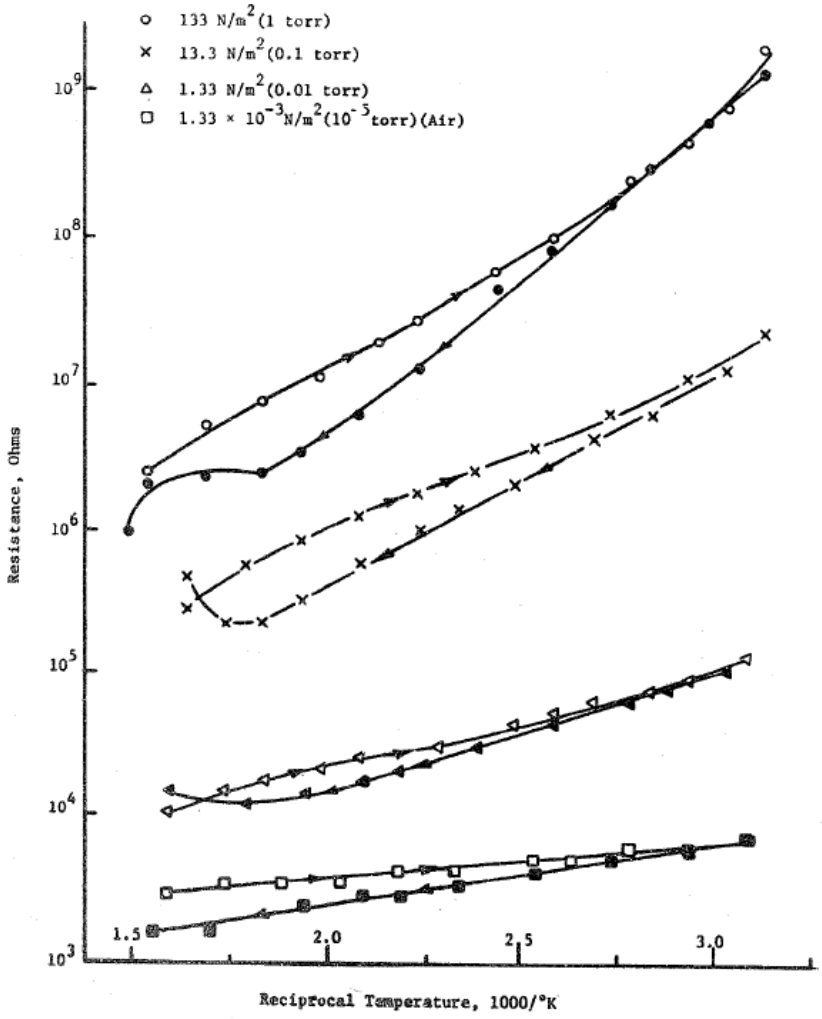

Figure 10.3 Resistance dependence on Oxygen Partial Pressure in Air and Temperature, Wortman et. al., *(1972).*

As the number of adsorbed oxygen atoms or molecules increase on the surface, so will be the probability of repulsion among them. This circumstance will also result in an increase in the activation energy (a consequence of the increase in partial pressure of air); eventually, the surface will saturate and prevent further adsorption. The activation energies found by Wortman et. al., *(1972)* are presented in Table 10.1.

Table 10.1 Change in Activation Energy with Oxygen Partial Pressure, Wortman et. al., *(1972)*

Pressure [Pa]	**Activation Energy** [eV]
1	0.05
10^4	0.2
10^5	0.3

Using the same reference, and after a long analysis that goes beyond the scope of the present work, it can be proposed that the concentration of O_2 at the surface of the film $[O_2]$ is a function of the number of available sites at the surface per unit area n_s, the partial pressure of O_2 P_{O2} and the total air pressure P_T:

$$[O_2] = \frac{n_s P_{O_2}}{P_T} \tag{10.9}$$

The fact that ZnO films can operate as piezoelectric detectors/transducers is well documented. Piezoelectric zinc oxide thin films are used as a transducer material in mechanical sensors, acoustic wave devices (it can also generate this type of waves), acoustic microscopy and acousto-optic devices *(Cimpoiasu et al., 1996; Schwesinger et al., 2005).*

10.8 Response to Humidity

It has been reported that the presence of water vapour in the gas (either pure molecular oxygen or nitrogen) in which thin zinc oxide sensors were tested,

will increase the resistance of the sensors while exposed to UV radiation *(Melnick, 1957).* It has been proposed that the water vapour decreases the concentration of charge carriers while under UV radiation according to the following mechanism *(Takahashi, 1994):*

$$H_2O + 2h^+ + 2e^- \rightarrow H_2 + \tfrac{1}{2}O_2 \qquad (10.10)$$

An alternative mechanism would be the oxidation by water of the interstitial Zn atoms (created by the UV radiation) which will also reduce the concentration of electrons and thus reduce the conductivity of the material.

Wortman et. al., *(1972)* report an increase in resistance of thin ZnO films with an increase in the partial pressure of water vapour in air. He attributes the change to the chemisorption of H_2O molecules on the surface of the films, which will 'trap' some of the electrons.

10.9 Response to Other Gases

Wortman et. al., *(1972)* report that thin films of ZnO do not significantly react to a variation in the pressure of either molecular nitrogen or argon, at room temperature. This contrast with the response of adsorbed oxygen can be explained by the nature of the interaction of N_2 or Ar with the surface of a film: having both the electronic configuration at the atomic level of noble gases, they will not accommodate an electron from the ZnO, which will not allow a chemical adsorption, but rather a physical one. This physisorption involves much weaker forces and of a reduced range than chemisorption; also, no significant reduction of the concentration of electrons takes place, and therefore, there is no significant increase in the resistance of the films.

There is documented evidence that thin films of ZnO respond to the presence of molecular hydrogen. Research performed by Yamazaki et at., *(1993)*, show that the resistance of thin films (that were deposited by ion-beam sputtering over a substrate) increase as a consequence of a partial pressure of H_2 in dry air; this increase in resistance is attributed to the creation of a depletion layer of

electrons in the surface of the film, in a similar fashion as adsorbed oxygen. In this experiment, the sensitivity of the sensor dropped as its thickness increased, which is consistent with the presence of a depletion layer.

It has been reported *(Trivikrama Rao et al., 1999)* that thick and thin films of ZnO at about 300℃ respond to trace amounts of reactive gases like hydrocarbons, carbon monoxide, methane, ammonia, and oxides of sulphur, nitrogen, and chloride; it has also been reported *(Arshak et al., 2005)* the use of thick zinc oxide films to monitor the concentration of propanol, methanol, and ethanol at temperatures of 25℃ to 50℃. A review on these effects is considered to be beyond the scope of this work.

11. Sensor Development

11.1 Historical Background

This research project has its immediate predecessor in the work performed by Osborne *(1999)* for his doctoral thesis in the University of Southampton. He developed a series of thin films that proved to be responsive to AO, as well as being capable of regeneration by suitable heating. Thin film technology allows the manufacture of sensors that can be small, with very modest requirements in terms of electronics and power. Nonetheless, Osborne's sensors presented a significant hysterisis upon repeated exposure, and also significant variability in their initial resistance.

Osborne's work in turn was inspired by the experimental work carried out by Gabriel *(1997)* in which he recorded the increase in resistance of a single ZnO crystal exposed to AO.

However, thick film technology presents a series of advantages to be exploited in the design of sensors. The printing of films can be done at atmospheric conditions with simple instrumentation, and the firing only requires a furnace without a controlled environment. All this makes thick film technology very affordable and allows the simple and rapid preparation of sensors. These features were exploited in the present work.

11.2 Sensor Fabrication

The design was based on the thin film sensors of Osborne *(1999),* but with many differences: the substrate and heaters were the same, but deposition took place by screen printing (later to be explained in more detail). A thick film of ZnO was deposited over an alumina substrate; in between these two, an interdigitated gold array (thickness of about 1 μm) was printed so as to provide electrical contacts with the film. A heater of the resistor type was printed on the other side of

the substrate to provide temperature control and the necessary heat for regeneration.

Substrates are made of commercially available alumina (supplied by Coors Tek, catalogue code USO-LS/1), better than 98% pure.

Initially, a gold film used for conduction is deposited over the substrate. This gold film has a very fine interdigitated structure so as to decrease the resistance of the ZnO sensor once it is deposited over. The gold (ESL 8880-H) is deposited by a screen printing technique and then fired at 850℃ to assure its adherence to the substrate; final thickness will be 1 μm approximately. Four equidistant gold films are printed in each substrate. Fig. 11.1 is a diagram of one of these interdigitated films (dimensions in mm):

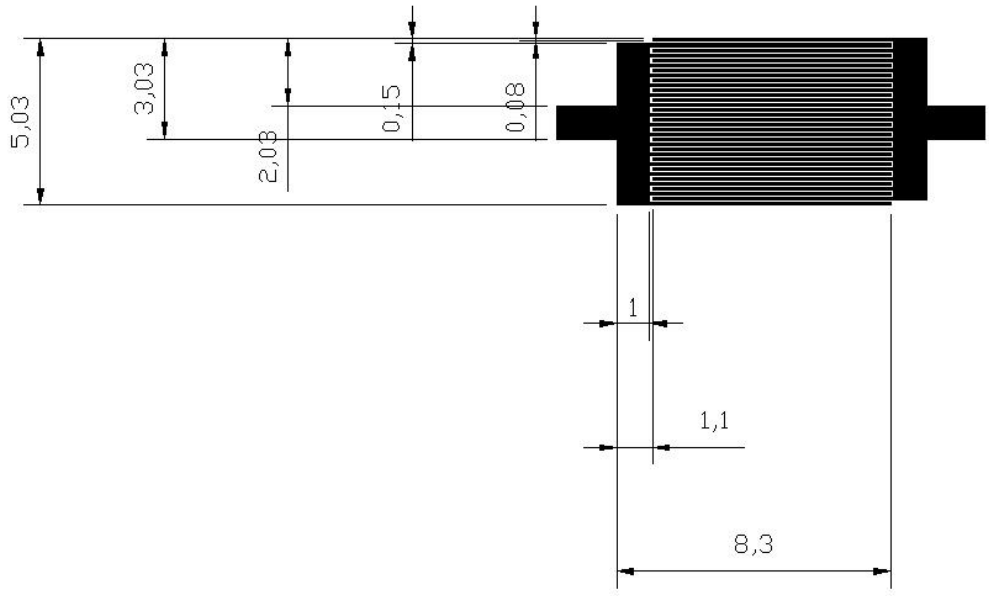

Figure 11.1 Gold Interdigitated Film Design.

Silver soldering pads were printed on both sides of the gold interdigitated array.

An ‘ink’ (or paste) was prepared with better than 99.9% pure ZnO powder (supplied by Sigma Aldrich, catalogue number 20,553-2) and one of several

different oils (that would act as solvents) into a homogeneous paste. Different percentages of binders (substances that would ease the adherence of the ink to the substrate) were added to some of the inks. A simple mixing process by hand to make it homogenous is completed, using a pot and stainless steel tools (see Fig. 11.2).

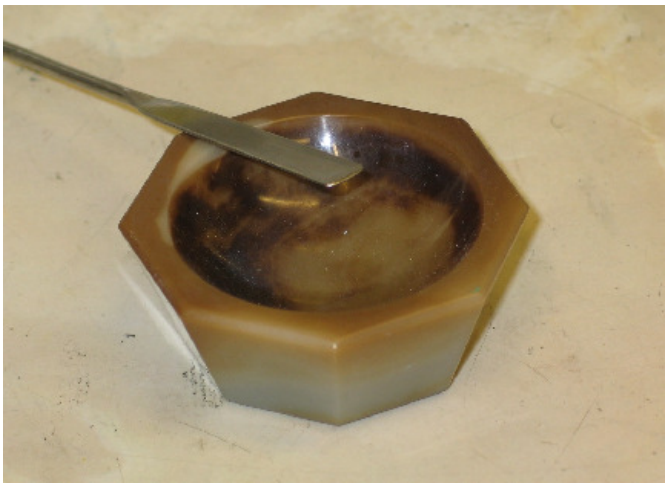

Figure 11.2 Mixing Tools.

The ink was then taken to a mill (see Fig. 11.3) for about five minutes to further reduce particle size and increase homogenization. This mill has rollers that rotate with different angular speeds to provide shear stress to the ink that is constantly going from one roller to the other by the small gaps in between them.

Then the ink is deposited on the substrate by a screen printing process. The sketch in Fig. 11.4 shows a schematic arrangement of the process and the instruments used for it *(Atkinson et al., 1992).*

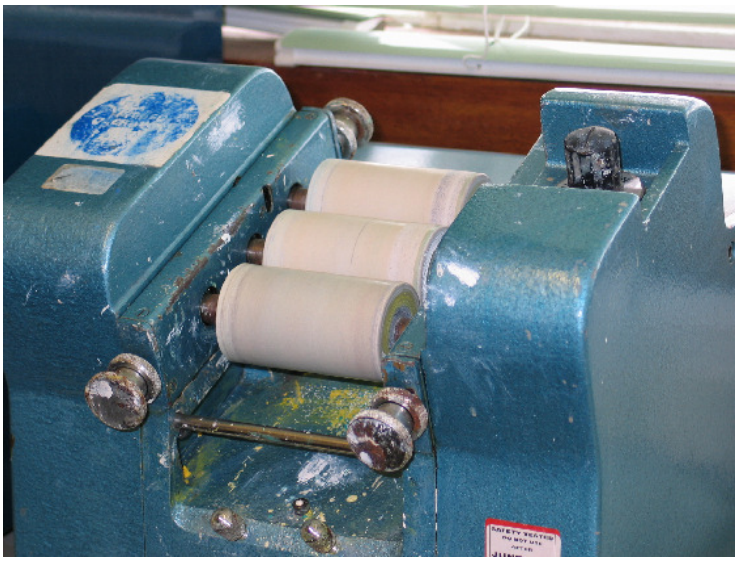

Figure 11.3 Mill used for Homogenization.

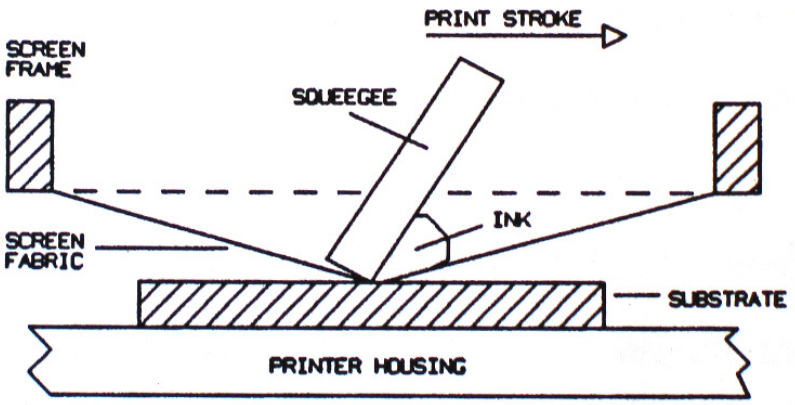

Figure 11.4 Screen Printing Technique.

Quoting Sizeland *(1994):* "The screen is held above the substrate, paste (ink) is applied to the screen and the squeegee travels over the screen, pressing it down into contact with the substrate, pushing the paste through the screen, thus depositing paste onto the substrate surface." A mesh in between the substrate and the screen would allow the deposited ink to have the desired shape. Different ink thicknesses (of the order of several μm) can be achieved: an emulsion is fixed in

the screen that provides the space between the mesh and the substrate where the ink is deposited.

The screen used for the deposition of the ZnO inks was made of a stainless steel mesh at an angle of 45° with the frame, with 325 holes per square inch, and an emulsion about 13 μm thick. The hole density and emulsion thickness are the main drivers that determine final film thickness; other drivers are the viscosity of the ink and the pressure applied on the squeegee.

Once the deposition of the ink was completed, the substrate was taken to a furnace for a carefully planned firing to a temperature of up to 850℃ (standard temperature in the industry) in a process that can take up to an hour, according to the profile showed in Fig. 11.5; it should be noted that the firing for all printings described in this report followed the same temperature profile. In case of a commercial ink like the one of gold used for the interdigitated array or when using a binder, the firing temperature is set by the manufacturer; in case only an oil (solvent) is used, the firing temperature has to ensure this solvent evaporates at the end of the process.

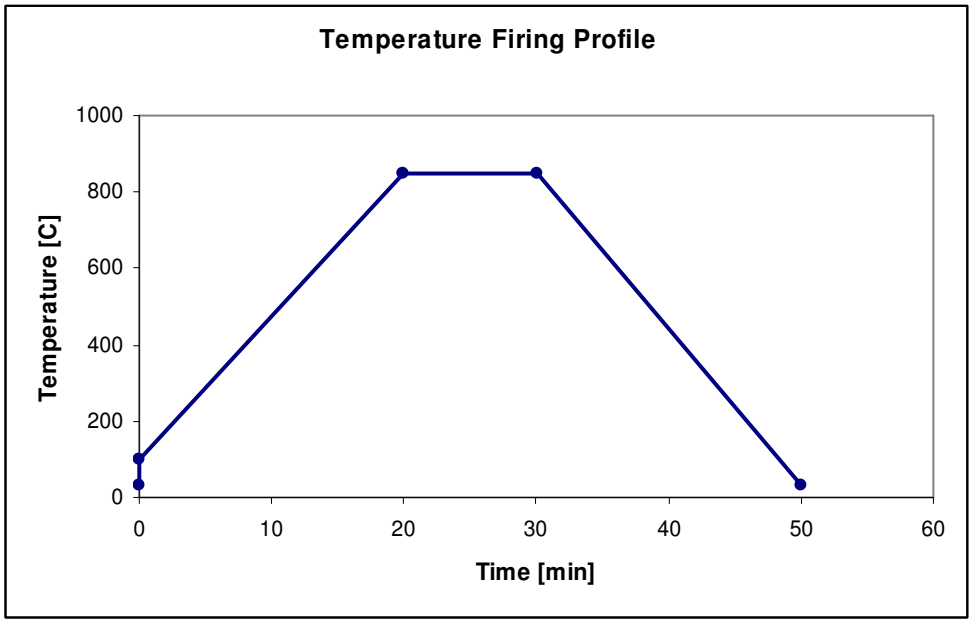

Figure 11.5 Furnace Temperature Sequence.

Shorter times in the firing processes were also tried for the ZnO inks, but the above described firing profile seemed to provide the better adherence of the ink to the substrate.

ZnO inks were printed on the substrates, covering two gold interdigitated arrays, as can be seen in Fig. 11.6.

With the aid of a sharp object, a groove in the ZnO film in between each gold array was created, so as to separate each individual sensor.

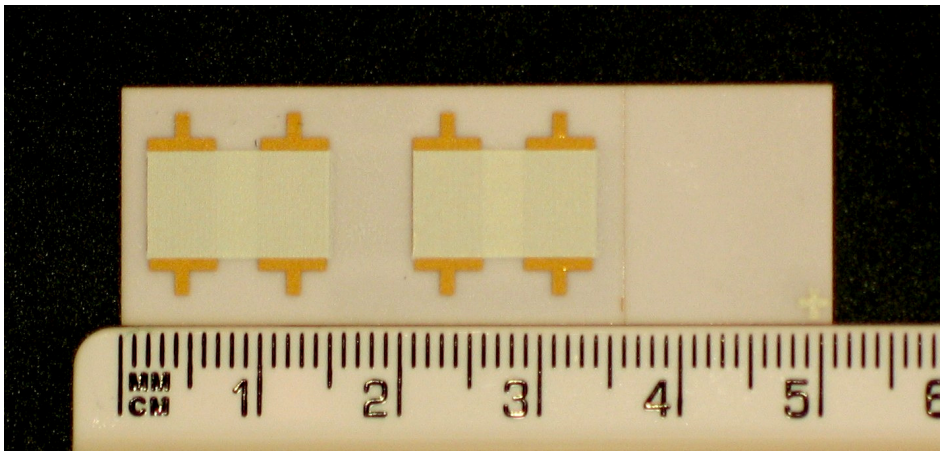

Figure 11.6 ZnO Sensors.

With the screen printing technique, sensors of different thicknesses and multiple layers can be produced. For the first batch of sensors, a single layer with a thickness of about 10 μm (plus or minus 10%) was chosen; this thickness is a common value used in the sensor industry. This thickness has been measured by means of a “light section microscope” that measures the difference in reflection of the impinging light on the substrate and film as an indication of thickness. One of the technical challenges that remain to be dealt with is to achieve little variation among the thickness of different sensors.

The detailed list of steps to manufacture single-layer sensors can be found in Table 11.1. To obtain multiple layers, the last four steps need to be repeated as necessary.

Table 11.1. Manufacturing route for single-layer ZnO thick films.

Step	Operation
1	Screen-print silver contacts for Ruthenium heater
2	Dry at low temperature
3	Fire to temperatures of up to 850℃
4	Screen-print Ruthenium heater
5	Dry at low temperature
6	Fire to temperatures of up to 850℃
7	Screen-print interdigitated gold array
8	Dry at low temperature
9	Fire to temperatures of up to 850℃
10	Optical inspection of gold array
11	Screen-print silver contacts for gold array
12	Dry at low temperature
13	Fire to temperatures of up to 850℃
14	Prepare ZnO ink
15	Mill ink for homogenization
16	Screen-print ZnO ink
17	Dry at low temperature
18	Fire to temperatures of up to 850℃
19	Measure film thickness

After some experience was acquired with the operation of single-layer films, and with the intention of reducing the resistance of the pure ZnO sensors, it was decided to manufacture a final batch of sensors with the same characteristics but made of three layers of the oxide. This result is achieved by subsequent printing and firing individual layers one on top of the other. The thickness achieved on the triple-layer sensors is in the order of 30 µm, that is, about three times the thickness of the single-layer sensors.

Several different inks were tested so as to determine which one provided the best adherence of the sensing material to the substrate; some of them were of pure zinc oxide with an oil (or vehicle), whose only purpose is to act as a solvent of the oxide to facilitate later the screen printing process. The following oils (always in the minimum amount possible) were used:

a-Terpineol (90%): oil produced by Sigma Aldrich (catalogue number 43,262-8)
Rosmerinol: oil produced by Heraeus.

Pine Oil: produced by Heraeus.
ESL400: vehicle produced by ESL Europe.

If a good homogenization is achieved, most if not all of the oil or vehicle should evaporate during the firing process.

Besides trying with different oils and vehicles, other chemicals known as binders where also used. These have the ability to facilitate the adherence of the zinc oxide to the substrate; they should remain with the zinc oxide after firing. The following were tried in the mass percentages indicated in parenthesis:

IP027 (18% and 30%): produced by Heraeus.
PbO (6% and 12%): produced by Aldrich.

On the back of the substrate, a heater made of a resistor material (ruthenium oxide in a glass frit) is deposited so as to allow the heating of the sensor to reach temperatures of up to 80 to 100°C during regeneration. Silver contacts were deposited before the ruthenium. This heater follows the same design used by Osborne *(1999)*, which is depicted in Fig. 11.7.

The production and utilization in conjunction with semiconductor gas sensors of thick film RuO_2 heaters is considered a mature technology. These heaters are reliable and not very much subject to ageing after utilization in temperatures not higher than 300°C. A good review on them can be found in Nowat et al., *(1992)*.

To this heater element, a commercially available thermocouple can be attached by means of Kapton® tape. Thermocouples require their own electrical connections.

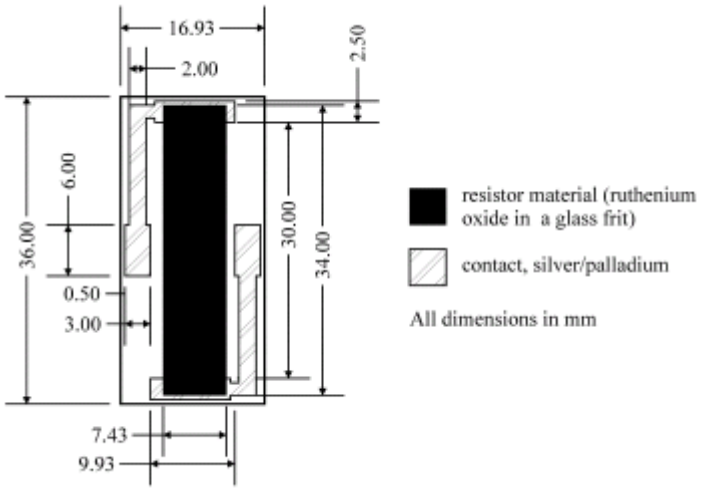

Figure 11.7. Heater Element Design.

12. Characterization of the ZnO Thick Film Sensors

Before testing the ZnO sensors under a flux of AO or other gases, they were studied using several techniques so as to learn more about their physical and chemical characteristics. Several batches of sensors were prepared using the same techniques; Table 12.1 lists all sensors used for this present research, indicating manufacture and place and type of testing.

Table 12.1 Master List of Sensors

Serial Number	Type	Date of Manufacture	Test Location and Conditions
100	1	October 2004	ATOX (exposed to AO)
101	1		
102	1		ATOX (covered with quartz window)
110	1		ATOX (exposed to AO)
111	1		
112	1		ATOX (covered with alumina)
122	1		Univ. of Southampton (SEM and basic electric response)
124	1		
200	2		ATOX (covered with quartz window)
201	2		ATOX (exposed to AO)
202	2		ATOX (covered with alumina)
203	2		Univ. of Southampton (SEM and basic electric response)
204	2		
301	3		Univ. of Southampton (SEM and basic electric response)
302	3		
401	1		ATOX (exposed to AO)
402	1		
403	1		
404	1		ATOX (covered with quartz window)
405	1		
406	1		ATOX (covered with alumina)
407	1		
A1	1	October 2006	University of Southampton (for vacuum and atmospheric gases) and ATOX (for atomic oxygen)
A2	1		
A3	1		
B1	1		
B2	1		
B3	1		
C1	1		University of Southampton (for vacuum and atmospheric gases)
C2	1		
C3	1		

Unless otherwise stated, the following results apply equally to sensors of all batches and refer to tests conducted within few days or weeks of the manufacturing of the respective sensors.

12.1 Adherence to Substrate

Initially, the different sensors produced were subjected to simple mechanical tests to evaluate the adherence of the thick film to the substrate. For all but the four following sensor types it was possible to scratch the zinc oxide by applying a gentle pressure with a sharp object:

- Type 1: Pure ZnO dissolved in ESL400 prior to firing, single layer.
- Type 2: ZnO (82%) with IP027 (18%).
- Type 3: ZnO (70%) with IP027 (30%).

It should be noted, that when an adhesive tape was applied to the above mentioned sensor types, in all but the Type 3, some sensor material remained on the tape when it was removed from the sensor.

It was decided to continue testing with these three types of sensors only from now on, since the adherence to the substrate was best. It should be noted, however, that the adherence of these sensors is inferior to that achieved by thin film sputtering as used in the sensors produced by Osborne *(1999).* The limited adherence of ink to the substrate may limit the application of these sensors to circumstances where damage due to installation, transport, and operation are not likely to occur.

12.2 Response to changes in Temperature and Pressure

The purpose of this package of work was to determine the response of Type 1 sensors to changes in pressure and temperature. These tests were carried out in a custom built chamber at the astronautics laboratories of the University of Southampton. The chamber (see Figure 12.1) was equipped with a mechanical pump and a turbomolecular pump (Edwards catalogue EXT 70 DN63 ISO-K). A

system to continuously monitor pressure from atmospheric pressure down to 10^{-9} Pa was installed and controlled by a PC. The resistance readings were carried out by highly accurate Agilent Data Acquisition Unit (model 34970A) that was connected to a PC for remote operation and data recording. This chamber has no windows.

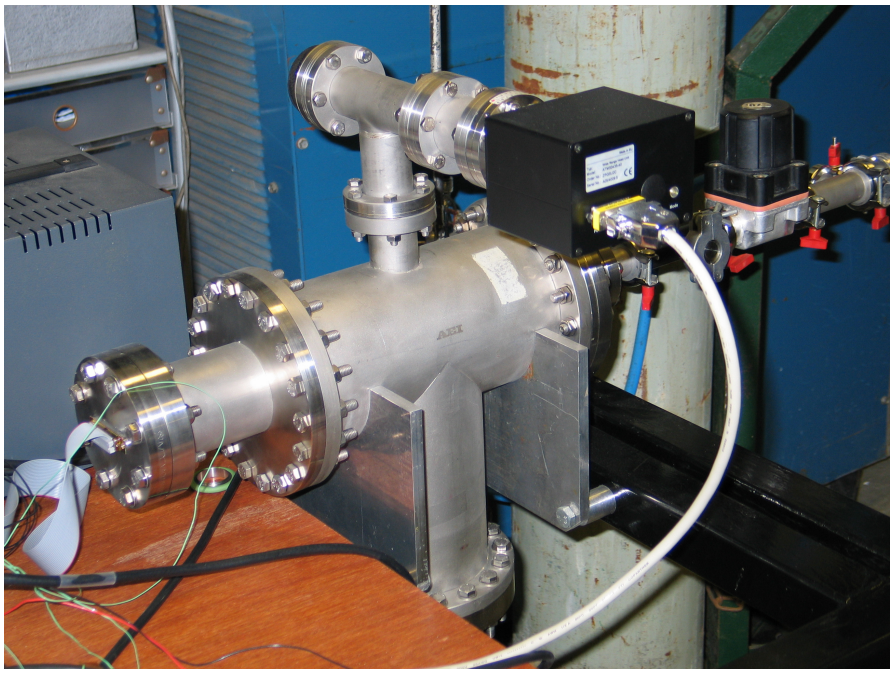

Figure 12.1. Custom-built vacuum chamber for this research project.

DC resistance was chosen as an indicator of sensor response since, as discussed in Chapter 10, it is expected that a reduction in atmospheric pressure will result in desorption of molecular oxygen and water, which in turn should reduce the resistance of the sensors. Some preliminary tests were carried out in vacuum; these determined that for temperatures close to ambient, the most stable temperature for resistance readings over time was 35℃.

Figure 12.2 shows the typical response of Type 1 sensors when pressure is reduced. The first significant drop in resistance (at time 190 hours) occurred when the mechanical pump was activated. The second drop occurred when the turbomolecular pump was activated (at time 330 hours). The temperature used for this test was around 35℃. The final pressure in the chamber was in the order of

10^{-4} Pa. From the time the turbomolecular pump was activated, it took the sensors at least 72 hours to provide a nearly stable resistance. The resistance drop from atmospheric pressure to high vacuum was of about five orders of magnitude; this is general agreement with past experience presented in Section 10.7.

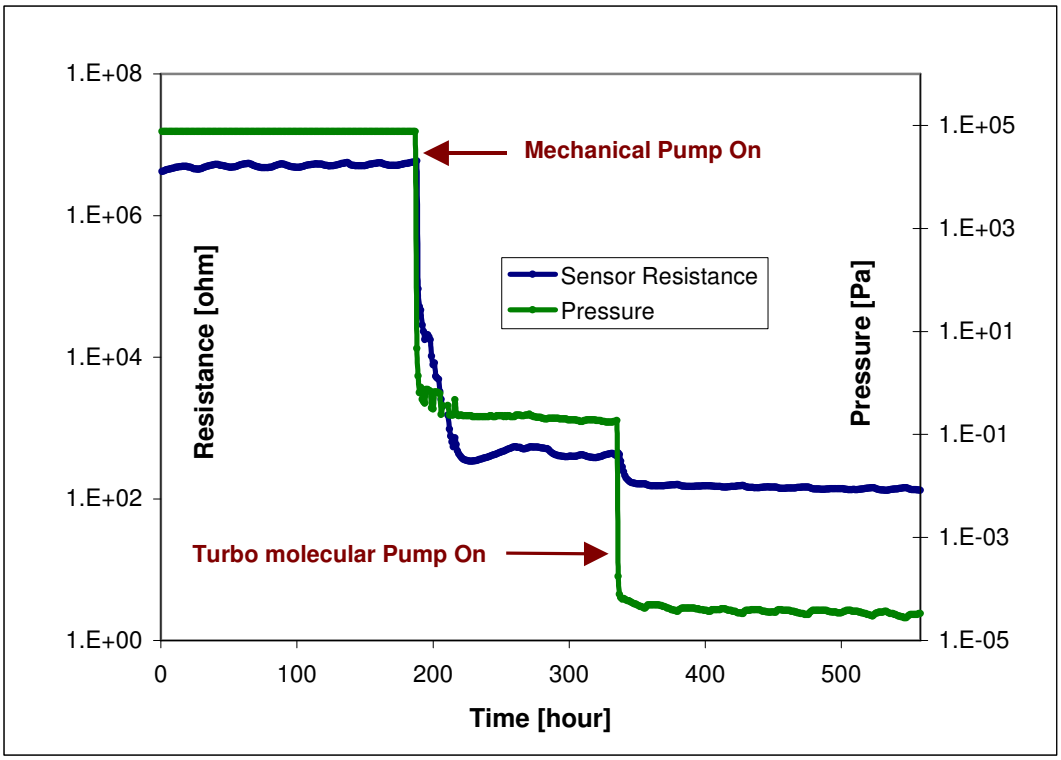

Figure 12.2. Change in Resistance with Change in Pressure for one Type 1 Sensor (serial number C2).

Once the resistance readings of all sensors were stable, temperature was varied according to Figure 12.3. This figure shows that as temperature increases, resistance decreases; this is to be expected, since as more thermal energy is available, more electrons are able to migrate into the conduction band and therefore conductance increases.

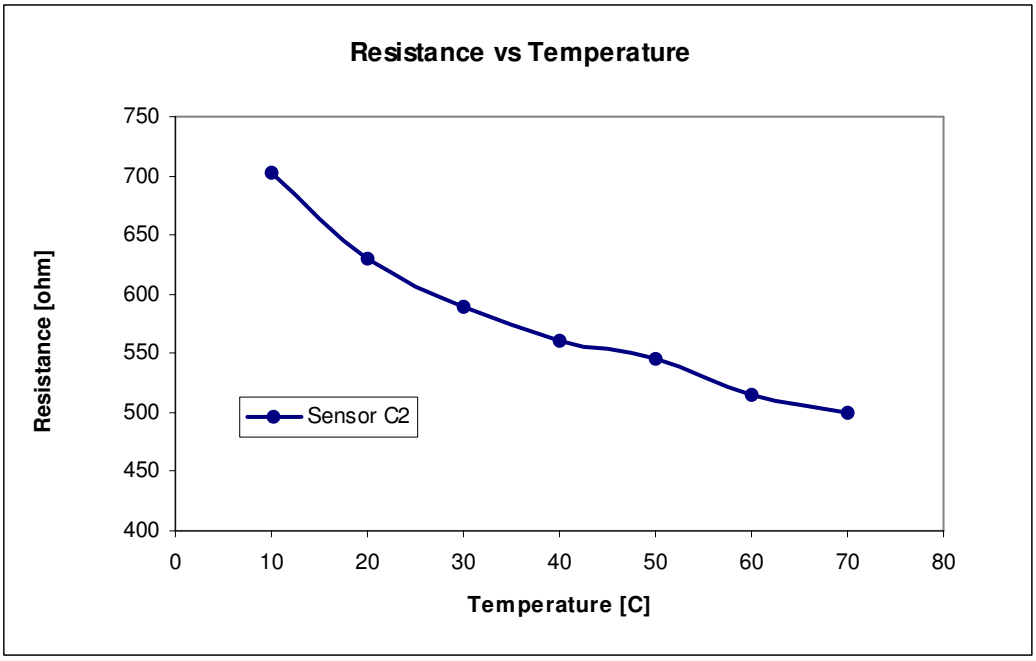

Figure 12.3. Resistance versus Temperature for a Type 1 sensor.

Using equation 12.1 *(Wortman et. al., 1972):*

$$R = R_0 \exp(\frac{E_R}{kT}) \tag{12.1}$$

we can find the following relationship (Equation 12.2):

$$\ln(R) = \ln(R_0) + \frac{E_R}{kT} \tag{12.2}$$

The same data presented in Figure 12.3 is now presented in Figure 12.4 but using Equation 12.2. The slope of the linear regression curve fitted into the data allows us to find the activation energy E_R which is 0.045 eV, with coefficient of correlation 97%. This value is similar to that found by Wortman et. al. *(1972)* for thin ZnO films (0.047eV) and similar to that found by Osborne *(1999)* for thin films as well (0.039). These range of values are the ones to expected for the first ionization energy for interstitial zinc atoms in Zinc Oxide. These results allow us to confirm that O_2 will adsorb as O_2^- removing some of the electronic density available for conduction in the ZnO.

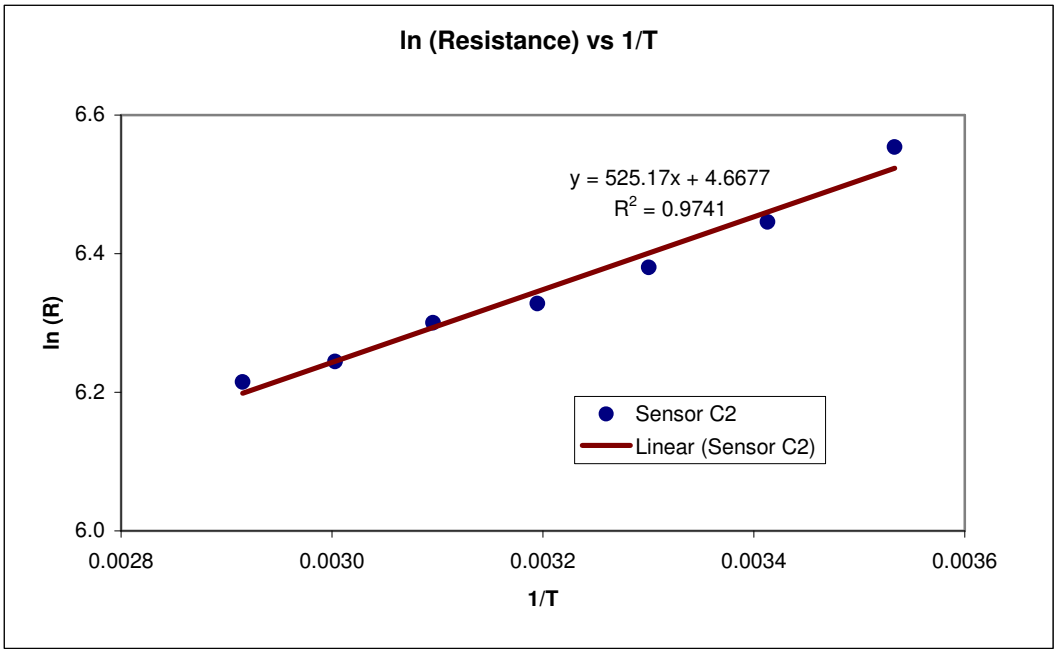

Figure 12.4. Logarithm of Resistance versus the Inverse of Temperature for a Type 1 sensor (serial number C2).

It was also found that although the all Type 1 sensors were manufactured according to the same procedures, and all have the same exposed surface, their baseline resistance in vacuum can vary significantly from sensor to sensor. Table 12.1 gives an indication of the distribution of baseline resistances for one batch tested.

Table 12.2. Mean Baseline Resistance for one batch of Type 1 Sensors at 35°C

Mean Resistance [Ω]	Standard Deviation [Ω]
96	50

12.3 Electrical Response Characterization

With the purpose to determine the response of Type 1 and 2 single-layer sensors due to varying applied DC voltages, a series of tests were carried out under vacuum conditions using a Keithley 6485 multimeter. These tests took place nine months after the sensors were manufactured; the sensors were stored in a

clean box under normal atmospheric conditions during this time. The vacuum chamber used was that depicted in Figure 12.5 at the Astronautics Research Laboratories of the University of Southampton. No light was admitted into the chamber during testing, which occurred at atmospheric pressure. Plots of resistance vs. voltage can be found in Figures 12.6 and 12.7 for typical results; the voltage was varied from nearly 1 to 50 V, and then back to 1 V.

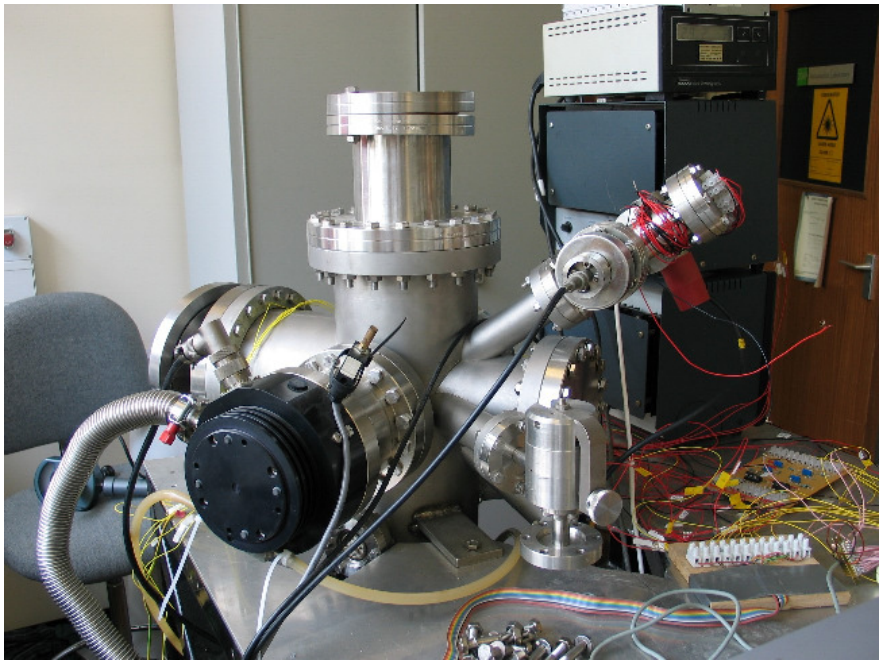

Figure 12.5. Vacuum Chamber at the University of Southampton.

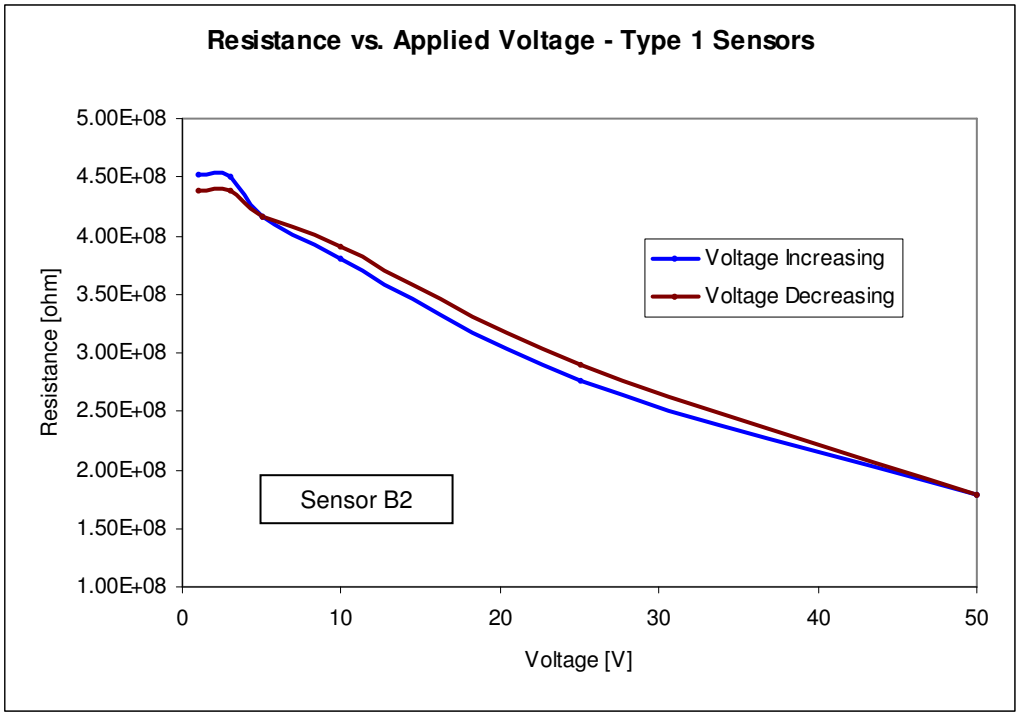

Figure 12. 6. Resistance vs. Voltage for Type 1 Sensor.

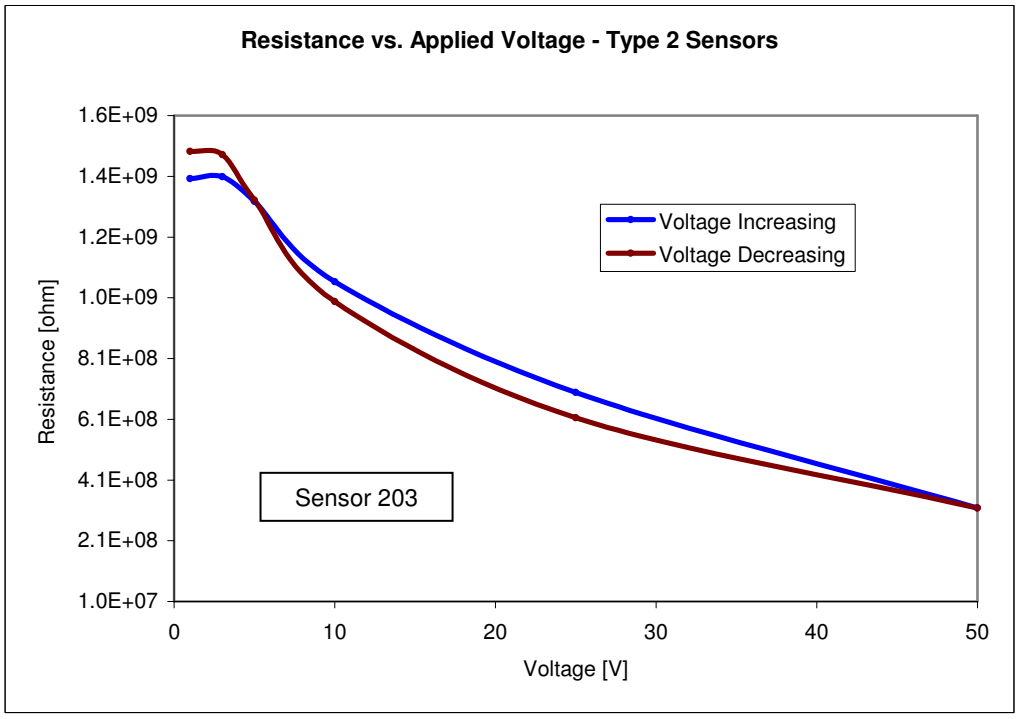

Figure 12.7 Resistance vs. Voltage for Type 2 Sensor.

The above results show that for sensors of types 1 and 2, the resistance decreases with an increased voltage across the sensor, showing a clear departure from an ohmic response for voltages in excess of 3.3 V, which has been determined to be the breakdown voltage for Type 1 and Type 2 sensors. This is in agreement with published values of around 3 V for ZnO varistors *(Ohashi et al, 2003).* The results also show that resistance can drop up to an order of magnitude when the voltage increases from 5 V to 50 V.

There is a modest hysterisis on the resistance value of the sensors. The resistance values first obtained when increasing the voltage are generally lower than those obtained later when a decreasing voltage is applied for Type 1 sensors. The opposite is true for Type 2 sensors.

To further characterize the region near the breakdown voltage but at a low pressure, Type 1 sensors were tested in the ATOX chamber (this chamber to be described later in Chapter 13) at a pressure of about $1.3*10^{-2}$ Pa and temperature of 35℃, after four days of heating at about 135℃. The instrument used was an Impedance Spectroscopy equipment to be described in more detail in Chapter XIV. The results for one sensor, which are typical for Type 1 sensors, are shown in Figure 12.8 and confirm that in the range 0 to 3.3 V, Type 1 sensors obey Ohm's Law (evident by linear response of current vs. applied voltage as shown in Figure 12.8)

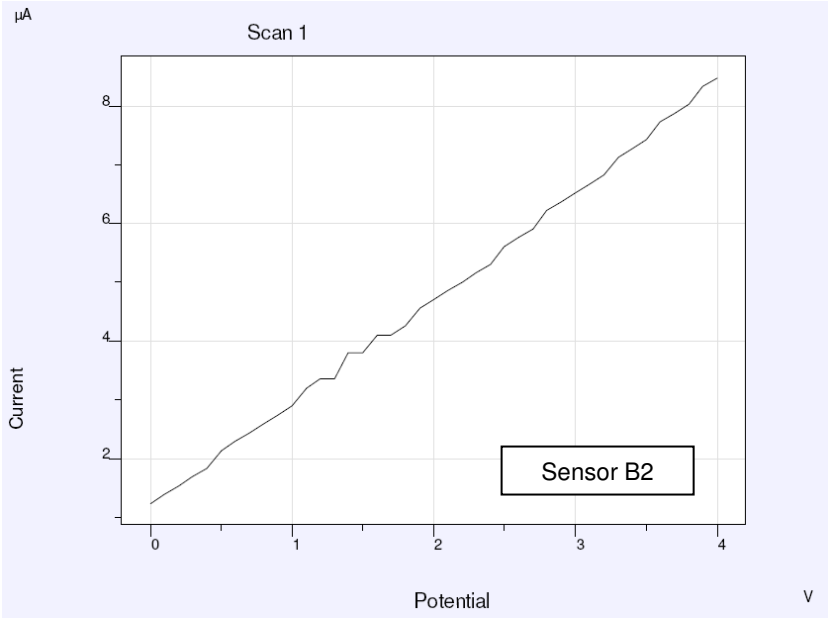

Figure 12.8 Typical resistance response for Type 1 sensors.

12.4 Characterization by Electronic Microscopy

Thick film ZnO Type 1, 2 and 3 sensors were examined by means of Scanning Electronic Microscopy (SEM) and Energy Dispersive X-ray Spectroscopy (EDS) at the University of Southampton. The purpose was to determine grain characterization and chemical composition before AO exposure.

The instrument used for these tests was a JSM 6500F thermal field emission scanning electron microscope (see Fig. 12.9). Its main characteristics are: accelerating voltage 0.5 to 30 kV; magnification up to 500,000; resolution: 1.5 nm at 15 kV, 5.0 nm at 1 kV; it allows secondary electron and backscattered electron imaging, electron backscattered diffraction, and energy dispersive X-ray determinations (by means of the attached Oxford Inca 300 instrumentation).

Figure 12.9 JSM 6500F thermal field emission scanning electron microscope.

Each of the tested substrates was attached to the sample holder by a special adhesive conductive tape (see Fig. 12.10). So as to provide electric continuity between the top surface of the sample holder and the sensors to be

tested, a conductive strip was placed to connect that surface with the film connectors on one side of the substrate.

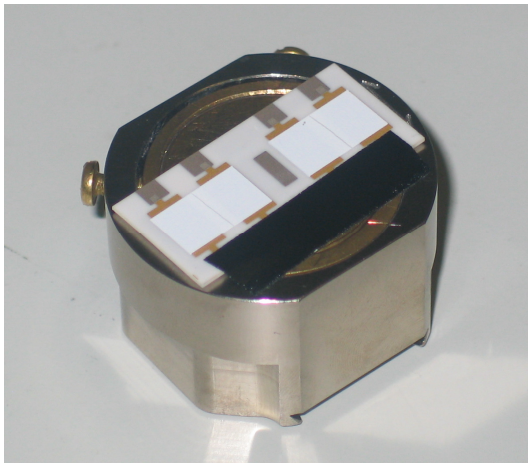

Figure 12.10. Substrate in Sample Holder.

12.4.1 Type 1 Sensors

Type 1 sensors not yet exposed to AO generally showed a flat surface, but often, deep cracks and protuberances were noticed (see Fig. 12.11). Depending on the depth and extension of the cracks, they can have a severe impact on the ability of the sensor to conduct electrons.

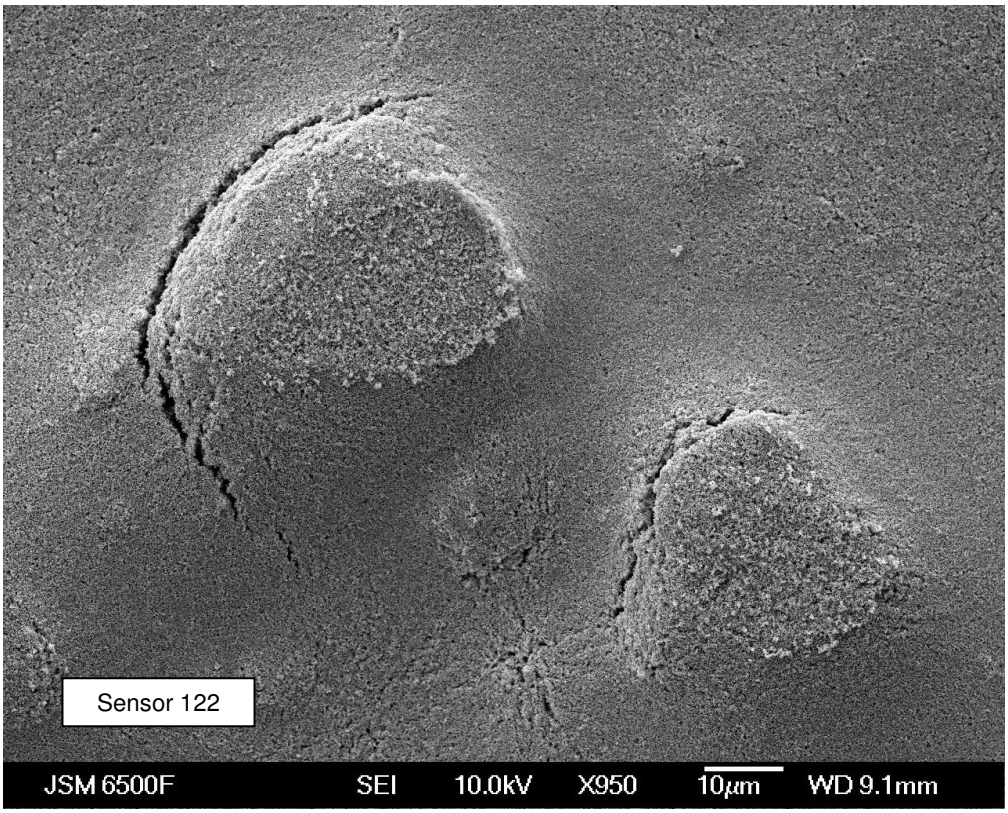

Figure 12.11. Typical Type 1 Sensor SEM Image.

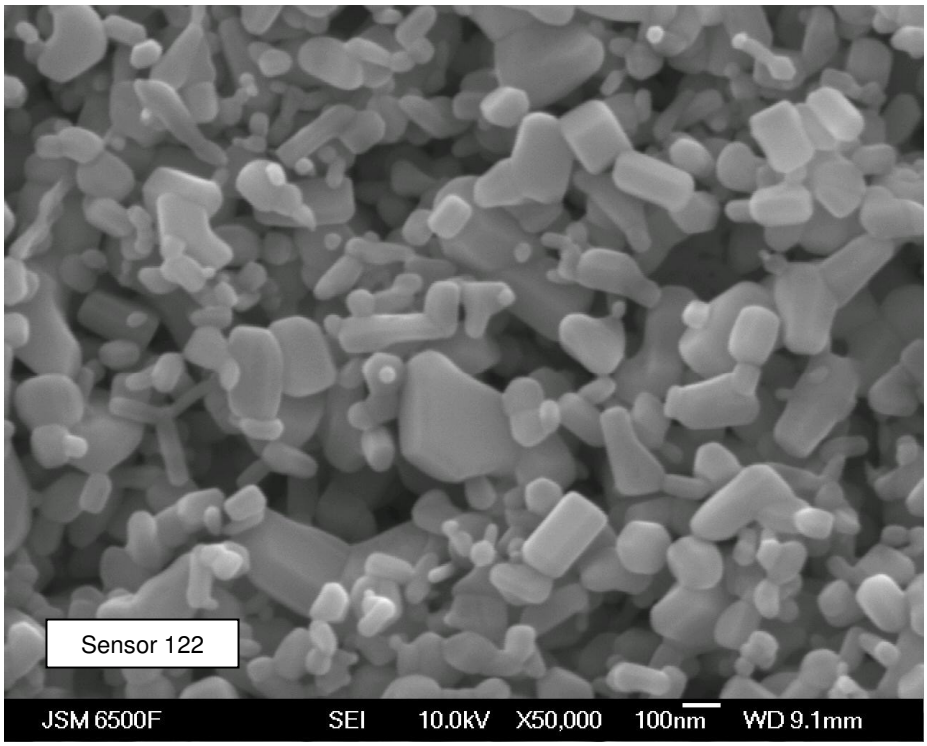

Figure 12.12. Typical Type 1 Sensor SEM Image.

Visual inspection of several SEM pictures taken at different magnifications, show that crystallite size for Type 1 sensor range from 20nm to 1000nm (see Fig. 12.12). It can also been seen the porous nature of this type of sensors; although the area exposed to the ram remains the same as the geometrical surface, the actual surface exposed to gases (the effective surface) that can diffuse through the spaces in between the crystallites (like air and O_2 at standard atmospheric conditions) is much bigger than the geometrical surface of the sensor.

Using equations 10.6 and 10.7 to find the diffusion time along a distance of 20nm (the size of the smallest crystallite), a D^0 of $1.63*10^{11}$ $cm^2.s^{-1}$ *(Newmann, 1981),* and an activation energy of 4.11 eV, we find that diffusion time is in the order of 10^{44} s for a temperature of 308 K. For the time scale of the experiments being carried out in this research, AO diffusion within the crystalline is not to be considered a significant factor in resistance change.

EDS analysis performed on the Type 1 sensors, revealed they all contain the same relative proportions of the elements Zn and O, consistent with the stoichiometry of ZnO (Fig. 12.13 presents results in terms of atomic percentage). Information provided by this instrument does not allow us to elaborate on composition at the chemical compound's level. The maximum percentage error for this instrumentation is +/- 0.5%.

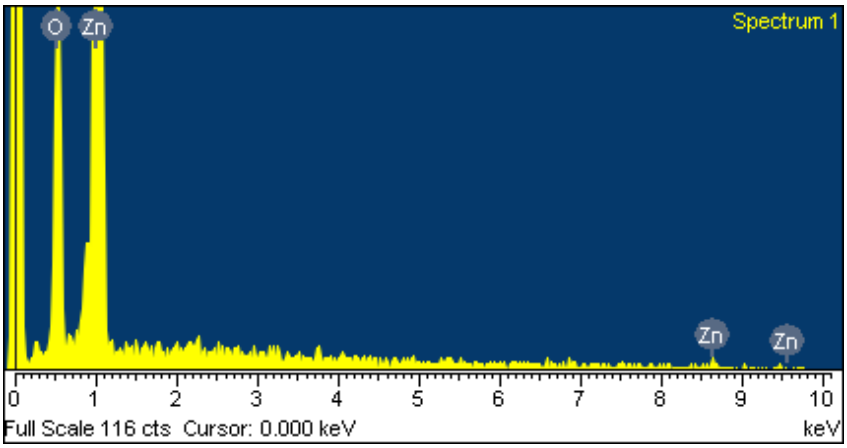

Figure 12.13. Results for Sensor 124: O (52.4%), Zn (47.6%).

It should be noted that EDS is an analytical tool for surfaces. The volume sampled (that is, the actual portion of the specimen under analysis) is a layer with a thickness of about 1µm *(Goodhew et al., 2000).*

Pure ZnO powder, from the same source employed to manufacture all the sensors, was also analyzed by means of the SEM and EDS instrumentation. Fig. 12.14 shows a microphotograph of the powder, which reveals crystallites of about the same size of those in the films (compare with Fig. 12.12). These results lead us to believe that the homogenization carried out in the three-roller mill does not significantly alter the size of the crystallites.

Figure 12.15 presents the composition for the ZnO powder in terms of atomic percentage. A comparison with Fig. 12.13 reveals a decrease in the ratio of the concentrations of O to Zn (ratio of areas under the curves as calculated by the instrument) in the printed ZnO versus the powder; it is possible to speculate that this reduction is due to the firing sequence during sensor production. This relative increase in Zn atoms can increase the concentration of interstitial Zn atoms that provide most of the charge carriers available for conduction.

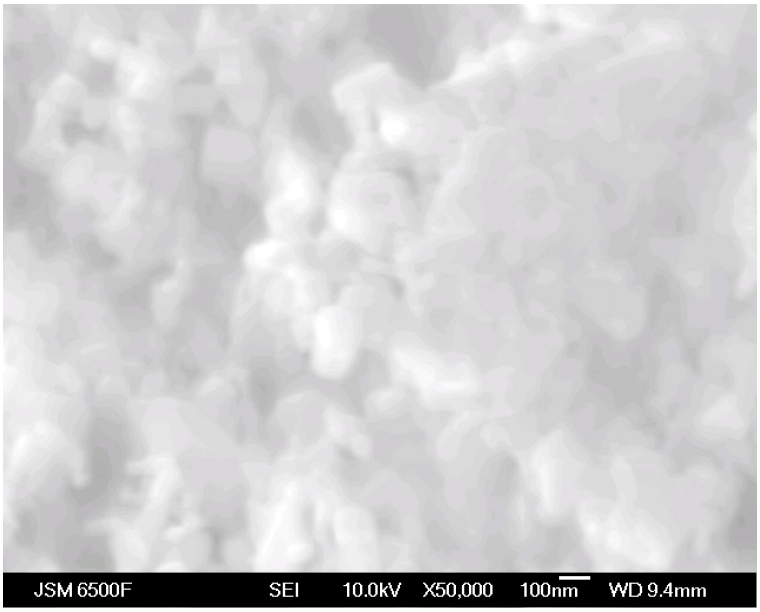

Figure 12.14. ZnO powder.

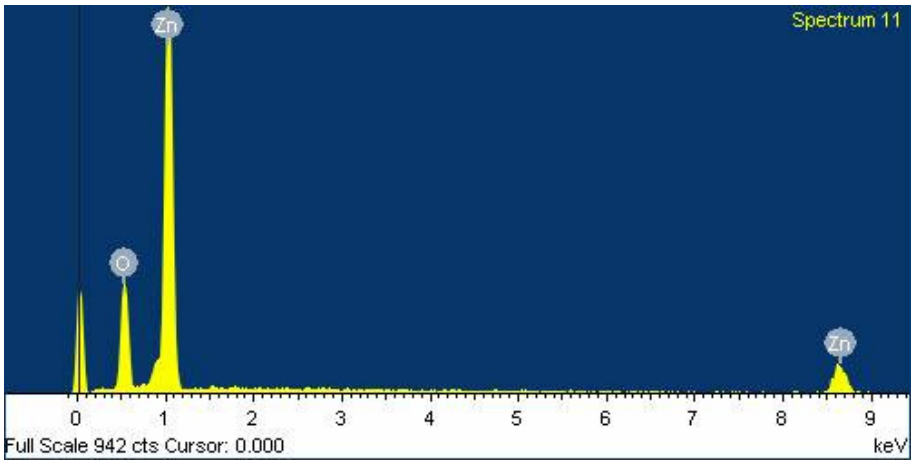

Figure 12.15. Results for ZnO Powder: O (56.8%), Zn (43.2%).

12.4.2 Types 2 and 3 Sensors

Sensors of Types 2 and 3 generally show a flat surface (see Figures 12.16 and 12.17), but holes and other features are also present. SEM pictures at higher magnification show the binder keeping crystallites together in the sensor (see Figure 12.18); this figure also shows crystallite sizes comparable to that of Type 1 sensors.

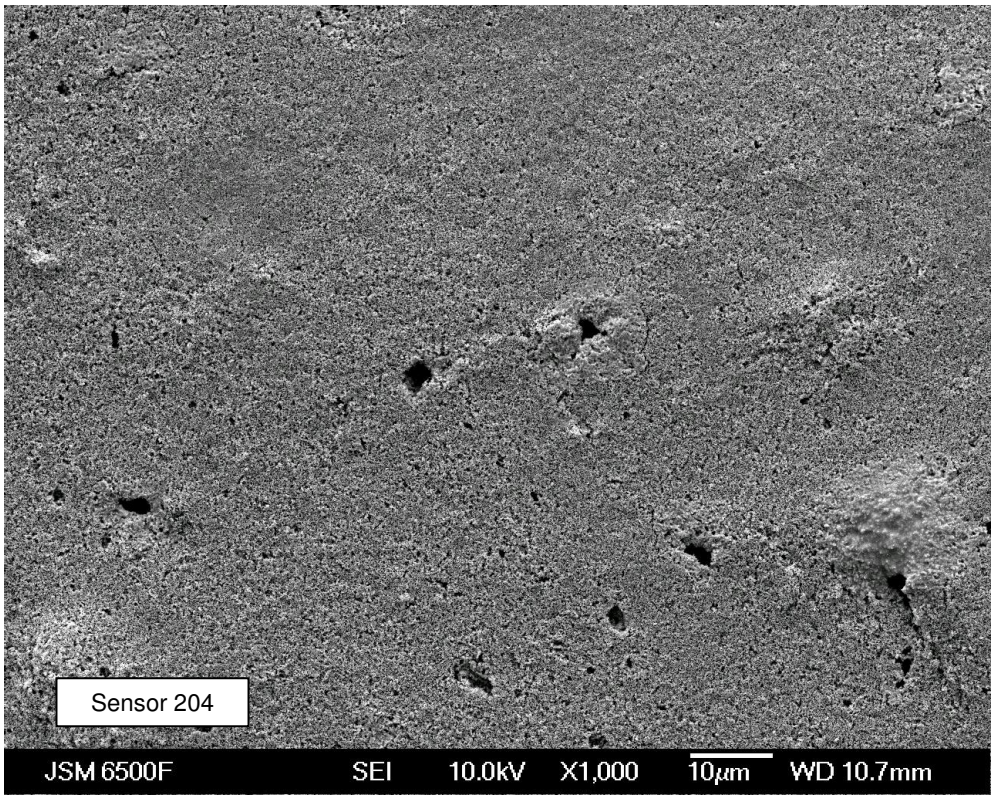

Figure 12.16. Type 2 Sensor.

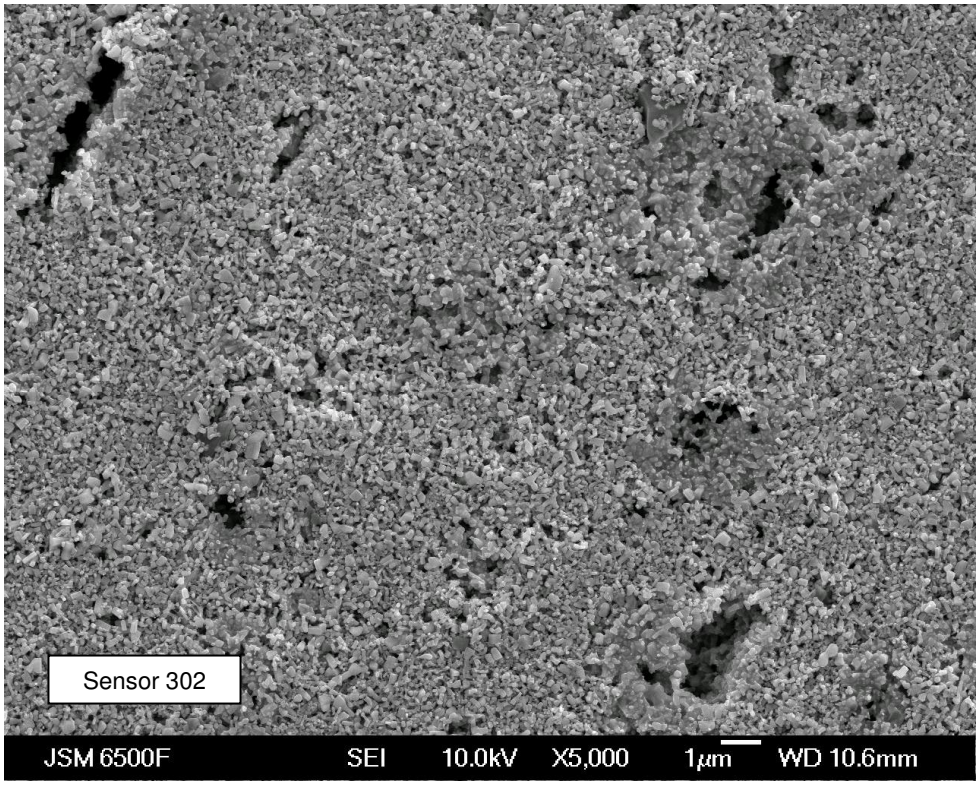

Figure 12.17. Type 3 Sensor.

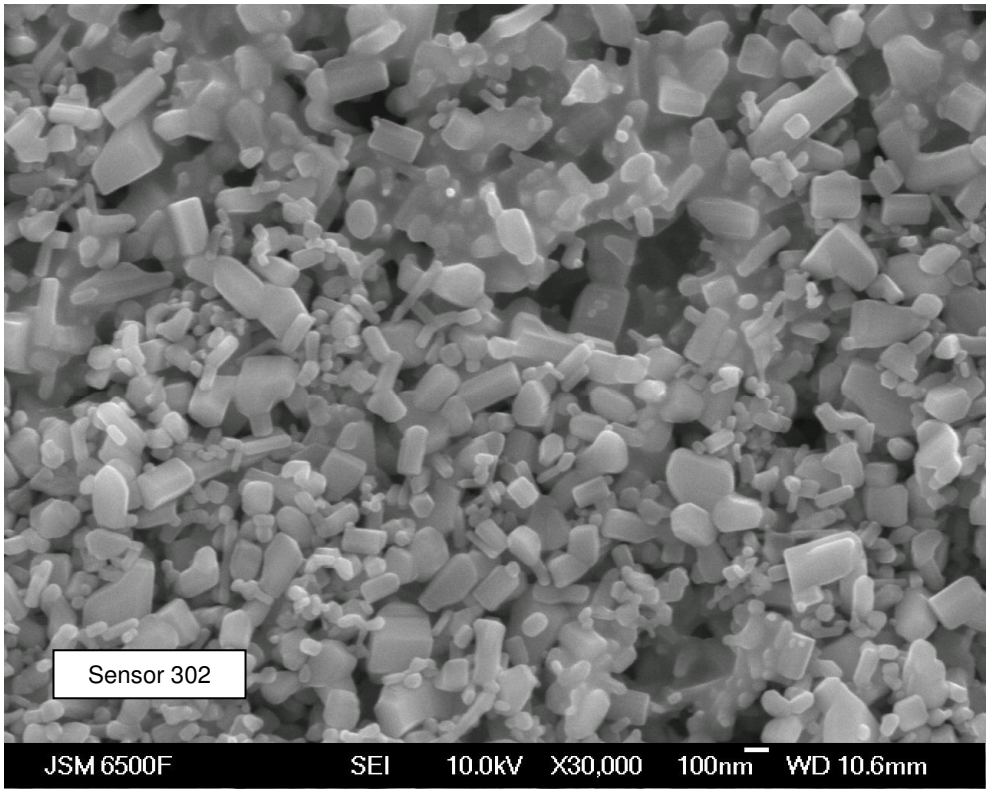

Figure 12.18. Type 3 Sensor.

A ‘sensor’ manufactured with an ink made exclusively with the binder used in type 2 and 3 sensors was also tested with the EDS instrumentation. Table 12.2 presents the results of such chemical analysis.

Table 12.3 Ink Chemical Analysis

Element	Atomic %
O	73
Si	12
Pb	14

12.5 Summary

The tests outlined in this chapter have show the sensors to have a ohmic response up to applied voltages of 3.3 V. Their chemical composition of pure ZnO sensors is nearly stoichiometric. Sensors reduce their DC resistance by about five orders of magnitude when pressure is reduced from atmospheric to about 10^{-4} Pa. Resistance also reduces with increase in temperature; activation energies for the first ionization of interstitial zinc oxide have been measured and found to be in agreement with published literature. Sensors show a limited adherence to substrate, as well as some cracks and valleys in their surface; crystallites have been found to be in the nano-size range.

13. Sensor Characterization Investigation using DC Resistance

The main objectives of these experiments were to characterize the DC response of Types 1 and 2 sensors to atmospheric gases and to AO at LEO-like fluxes.

13.1 Response to Atmospheric Gases

The objective of this package of work was to determine the response of Type 1 sensors to the atmospheric gases in both dry and wet conditions. Although the sensors developed under this research are intended to be operated under the vacuum conditions prevalent in LEO, the sensors will be exposed to Earth's atmosphere before and after this happens, so their response to these gases is required to be characterized to understand any possible interactions. The chamber used and other required equipment are those described in Section 12.2. The sensors were kept for at least 72 hours in vacuum before different gases were allowed into the testing chamber; the sensor temperature was 35°C. Gas bottles were used to provide the dry O_2 and N_2 for this work. Gases were admitted into the chamber in the order shown in Figure 13.1; vacuum was obtained and kept for at least 72 hours in between each gas exposure; values shown in Figure 13.1 for final values, after a stable response was present for several hours. The pressure of each gas tested was one atmosphere inside the chamber; the N_2 was saturated with water by means of the device shown in Figure 13.2.

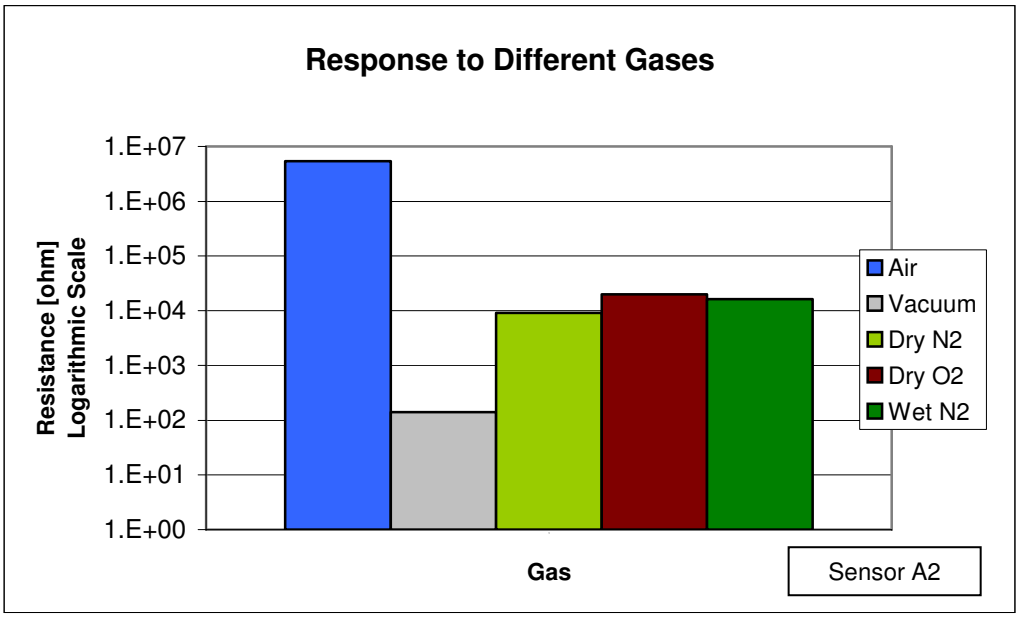

Figure 13.1. Typical Response to Different Gases of Type 1 Sensors.

Figure 13.2. Device to Saturate with N_2 with H_2O.

As observed before, there is a significant drop in resistance in going from atmospheric conditions to high vacuum (10^{-4} Pa). When dry O_2 is admitted into the

chamber, the resistance increases by about two orders of magnitude, as expected, since O_2 will adsorb at the surface of the sensor as O_2^- and therefore, removing some electronic density from the conduction band (see Section 10.4). Molecular Nitrogen also increases the resistance of the sensors, but not as much as O_2, N_2 having a complete electronic configuration in its outer shell; the increase in resistance is attributed to some adsorption and perhaps a piezoelectric effect (not confirmed). Comparison of resistance change between dry and wet N_2 (the former being higher than the latter) indicates the adsorption of H_20 with the removal of some of the electronic density from the conduction band (see Section 10.8).

13.2 Response to Atomic Oxygen

The purposes of these experiments were to characterize the DC resistance response of sensors of Types 1 and 2 to a flux of AO similar to these in Low Earth Orbit, the time dependence of this response, as well as to explore the regeneration properties of these types of sensors. An objective was also to evaluate how the sensors respond to UV radiation. The very high resistance of Type 3 sensors made it impracticable to include these sensors in this testing.

The ATOX test facility in ESTEC, Netherlands, was used for these experiments, which took two separate visits, the first one in August 2004, and the second in September 2005. This facility was chosen because: it can produce a high flux (typically a day-in-orbit fluence in a few hours), the absence of other than oxygen elements, and the fact that it was readily available as part of the support of the European Space Agency for this research. A good description of it can be found in Osborne *(1999).*

13.2.1 Instrumentation

The ATOX source (see Figure 13.2) is of the laser-breakdown type, based on the research work of Caledonia et al. *(1987).* By means of an electromagnetic valve, a measured amount of molecular oxygen is injected in the nozzle of the source. Here, a beam produced by a carbon dioxide laser breaks down the oxygen molecules so as to produce plasma with a temperature in excess of 21000K. This plasma constitutes a source of UV radiation that will reach the test samples, with

an illumination several orders of magnitude higher than the solar at LEO (*Weihs and van Eesbeek, 1994*).

The system is designed so as to allow the plasma (which has been accelerated due to the blast-wave originated during the breakdown) to cool off to the point of allowing the recombination of ions and electrons, but to prevent the recombination of atomic into molecular oxygen. The flux of AO will then reach the sample holder in the test chamber of this instrument.

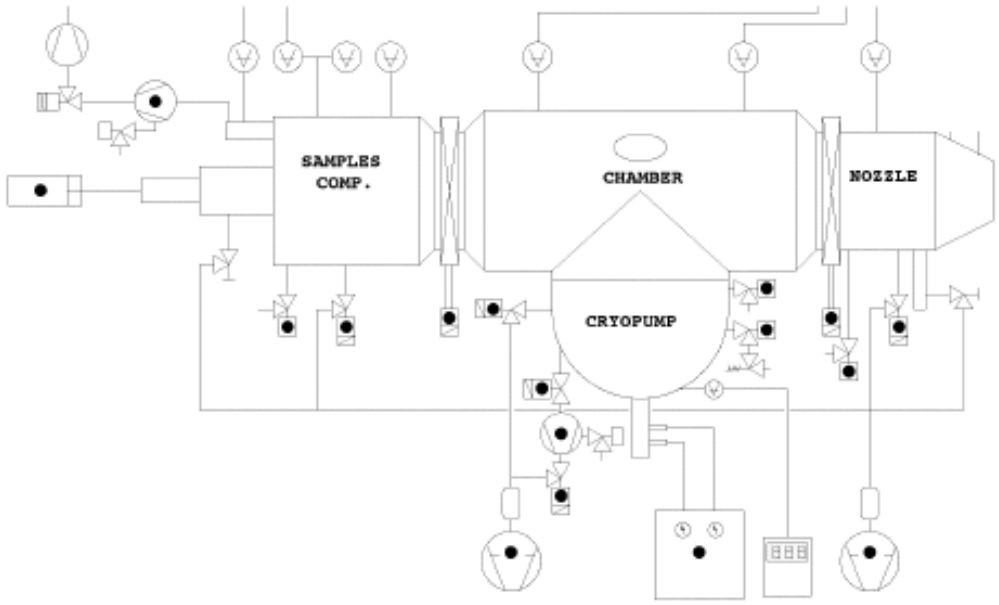

Figure 13.3. ATOX (Osborne, 1999).

It needs to be mentioned that there is a small amount of molecular oxygen that is not dissociated *(Caledonia, 1988),* and other small amounts of excited or ionized AO *(Caledonia et al., 1994)* that would reach the samples under being tested. All these constitute contaminants that should not be ignored.

The AO produced by ATOX has a typical speed of 5 eV, which is the value ram spacecraft surfaces typically experience in LEO, with high directionality. This makes us conclude that the vast majority of AO from the source will interact with the ram surface of the sensors, that is, some of the AO will penetrate into the bulk

of the sensors through the cracks. Due to scattering, the effective area may be higher than the ram area of the sensors.

The test chamber can be kept in a vacuum of 10^{-7} Pa by means of a turbomolecular and a cryogenic pumps, when there is no AO flux. This value will increase to 10^{-4} Pa when the source is generating AO due to the pressure of this element.

The test chamber is connected to a sample chamber that can be isolated from the former. This allows working on the samples and/or replacing them while keeping the test chamber under vacuum. The sample chamber is brought into vacuum by means of a turbomolecular pump, reaching a minimum pressure of 10^{-5} Pa. There are no windows in any of the ATOX chambers.

The sample tray can be moved back and forth from the sample chamber and the test chamber. Its orientation in respect to the flux can be varied so as to allow different angles of impact of the AO upon the samples. The distance between the origin of the flux and the sample tray can also be varied to allow different fluxes to reach it, taking advantage of the geometry of the AO beam.

All the sensors, heaters, and temperature sensors were connected to the internal electrical connections in the ATOX test chamber, thus making those connections available to the exterior of the chamber via the corresponding feedthrough. All leads were soldered using PTFE insulated wire, and vacuum-compatible soldering.

The equipment used to measure the resistance across the sensors was a Hewlett Packard 34401A Multimeter. This instrument was connected to a switch box that allowed the sequential reading of resistance values, with an interval of about 30 seconds for taking readings on the same sensor (which would mean that very rapid changes in resistance on the sensors would not be recorded). This instrumentation was connected to a personal computer that recorded the measured values in a *Microsoft Excel* file.

The multimeter used to measure resistance did so by applying a potential difference across the sensors that varied as a function of the resistance being measured. Table 13.1 (obtained from the manufacturer of the multimeter) indicates

the ranges of resistances, and the corresponding currents, that the instrument can measure; voltages values have been calculated and added by the author. The results of Table 13.1 are very important, since it has previously been determined that the sensors obey ohm's law for applied voltages of less than 3.3 V. Therefore, the most accurate measurements of resistance will take place for resistances of 10^6 Ω or less.

The heaters of the substrates used during each test were connected in series with a power source to heat the films. The voltage applied to the whole circuit was three times as much as intended for each sensor, since they were in series. Given the fact that the resistance value of the heaters was 400 Ω plus or minus 2%, the voltage applied to each particular sensor is very close to one third of the total potential difference applied to the three heaters in series. For heat treatment and regeneration, the potential applied to each heater was about 30 V (which yielded a temperature of about 135°C) and this took place in the sample chamber, while a value of about 5 V (which yielded a temperature of about 35°C) was used in all other circumstances. The temperature for regeneration is in the higher end of the regeneration temperatures chosen by Osborne *(1999)* for this work with thin films.

Table 13.1

Resistance [Ω]	Current [A]	Voltage [V]
1.E+02	1.E-03	0.1
1.E+03	1.E-03	1
1.E+04	1.E-04	1
1.E+05	1.E-05	1
1.E+06	5.E-06	5
1.E+07	5.E-07	5
1.E+08	5.E-07	50

On applying a potential difference to the heaters, we find by means of Equation 13.1:

$$\textbf{Power [W]} = \textbf{Voltage [V]}^2 / \textbf{Resistance [Ω]} \qquad (13.1)$$

that the power applied to the heaters were 62mW (5V) and 2244mW (30V).

To provide an independent means to measure the AO fluence to which the zinc oxide sensors have been exposed, carbon-coated quartz crystal microbalances (manufactured by Stabilix, model A OZ) were used. These instruments were connected to a Hewlett Packard 53132A Universal Counter so as to display the oscillating frequency of the crystal; this value was recorded by hand both at the beginning and end of each exposure. The change of frequency (in Hz) would then be converted to AO fluence or total flux F_t by means the Equation 13.2 (provided by the ATOX staff):

$$\textbf{Fluence} = 2.46 * 10^{15}\ \textbf{O-atoms}/(\textbf{cm}^2\ \textbf{Hz}) \qquad (13.1)$$

The above equation was calibrated using Kapton witness samples that were exposed to AO the ZnO.

An AD590 commercially available thermistor was attached in each substrate to monitor the temperature during the first run of experiments. These small integrated circuits were connected to an electronic board that gives an electrical output that can be converted to temperature and saved by the data acquisition system under use.

Problems were experienced when trying to measure the temperature of the sensors while testing in the test chamber. The electronic board initially intended to measure the response of the AD590 temperature sensor was judged not to be working properly during testing, due to readings that indicated erratic temperatures in the films that could not correspond to real test temperatures. In addition to this, later tests on the board indicated that the circuitry that was connected to an AD590 was giving the same temperature readings as the circuitry in the board that was not connected to any temperature sensor.

A determination of the typical temperature during exposure and during regeneration was later performed under similar testing conditions (all the same factors except that the ATOX laser was not turned on). For this purpose, a PT100 thermometer (manufactured by Minco, model number S651PD) was employed in place of the AD590 sensor. It was found that when a potential difference of 5 V is

applied to the sensor heater, this corresponds to a temperature of about 35°C; a potential difference of 30 V corresponds to a temperature of about 135°C ± 2°C.

For the tests carried during the second visit, a group of PT100 thermocouples were successfully used to measure the temperature.

13.2.2 Experiment Set-up

The following types of sensors were tested on the first visit to ATOX; only Type 1 were tested on the second visit:

- Type 1: Pure ZnO dissolved in ESL400 prior to firing.
- Type 2: ZnO (82%) with IP027 (18%).

The aim of these tests was to characterize their response to AO, to determine if it is possible to use the sensors to measure AO flux, to detect if saturation could be achieved with a small fluence, as well as to determine the regeneration properties of the sensors (if any). It was decided not to test Type 3 Sensors (with 70% of ZnO and 30% of IP027) as originally planned because the resistance of this type of sensors was beyond the limit of detection of the instrumentation used for the tests.

With the objective of providing control sensors (not exposed to AO but exposed to the same vacuum, thermal and electrical environment of the exposed sensors), some of the sensors were covered (and thus preventing the AO from impinging on them) with an alumina sheet, the same substrate material used in the deposition of the zinc oxide films. This procedure was intended to help to determine the role of the other-than AO flux conditions in the resistance change (if any) on Types 1 and 2 sensors.

Given the fact that the ATOX facility produces a significant amount of UV radiation during the production of AO, it was required to isolate the effect of that radiation on any eventual change of resistance on sensors of the types tested. Some of the sensors were covered with a 0.25mm thick sheet of quartz (supplied by Goodfellow, catalogue number 720-613-54) that is transparent to radiation between 180nm and 2500nm, but resistant to the attack of AO; the resistance of quartz to AO attack *(Tagawa et al., 1997)* and its UV transparency *(Kopitkovas et*

at., 2004) have been well established. These UV control sensors were exposed to the same electrical, vacuum, and thermal environments as the exposed sensors.

.

Figure 13.4 shows a typical arrangement of three substrates with four sensors in each one, as mounted in the ATOX chamber prior to testing. Kapton tape is seen holding in position a plate of alumina to block one sensor from the AO flux. In the lower right position, a quartz widow can be seen covering one sensor. All sensors were oriented perpendicularly to the AO beam.

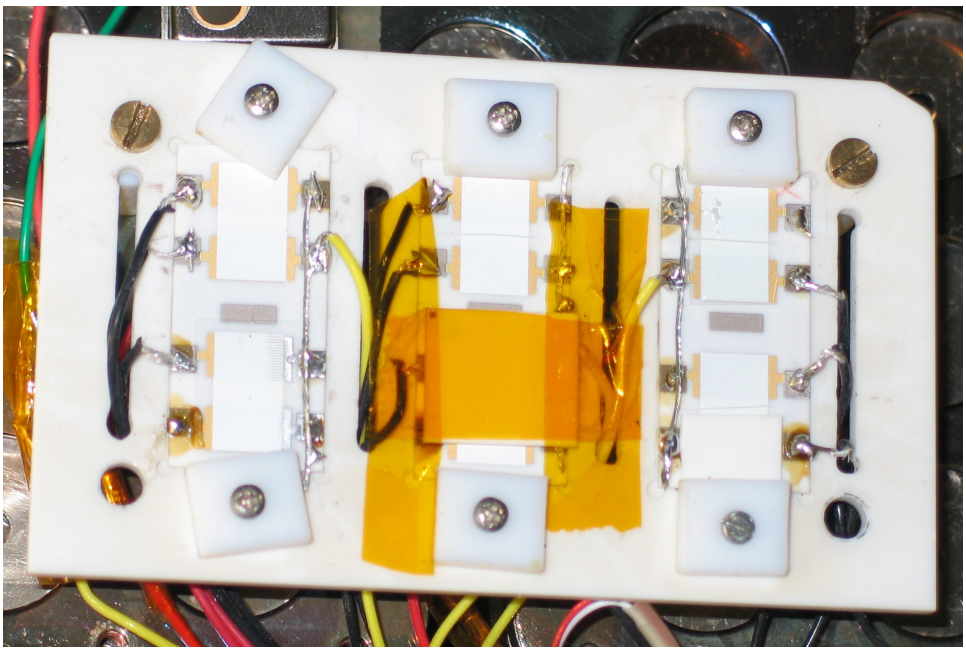

Figure 13.4. Typical Sensor Arrangement for Testing.

13.2.3 Atomic Oxygen Exposure

Multiple runs were carried out with different sensors on both visits to ATOX. The results of both visits tend to agree. For clarity, only results for individual sensors that represent a group tested under the same conditions will be presented. It should be noted that about 15% of all sensors failed at some point during testing. Data is reported here of sensors that were kept for at least three days at a pressure of about 10^{-4} Pa in the sample chamber for outgassing at a temperature of about 135℃ before testing. These conditions have been determined to be enough (see preceding chapter) to reach stable resistance

readings indicating the completion of the outgassing of the sensors, and therefore, surfaces to be clean of adsorbed species. Prior to AO exposure, the temperature was lowered to about 35°C.

The first series of experiments was carried out to determine the response of Type 1 sensors to AO, and to investigate the possibility to regenerate Type 1 sensors after AO exposure by heating. It was also desired to investigate the response of sensors placed in the same chamber but being covered with either alumina or a UV-transparent (quartz) window. The results of such an experiment are shown in Figures 13.5 to 13.8 for one exposed sensor (serial number 110), one sensor covered with quartz (102) and one covered with alumina (112); these results are typical of the whole sample of tested sensors. The time line is as shown in Table 13.2.

Figure 13.5 shows the complete timeline of testing in logarithmic scale of resistance. Significant events are marked on the plot. Note the very large fluctuations in the signals when the pressure conditions change (that is, when the sensors are moved from the sample chamber to the test chamber and back). Some of these fluctuations were accompanied by nearly instantaneous DC resistance readings of 10^{38} Ω which can only be interpreted as brief 'open circuit' readings; these events are depicted in Figure 13.5 as lines going vertically above the scale in the figure. The sensitivity to pressure changes has already been noted and discussed in Section 12.2. The details of the sensors' response to AO and to regeneration heating is further discussed below.

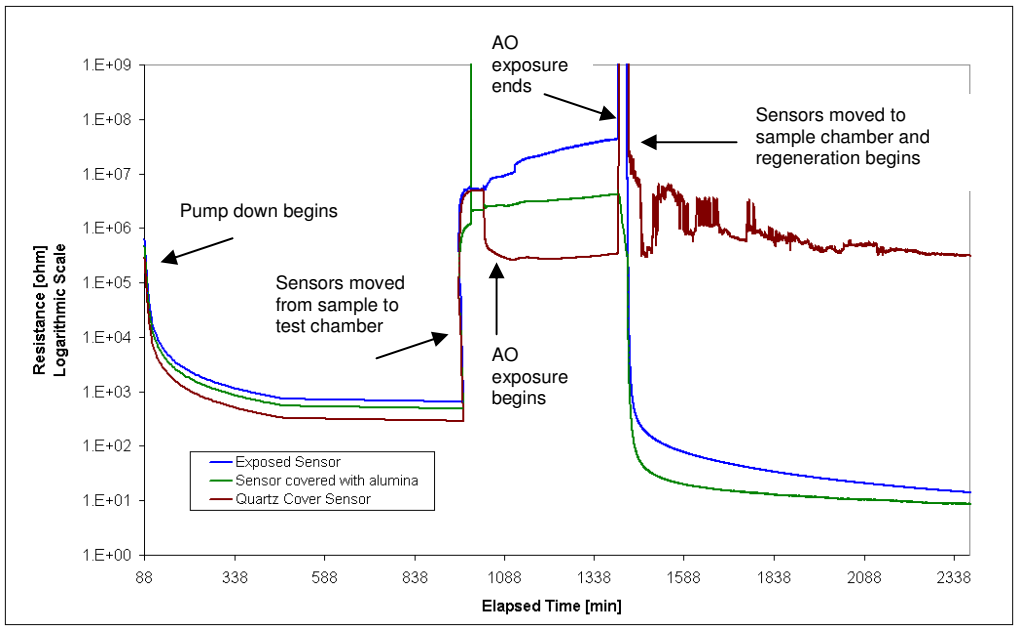

Figure 13.5. Exposure Timeline for sensors 102, 110, and 112.

Table 13.2. Timeline of Events for Testing at ATOX.

Time [min]	Event
88	Sensors in Sample Chamber at 35℃
963	Sensors are moved sample to test chamber
1029-1407	Exposure to AO
1410	Sensors are moved test to sample chamber
1429-2529	Sensors regeneration at 135℃

Figures 13.6 and 13.7, which only show the timeline of exposure to AO, indicate that the sensor exposed to the AO flux increases its resistance as the exposure continues, but the covered sensors only show a very modest increase in resistance as that compared to the exposed sensor. During this exposure, a fluence of 3.2×10^{19} atoms/cm^2 was achieved.

The apparent lack of UV-response noted in the thick film sensor is attributed to the fact that the UV's effects penetrate only just beneath the surface of the thick film; Heiland (1961) showed that the increase of charge carriers due to UV exposure in ZnO goes to up to a depth of the order of 0.1μm, which would

leave the majority of the 10μm-thick film unaffected. The bulk conductance in the thick film sensors may therefore shunt the (predominantly at the surface) effects of UV radiation. This would explain why the present results with regard to UV sensitivity are different from those of other researchers, as documented in Section 10.3.

Figure 13.6 shows that resistance increases nearly linearly with exposure for most of it. In particular, it should be noted that the mere increase in resistance and the fact that this can be measured allows us to use the ballistic model (see Section 9.1) to measure flux. However, it should be noted that since all sensors showed different baseline resistances in vacuum, each would need to be calibrated independently so as to find the constant the relates flux with change of conductivity in time before they can actually be used for AO flux measurements.

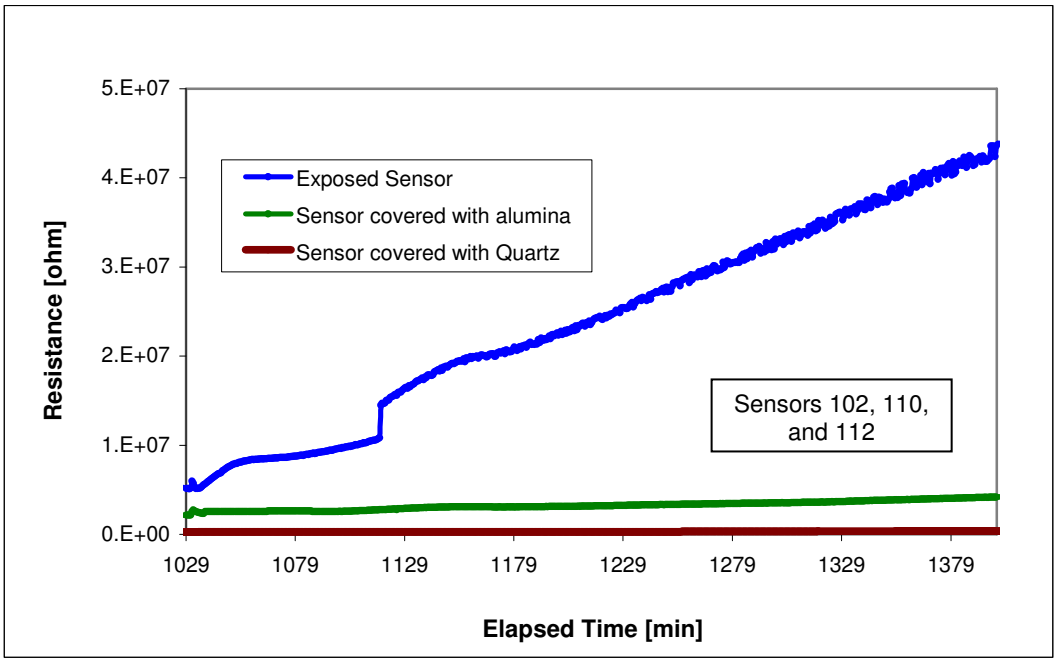

Figure 13.6. Exposure of Type 1 sensors to Atomic Oxygen, and control sensors.

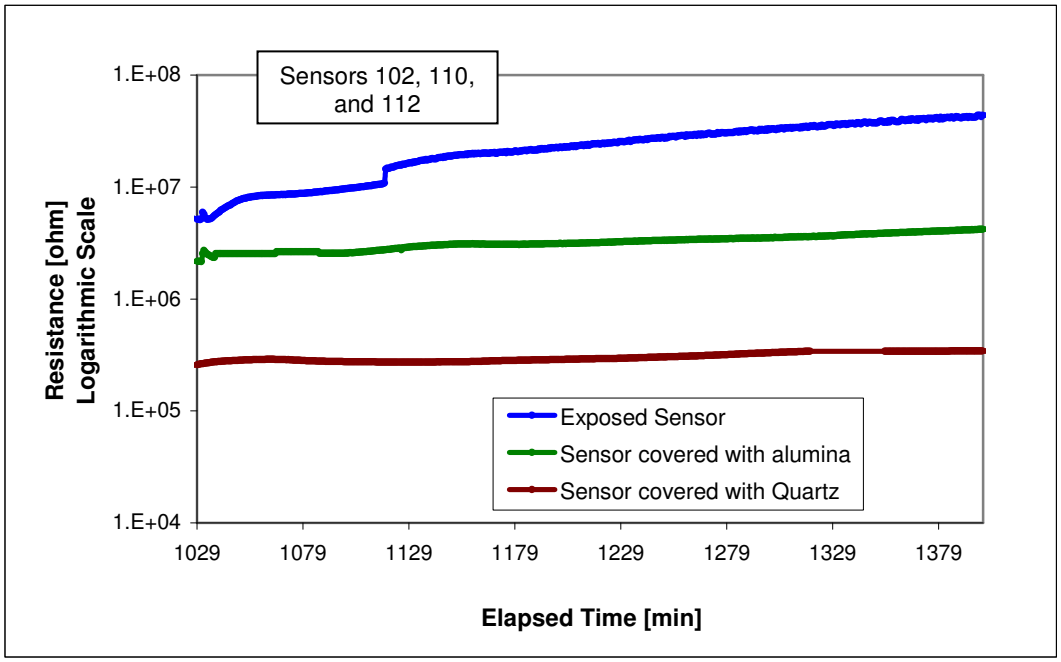

Figure 13.7. Exposure of Type 1 sensors to Atomic Oxygen, and control sensors, logarithmic scale.

Figure 13.8 shows the regeneration event (which took place in the sample chamber): the resistance of the exposed sensor decreases to a value even lower than that of the beginning of the exposure, but similar in magnitude to that in the sample chamber before exposure. The resistance of the sensor covered with alumina also decreases.

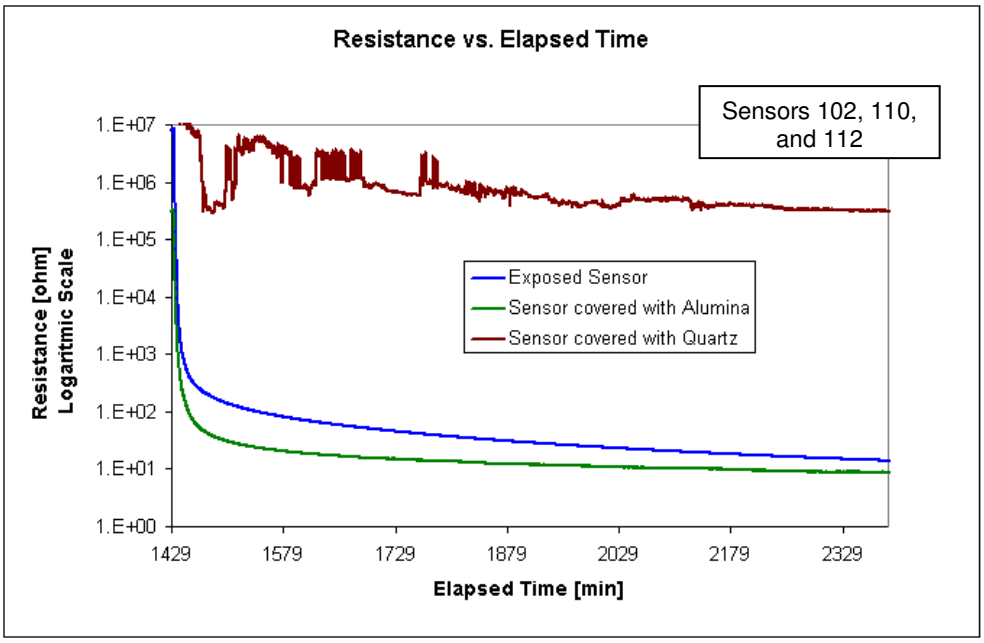

Figure 13.8. Regeneration of Type 1 Sensors.

The sensor covered with the quartz window showed an erratic response (see Fig. 13.8). Figure 13.9 is a picture taken after the tests and shows the sensor had been damaged at some point during those tests. This figure shows a silver appearance on the right side of the gold interdigitated film; it also indicates that some of the ZnO material is missing since the underlying interdigitated gold film is visible. A possible explanation is that solder flux, which is part of the vacuum-grade solder used, may have found its way into the thick film and removed some of the ZnO and damaged some of the gold film. Solder flux, a chemical cleaning agent that removes oxides during soldering and allows the solder to flow easily on the working piece (rather than forming beads as it would otherwise), is usually an acid that could act as a solvent to the ZnO as well as attack gold. An acid attack on the gold interdigitated film may also change its geometry resulting in a permanent change of the measured DC resistance. However, this type of damage was observed on only a few of the films tested over the course of the research programme.

Figure 13.9. Damaged Type 1 Sensor (102) covered with Quartz window.

A separate experiment was carried out to determine the response of Type 1 sensors to subsequent exposures to AO. In between exposures, the sensors were kept in the sample chamber at 35°C and no regeneration was attempted; subsequent exposures took place in successive days. Results are shown in Figures 13.10 and 13.11. The fluence achieved during each exposure is shown in Table 13.3.

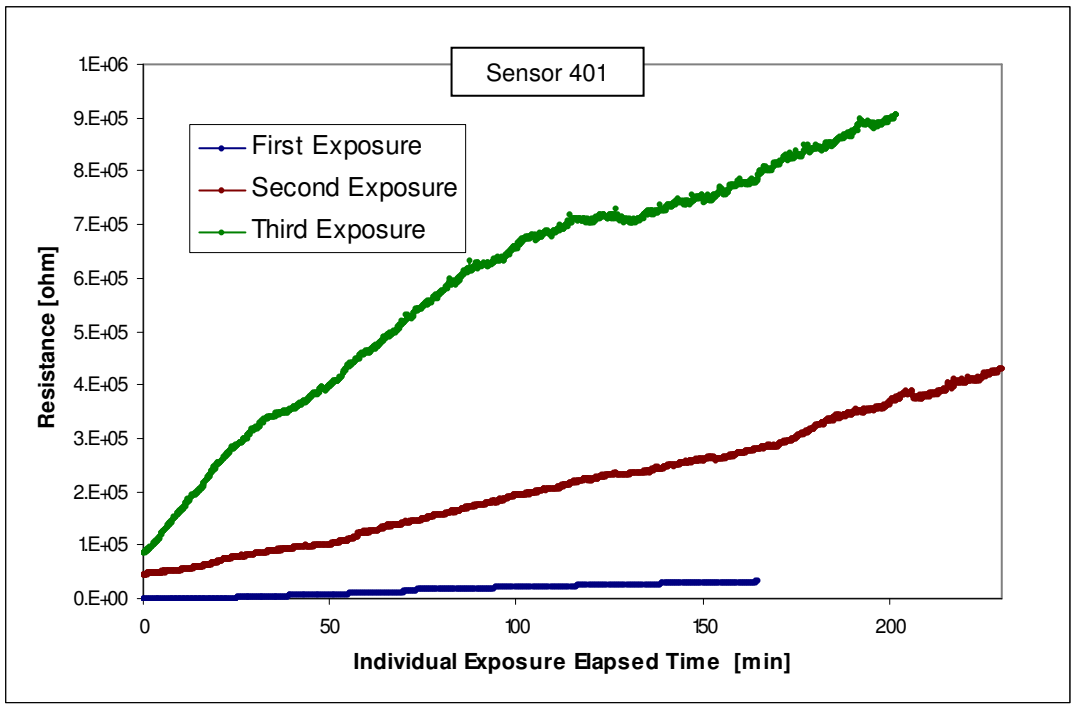

Figure 13.10. Response of a Type 1 sensor to AO.

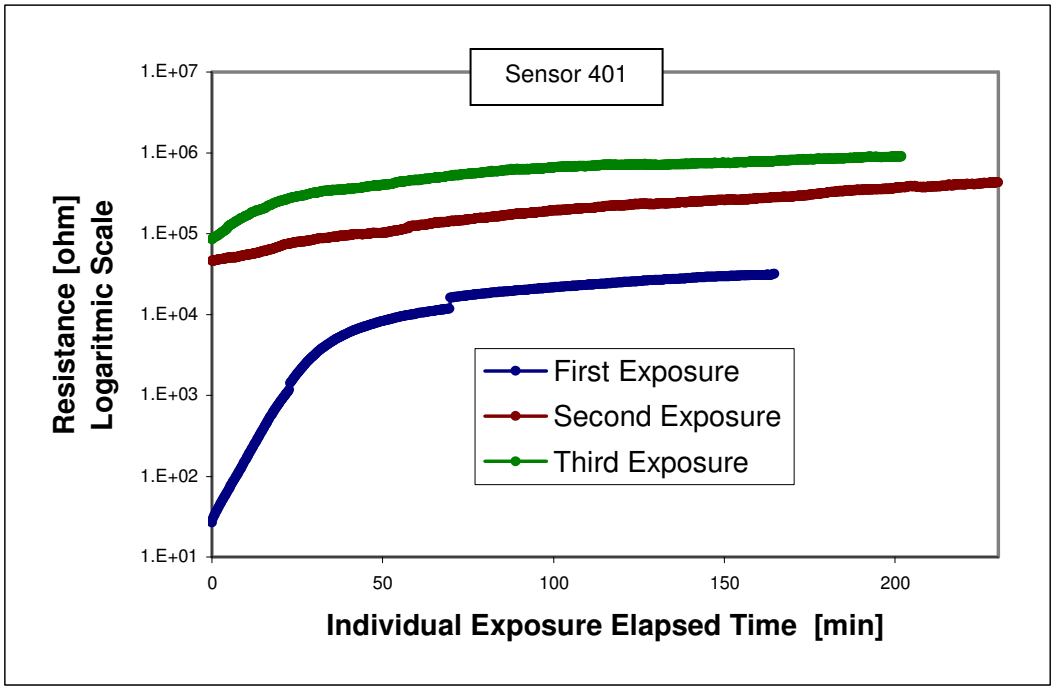

Figure 13.11. Response of a Type 1 sensor to AO.

Table 13.3. Fluence per Exposure

Exposure	Fluence [10^{19} O-atoms cm^{-2}]
1	1.1
2	1.5
3	1.3
Total	3.9

It can be seen that in all exposures, the resistance increases with time, and that this increase takes a near linear form at the beginning of each exposure; the resistance values never exceeded 1 MΩ which means the measured values were within the ohmic range of the sensors. Again, these results can be used to estimate flux by using the model described in Section 9.1 Some peculiar situations are evident: the resistance at the beginning of the second exposure is higher than that at the end of the first exposure; also, the resistance at the beginning of the third exposure is lower than that at the end of the second exposure. It is also shown that the total flux achieved combining the three exposures is not enough to saturate the sensor (a situation that would have rendered no further increase of

resistance with flux); technical limitations of the ATOX source prevented longer exposures.

Figure 13.12 shows the results of different exposures of the same Type 1 sensor to AO in ATOX. The negative of the initial rate of change of resistance is plotted in the vertical axis, with the AO flux on the horizontal axis. The two data points highest flux were attained during the first visit to ATOX; the other two data points were obtained during the second visit. It should be noted that the sensors were heated to 135°C in between each exposure for each visit to ATOX. This figure reveals a nearly linear relationship, as predicted by equation 9.23, with a correlation coefficient of about 93%. These results are typical for most sensors tested.

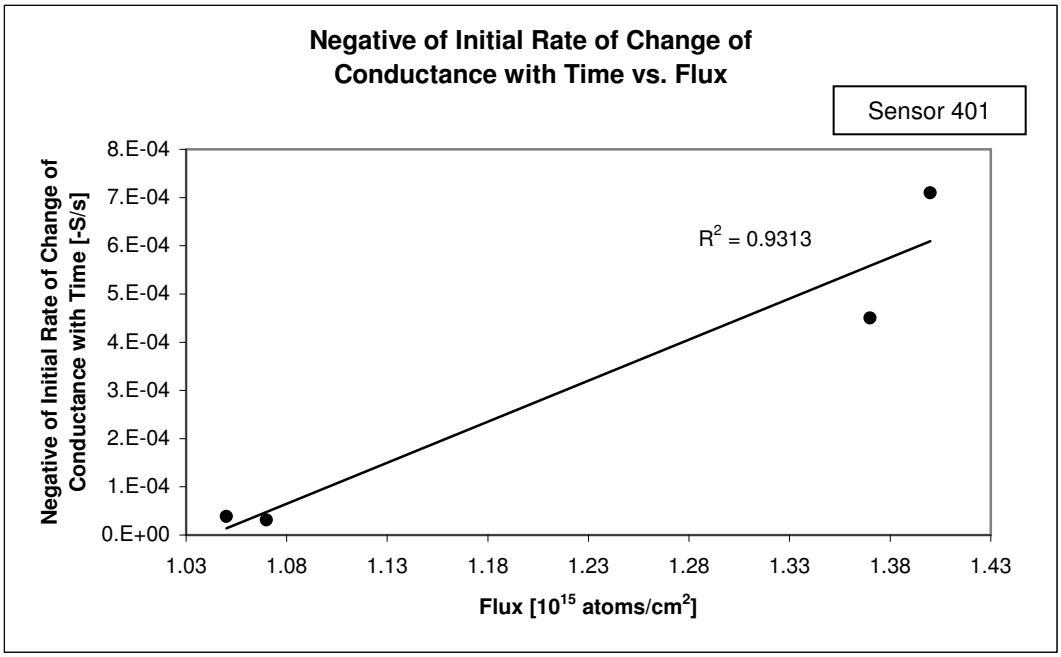

Figure 13.12. Exposure of Type 1 sensors to Different Fluxes of Atomic Oxygen.

As with Type 1 sensors, Type 2 sensors were exposed to AO flux in ATOX, and some were covered with quartz or alumina sheets. The results of such experiment are shown in Figures 13.13 to 13.15 for one exposed sensor (serial number 201), one sensor covered with quartz (200) and one covered with alumina

(202). The results, as well as the regeneration attempt, are shown in Figures 13.13 to 13.15. During this exposure, a fluence of 3.2×10^{19} atoms/cm^2 was achieved. Figure 13.13 shows that the resistance of the exposed sensor increases significantly as the exposure progresses. The same cannot be said about the sensor that only receives the UV from the source, which only increases its resistance modestly. The resistance of the sensor blocked with alumina decreases during the exposure. Figure 13.15 shows the period right after the exposure when the temperature was elevated to 135°C; the resistances of all sensors return to values in the same order of magnitude they had while in the sample chamber before exposure – in particular, the resistance of the exposed sensor reduces to a value lower than that at the beginning of the exposure.

The above results suggest that sensors may have changed their baseline resistance in between exposures. The changes in pressure in between exposures (going back and forth from test to sample chamber) may have altered the surface of these sensors, due to the relatively fragile nature of them.

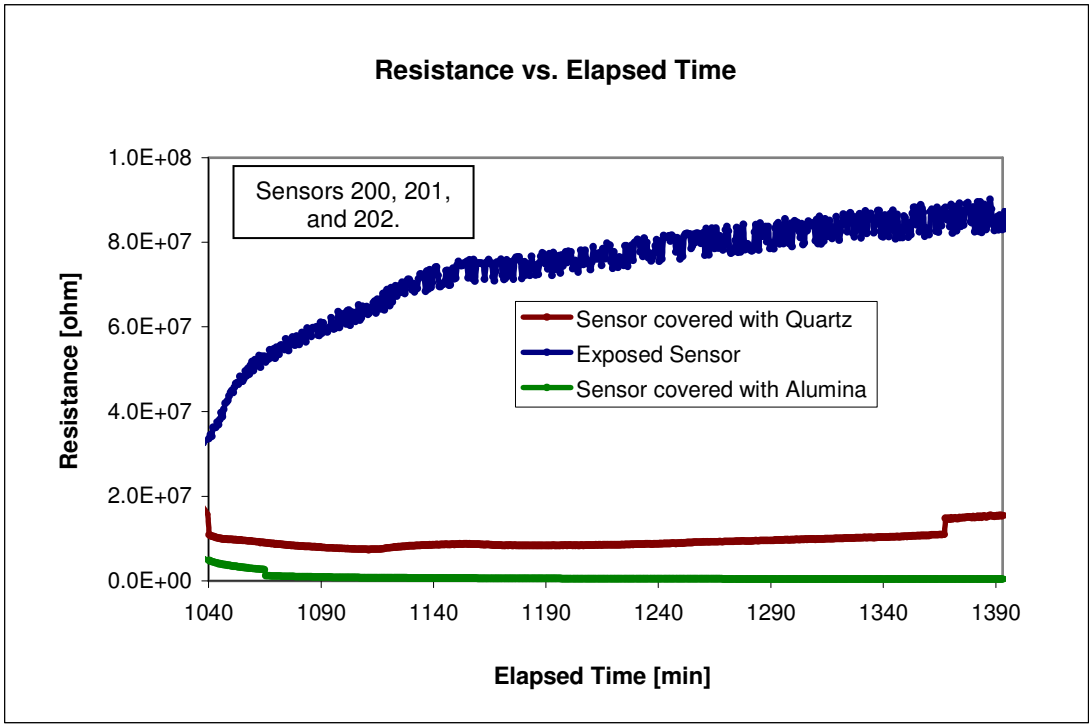

Figure 13.13. Exposure of Type 2 sensors to Atomic Oxygen, and control sensors.

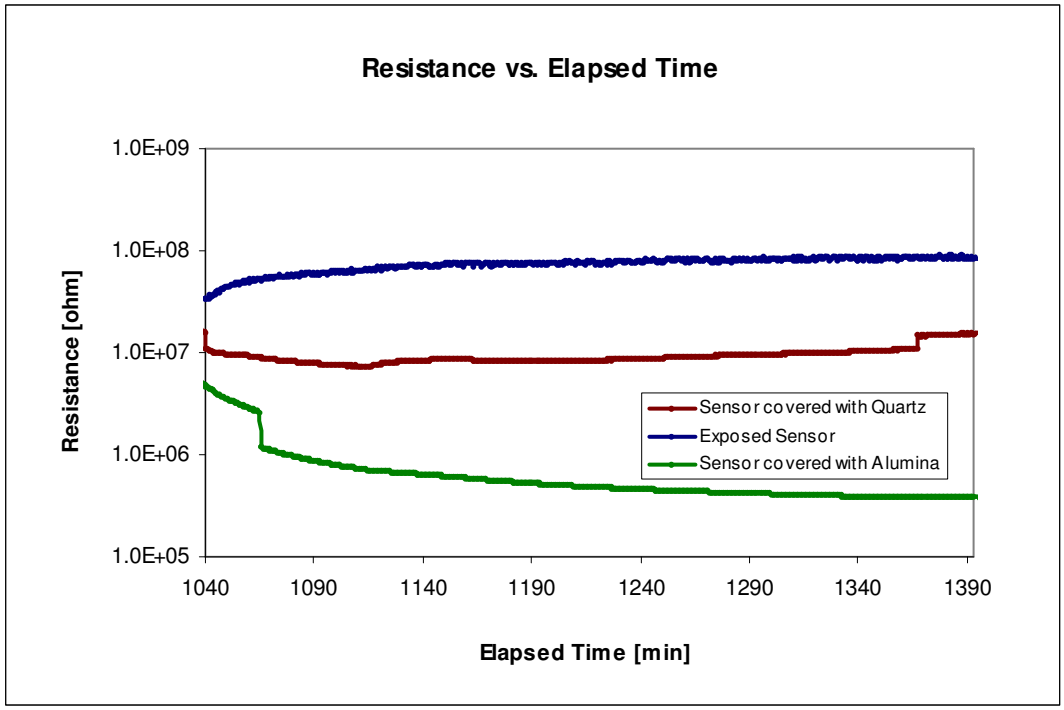

Figure 13.14. Exposure of Type 2 sensors to Atomic Oxygen, and control sensors, logarithmic scale.

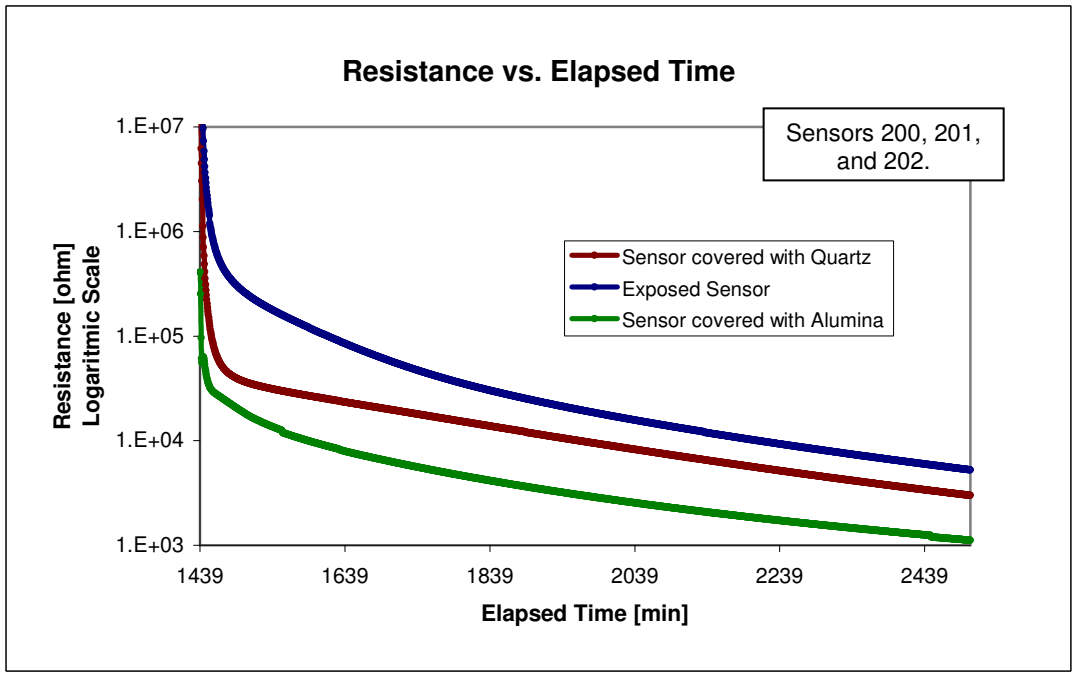

Figure 13.15. Regeneration of Type 2 Sensors.

14. Atomic Oxygen Flux Measurement and Sensor Characterization using Impedance Spectroscopy

The purpose of this package of work was an attempt to characterize the response of Type 1 and 2 sensors using impedance spectroscopy, and to investigate the feasibility of using impedance spectroscopy to measure AO flux. This work included two separate experiments: work in vacuum and exposure to dry O_2 at a laboratory of the University of Southampton for Type 1 and 2 sensos, and exposure to a flux of atomic oxygen at ATOX for Type 1 sensors.

14.1 Exposure to Vacuum and Molecular Oxygen

This work took place at the Astronautics Laboratory of the University of Southampton. The chamber and instrumentation used to measure pressure and temperature are those described in Section 12.2. The Impedance Spectroscopy instrument was an Ivium Technologies Compact Stat Electrochemical Interface, serial number B08033, loaned by the Electrochemistry Group of the Chemistry Department of the same university. A laptop was used to control the impedance spectroscopy equipment by means of the computer application Iviumsoft®, version 1.633; it was also used to record the data.

14.1.1 Type 1 Sensors

A group of five sensors in two substrates spent about three weeks at a pressure of 10^{-3} Pa (also the pressure the vacuum tests were carried at), at temperature between 10°C and 15°C. The settings for the Impedance measurements were as follows: constant potential 0.01 V, frequency range from $4*10^6$ Hz down to 0.1 Hz, and seven readings per decade. They reached a state of stable readings (desorption of atmospheric components was completed) before impedance measurements were taken.

Impedance was first measured in vacuum as the temperature was raised; three different temperatures were used. Later, dry molecular oxygen was allowed

to enter the chamber until reaching atmospheric pressure; two different temperatures were used for these measurements. At least three determinations were performed for each temperature and exposure condition, and the results were averaged to lessen the effect of noise.

Inspection of the Impedance plots and the past experience presented in the literature review (see Section 8.6) suggest that a suitable equivalent circuit to model the behavior of Type 1 ZnO sensors is a resistor for the grain, and a resistor and capacitor in parallel for the grain boundary, such as that depicted in Figure 8.3. Figure 14.1 shows one sample of the scans obtained, where some data points due to noise can be seen; this Nyquist plot shows the real response (Z') on the horizontal axis and the imaginary response (Z'') on the vertical axis, frequency increases from right to left. Figure 14.2 shows the higher frequency data from Figure 14.1 at a higher magnification, to make explicit the intercept of the plot with the horizontal axis.

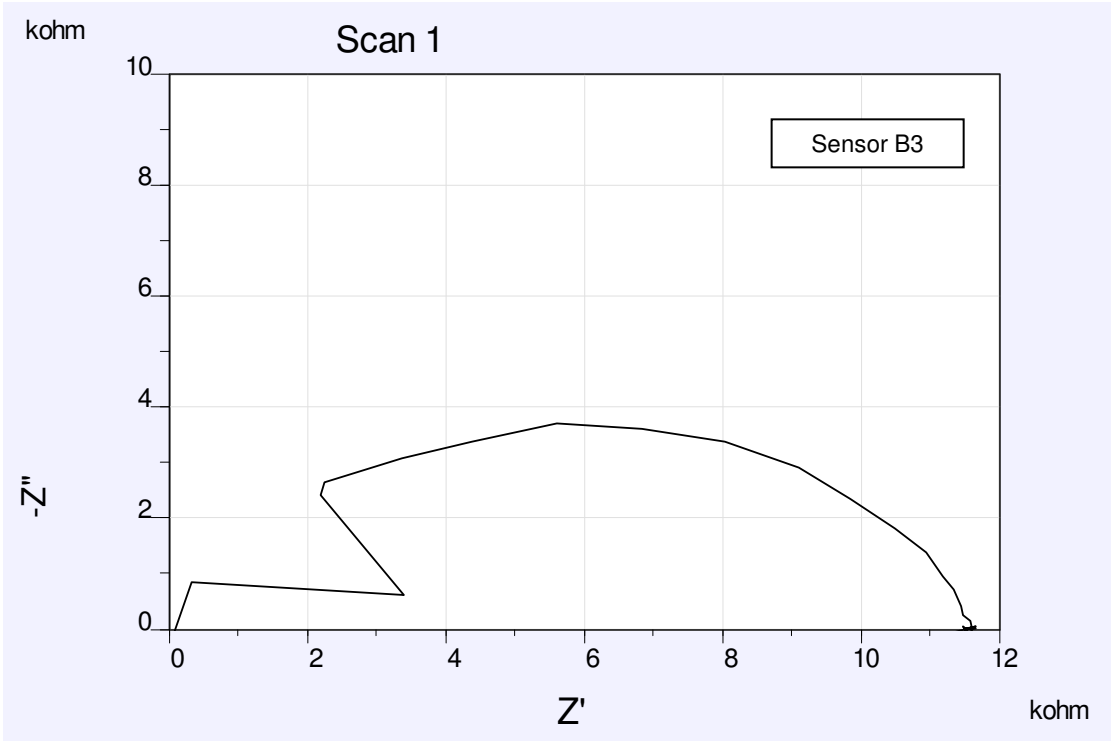

Figure 14.1. Nyquist Plot of ZnO Type 1 Thick Film in Vacuum at 35°C.

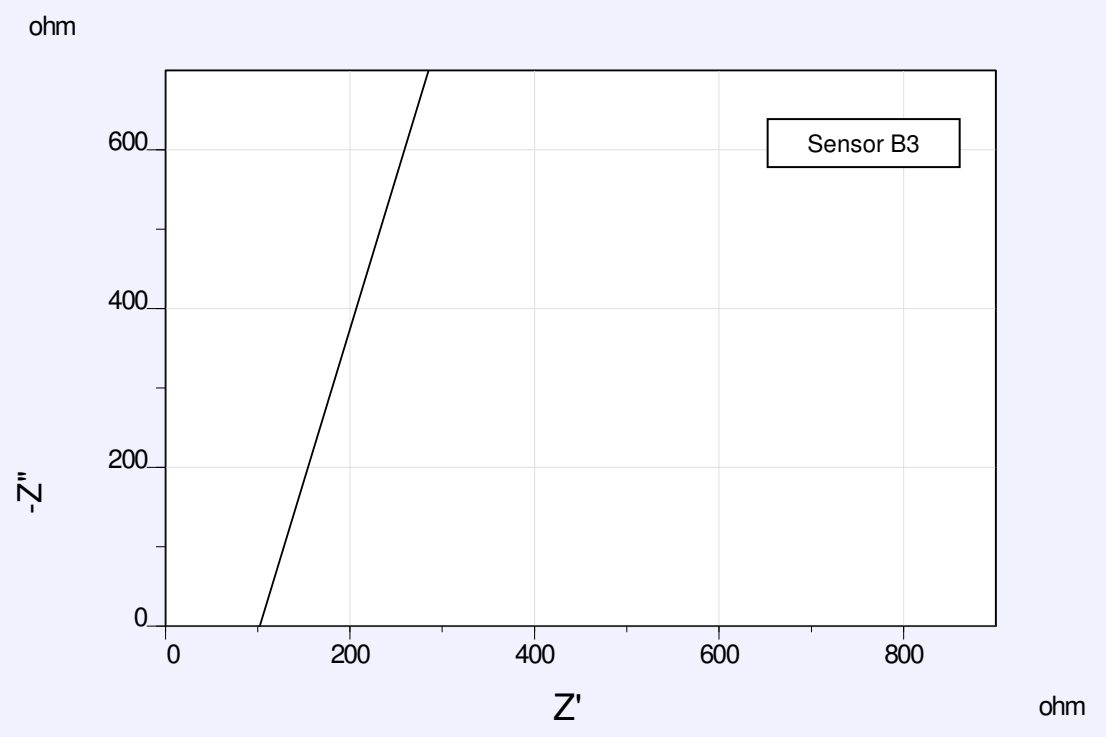

Figure 14.2. Nyquist Plot of ZnO Thick Film in Vacuum; high frequency data from Figure 14.1 but at higher magnification.

The following is a mathematical process to find the equations to calculate resistances and capacitance for the equivalent circuit of Figure 8.3. The total impedance of the circuit is (Equation 14.1):

$$Z = Z_g + Z_{gb} \tag{14.1}$$

The impedance of the grain is just R_g. The Impedance of the grain boundary is given by Equation 14.2:

$$Z_{gb} = \left(\frac{1}{R_{gb}} + j\omega C_{gb} \right)^{-1} \tag{14.2}$$

Therefore the total Impedance is given by Equation 14.3, after adding both terms and rearranging:

$$Z = R_g + \frac{R_{gb}}{1 + j\omega C_{gb} R_{gb}} \tag{14.3}$$

Rearranging the results to separate the real from the imaginary parts, we get:

$$Z(real) = \frac{R_{gb}}{1 + \left(\omega R_{gb} C_{gb}\right)^2} + R_g \tag{14.4}$$

$$Z(imaginary) = \frac{\omega R_g^2 C_{gb}}{1 + \left(\omega R_{gb} C_{gb}\right)^2} \tag{14.5}$$

When the frequency ω is nearly 0, we can find in the real axis:

$$Z(real)_{\omega \to 0} = R_{gb} + R_g \tag{14.6}$$

When the frequency has a very high value, say in the MHz range, we can assume that $\omega \to \infty$ and therefore:

$$Z(real)_{\omega \to \infty} = R_g \tag{14.7}$$

Resistances and Capacitances of the equivalent circuit were calculated using the algorithm included in Iviumsoft®, as well as the above two equations, which were in agreement. Figure 14.3 shows the measured resistance of the grain and the calculated resistances of the grain boundaries as function of temperature for both vacuum and molecular oxygen; this plot is of a sensor that represents well the results from the other four sensors.

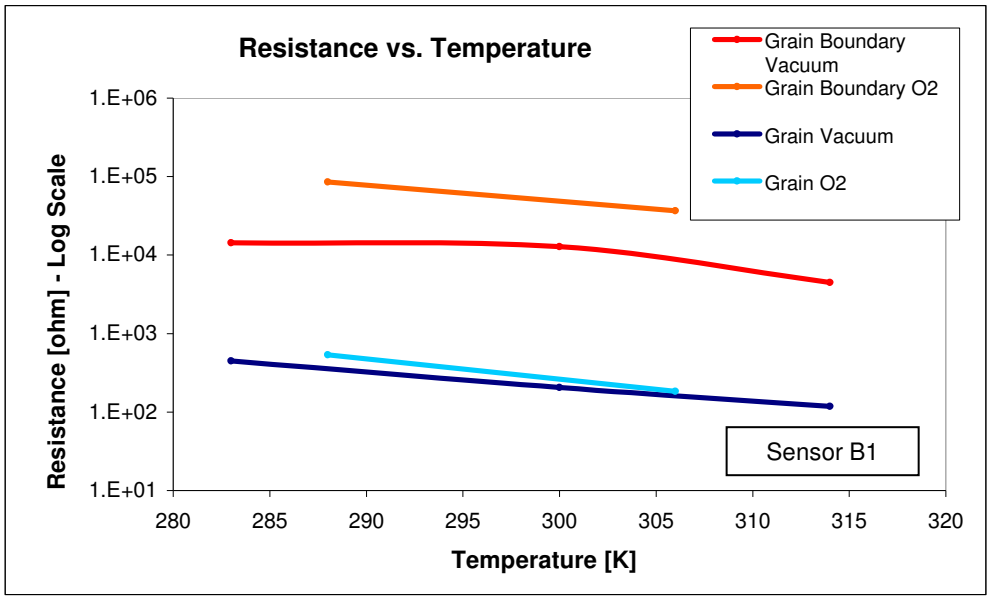

Figure 14.3. Resistance vs. Temperature plots for Type 1 Sensor.

An inspection of Figure 14.3 allows us to draw the following conclusions:

In all cases, resistance values decrease as temperature increases. This is to be expected in a semiconductor like ZnO, and is in accordance with data presented in Section 12.2. Resistance values at the grain boundary are about two orders of magnitude higher than those for the grain bulk, which confirms the existence of an electronic-depletion layer at crystallite boundaries. Resistances measured in vacuum are nearly two orders of magnitude higher for the grain boundaries than for the grain. This relative difference goes even higher when measured in molecular oxygen.

Grain boundary resistance increases by almost one order of magnitude when going from vacuum to molecular oxygen exposure, which in absolute terms means an increase of about 10^4 Ω. The resistance increase for the grain is relatively modest, only of about 10^2 Ω.

The above situation can be explained by the adsorption of molecular oxygen (as O_2^-) at the grain boundaries of the crystallites exposed to the gas. The adsorbed molecular oxygen would take some of the electronic density from the grain boundaries therefore significantly increasing its resistance. The results also

show that there is negligible diffusion of the oxygen into the grains, proved by the modest increase in resistance of the grain when going from vacuum to O_2. This is in agreement with literature reports that molecular oxygen migration into ZnO crystals is very slow.

Therefore the process that controls the response of these sensors is the change of resistance in the grain boundaries, due to adsorption of molecular oxygen.

Figures 14.4 and 14.5 show Arrhenius plots (ln (R) vs. the inverse of Temperature) for one Type 1 sensor, in order to calculate the activation energies of both the grain boundaries and grains, for both vacuum and exposure to molecular oxygen; the equations of the trend lines as well as the correlation coefficients are shown; care should be taken with the interpretation of a correlation coefficient of 1 on each plot, since those curves were obtained with just two data points. The same procedure was carried out for all five sensor and the results are shown in Table 14.1.

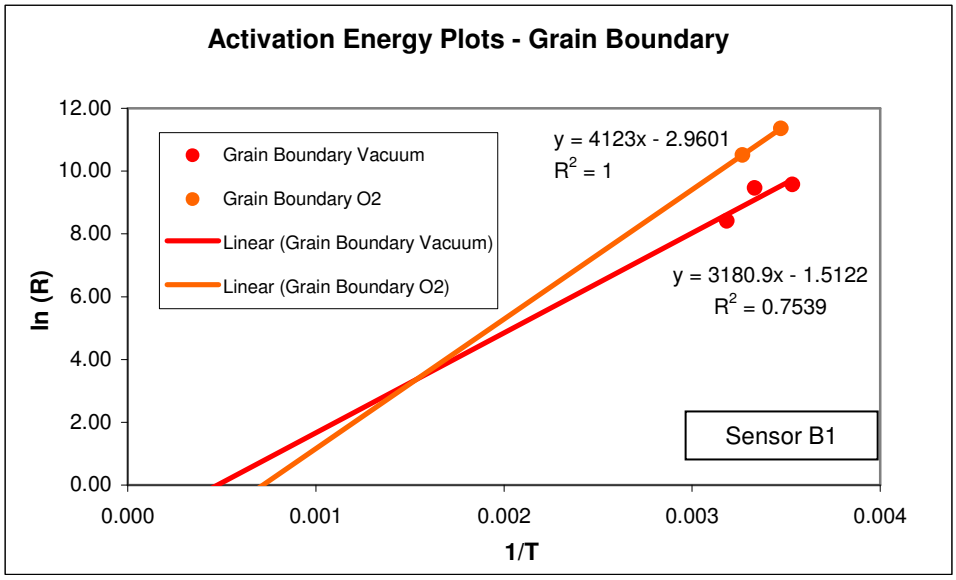

Figure 14.4. Arrhenius plot for the Grain Boundary, Type 1 Sensor.

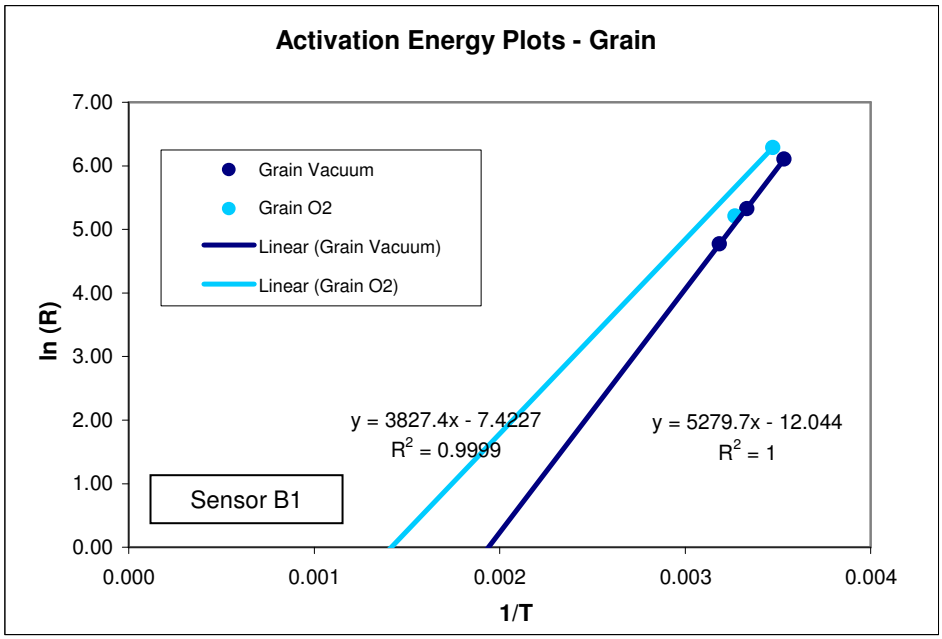

Figure 14.5. Arrhenius plot for the Grain, Type 1 Sensor.

Table 14.1 Activation Energies for Five Type 1 Sensors.

	Grain Boundary Mean [eV]	Standard Deviation	Grain Mean [eV]	Standard Deviation
Vacuum	0.300	0.025	0.314	0.017
Molecular Oxygen	0.381	0.026	0.492	0.038

The conduction activation energies in vacuum are in very close agreement with those published before (0.29eV; see Jose et al., *2001;* and Section 8.2) for both grains and grain boundaries.

14.1.2 Type 2 Sensors

A group of four sensors in one substrate spent about ten days at a pressure of 10^{-3} Pa (also the pressure the vacuum tests were carried at), at a temperature of about 85℃. The settings for the Impedance measurements were as follows: constant potential 1 V, frequency range from $4*10^{6}$ Hz down to 0.1 Hz, and seven readings per decade. They reached a state of stable readings (desorption of atmospheric components was completed) before impedance measurements were taken.

Impedance was first measured in vacuum as the temperature was raised; several different temperatures were used. Later, dry molecular oxygen was allowed to enter the chamber until one third of atmospheric pressure; several different temperatures were used for these measurements. A typical Nyquist Plot is shown in Figure 15.6.

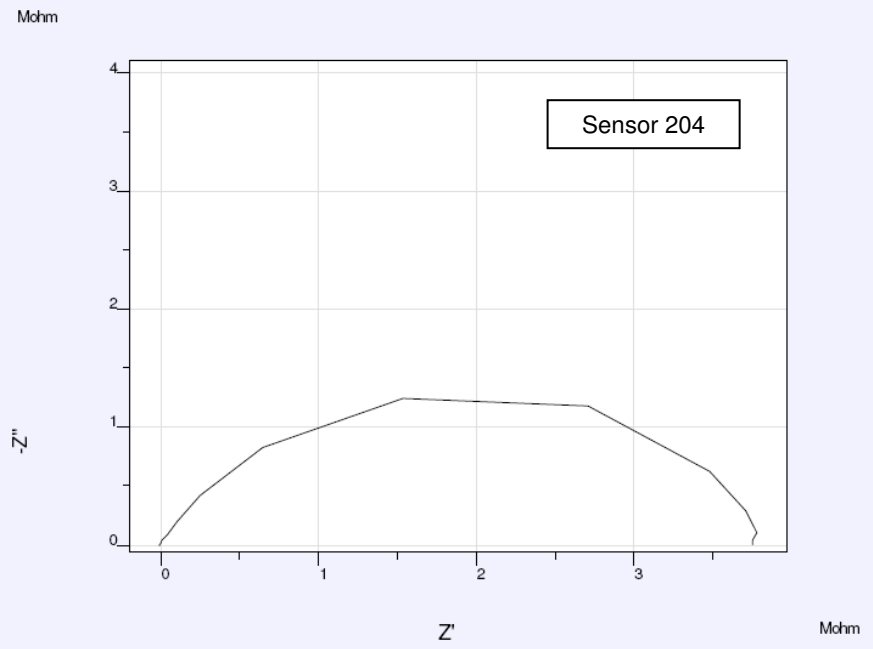

Figure 14.6. Nyquist Plot of ZnO Type 2 Thick Film in Vacuum.

An inspection of all plots reveal only one semicircle; in most cases the plots reveal an intercept with the origin at high frequencies; however, in some instances, noise at high frequency precluded determination of any intercept with the real axis. A possible interpretation of this result is that the total resistance of the sensor has shunted the response of the grain; however, other explanations are also possible and merit further investigation.

Figure 14.7 shows a plot of the natural logarithm of the total resistance vs. the inverse of the absolute temperature. As for Type 1 sensors, the total resistance of Type 2 sensors increase when exposed to molecular oxygen; this is probably due to adsorption of O_2 to the ZnO crystallites. This figure also allows us to calculate the conduction activation energy for this type of sensor, the results being

shown in Table 14.2. This table reveals values about 50% higher than those for the grain boundaries for Type 1 sensors. The role of the binder in the setting conduction activation energies thus merits further investigation.

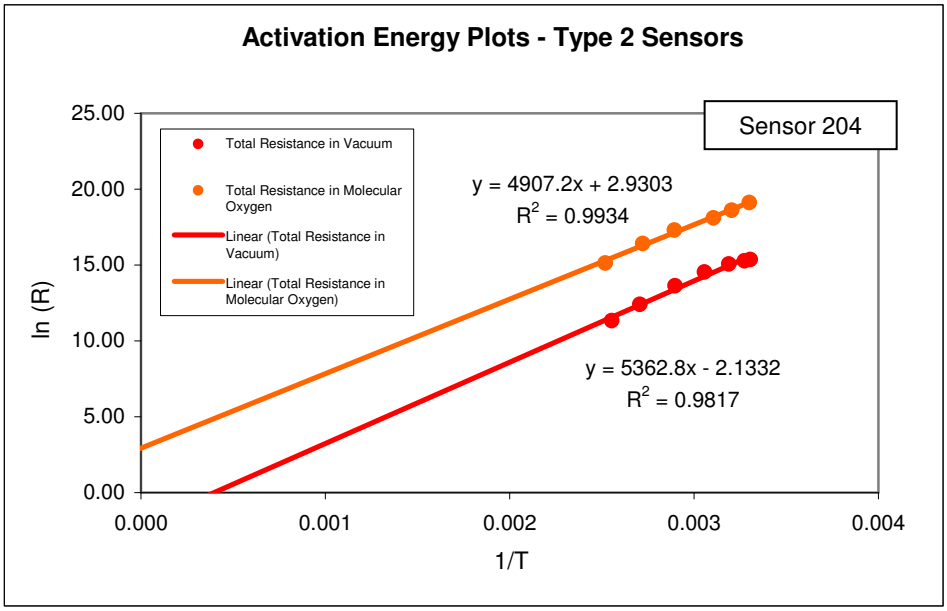

Figure 14.7. Arrhenius plot for the Grain, Type 2 Sensor.

Table 14.2 Activation Energies for Four Type 2 Sensors.

	Total Resistance [eV]	Standard Deviation
Vacuum	0.462	0.039
Molecular Oxygen	0.423	0.035

14.2 Exposure to Atomic Oxygen

This work took place at the ATOX facility of the European Space Agency in February 2009; this facility has already been described in Section 13.2.1. The Impedance Spectroscopy instrument used is that described in Section 14.1. Three Type 1 sensors were installed in the sample tray of the ATOX chamber. The sensors were left at 135℃ for three days at a pressure of about 10^{-4} Pa. A number

of preliminary impedance measurements in vacuum with no AO flux were taken using the same parameters as described in Section 14.1, but the noise of all the electronics in the laboratory precluded any useful readings. The voltage had to be increased to 1 V (still within the ohmic-range of these sensors) to obtain clear results. The settings for the impedance measurements were finally as follos: constant potential 1 V, frequency range from $4*10^6$ Hz down to 0.1 Hz, and five readings per decade; temperature of 35°C.

During the operation of the laser (necessary to produce the AO flux), the level of noise was such that it prevented any clear measurements even with the settings listed in the previous paragraph. So it was decided to stop the flux every 30 minutes to take a measurement, regretting that no measurements during the AO could be taken. Each measurement took about 20 seconds, with a total of no more than two minutes with the AO source stopped in between exposures. This means that an error of 20 seconds/30 minutes, that is, 1% could be expected versus an ideal operation without interruption of the source.

Kapton witness samples were also placed in the chamber to calibrate a microbalance, used to independently monitor AO flux, by means of the change of frequency of its sensing element. The results of the calibration are shown in Figure 14.8; they assume that the flux was constant in magnitude during the whole exposure, which is reasonable given the experience in using this equipment. The speed of AO was also monitored and found to be around 8 Km/s or an energy equivalent to 5 eV.

Figure 14.9 shows a Nyquist Plot of impedance measurements taken at intervals of 30 minutes for one Type 1 sensor; this response is typical of all sensors tested. It can be seen that total impedance (the low frequency intercept of each measurement with the real axis) increases with fluence. The lowest impedance measurement shows a data point that departs from the semicircle at a low frequency; this response, which can be attributed to noise, is also typical of the data taken.

Figure 14.9 also shows that the resistance of the grains is overshadowed by the significantly higher value of the resistance of the grain boundaries; grain resistance does not significantly vary as the exposure continues, remaining at values less than 100 Ω. These results show that the change of resistance is due to

AO adsorption at the surface, reducing the electronic concentration available for conduction at the grain boundary, with negligible or null diffusion of adsorbed species into the grains.

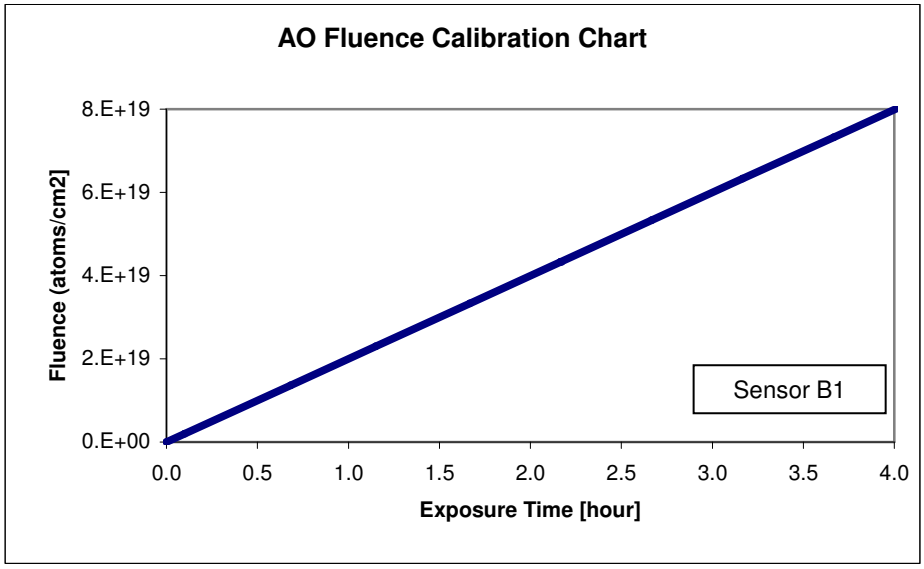

Figure 14.8. AO Fluence with Exposure Time calibration chart.

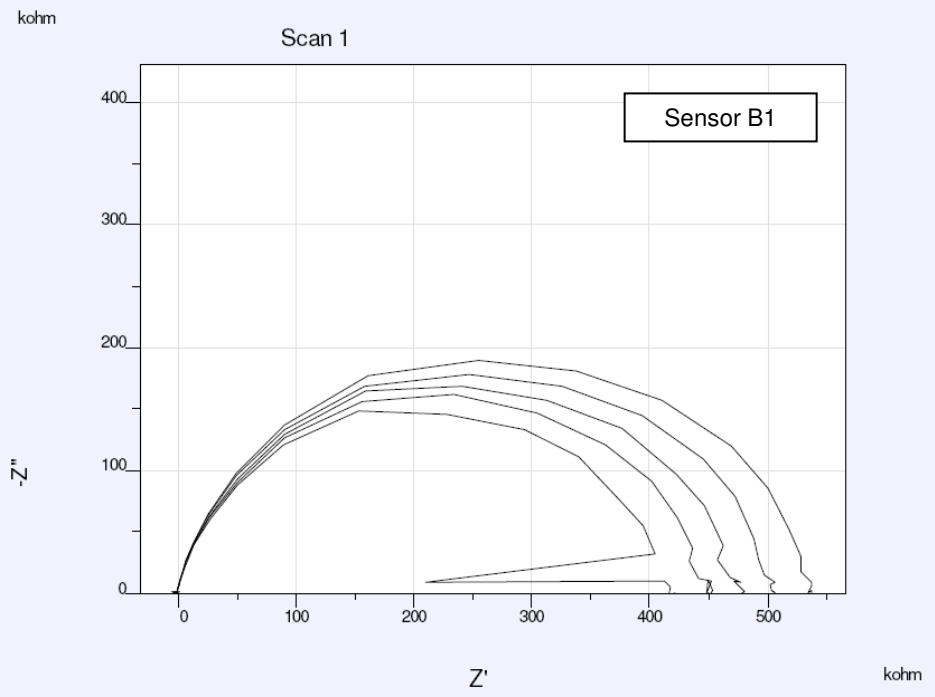

Figure 14.9. Successive Impedance Measurements in 30 min intervals.

Figure 14.10 shows total real impedance data plotted versus fluence at exposure elapsed time for the same sensor and fluence; total impedance shows a linear response to AO flux (the linear curve of regression has a coefficient of correlation of almost 1). This result enables to use the modified ballistic model (see Section 9.2) to measure AO flux by measuring resistance. It should be noted that all sensors had a different baseline resistance in vacuum, so each sensor would need to be calibrated (in other words, find the constant that relates flux with change of conductance at the beginning of the exposure) independently.

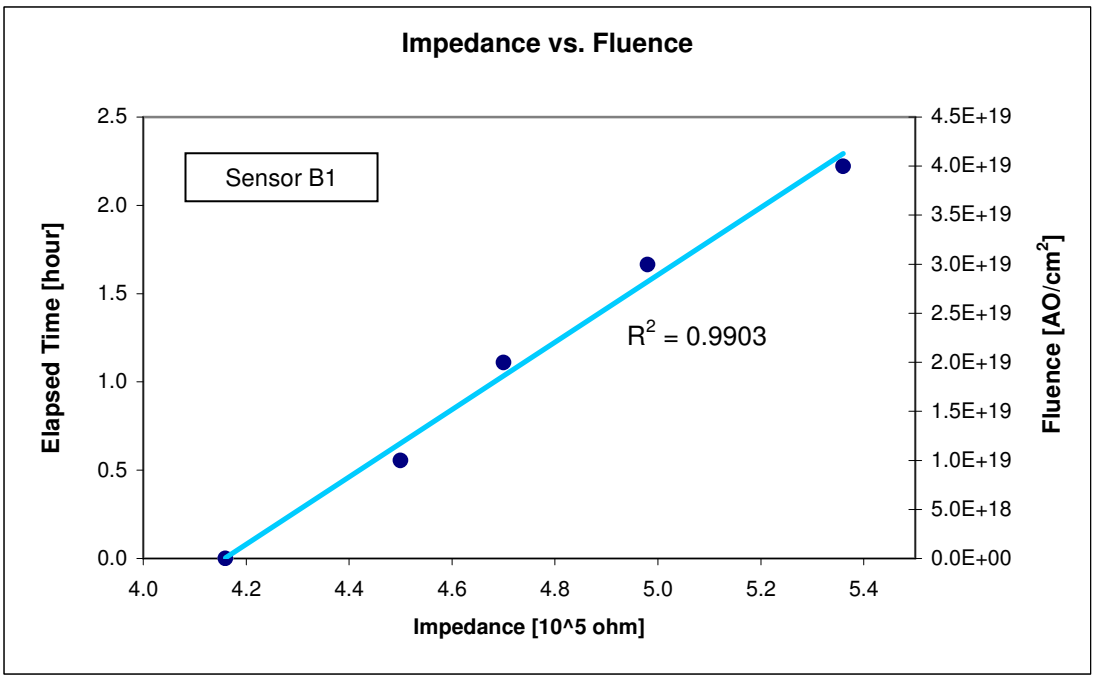

Figure 14.10. Total Impedance vs. Exposure Time and Fluence

15. Conclusions and Recommendations

Thick film ZnO sensors have been developed that are capable of measuring AO fluxes similar to those present in low Earth orbit. Two versions of screen-printed ZnO thick film sensors have been produced and tested; Type 1 sensors are made of pure ZnO while Type 2 use 18% in weight of a glass binder. The sensors have been characterized using a number of techniques, including Scanning Electronic Microscopy (SEM) and Energy Dispersive X-ray Spectroscopy (EDS). The response of these sensors to vacuum, changes in temperature and pressure, and while exposed to different gases has been assessed by means of DC resistance and impedance spectroscopy measurements.

It has been shown that a reduction in atmospheric pressure will reduce the DC resistance in Type 1 and Type 2 sensors. For Type 1 sensors, separate measurements with dry O_2 and wet N_2 suggest that the both water and molecular oxygen adsorb at the surface of these sensors taking a negative electronic charge, resulting in a decrease of electronic density available for conduction with the resulting increase in sensor resistance.

An increase in temperature in Type 1 and Type 2 sensors will result in a decrease in resistance. This can be explained by the increase of energy available for electrons to migrate from the valence to the conduction band.

Electrical characterization of Type 1 and 2 sensors show ohmic behavior for voltages up to 3.3 V result that is in agreement with published data. For higher voltages, the sensors show a clear departure from ohmic behavior.

It has been shown that Type 1 and 2 sensors do not significantly respond to ultraviolet radiation. This may be due to the limited penetration of UV into ZnO, which is of about 0.1µm as reported in the literature: the bulk conductance in 10 µm-thick sensors may shunt the effects of UV radiation.

Type 1 and 2 sensors show an increase (nearly linear for Type 1) of resistance with LEO-like atomic oxygen flux, for a fluence of 3.2×10^{19} atoms/cm^2; the best explanation available is the adsorption of the oxygen atoms by each atom

taking one electron from the surface of the sensor. Type 1 sensors are the first ZnO thick film sensors developed for space applications that successfully have measured AO flux (a model to convert conductance change with time to AO flux has been provided for Type 1 sensors). Type 1 and Type 2 sensors have also been regenerated by suitable heating, providing in principle the ability to reuse them an unlimited number of times for AO measurements; this has only being achieved before by the ZnO thin films produced by Osborne *(1999).* However, each sensor needs to be individually calibrated due to the significant variation in baseline DC resistance among them. A continuous fluence of $3.2x10^{19}$ atoms/cm^2 or a fluence of $3.9x10^{19}$ atoms/cm^2 accumulated in three exposures are not enough to saturate Type 1 sensors.

Type 1 sensors have been characterized by means of Impedance Spectroscopy. It has been found that the two components that make up the sensor resistance are the crystallites' grain boundary resistance and the crystallites' grain resistance; the value of the former is significantly higher than that of the latter and drives the overall resistance response. When exposed to molecular oxygen, the grain boundary resistance increase can be up to two orders of magnitude more than that of the grain, suggesting the adsorption of molecular oxygen takes place by removing some of the electronic density from the grain boundaries. Impedance spectroscopy measurements were taken while the sensors were exposed to AO; total impedance and grain boundary resistance offer an alternative measurable quantity to determine AO fluxes when the resistance of sensors goes beyond the measurement range of ordinary instruments. This is the first time that Impedance spectroscopy has been employed to characterize sensor response to LEO-like AO fluxes and to measure such fluxes.

Type 2 sensors have also been characterized by Impedance Spectroscopy, although not as comprehensively as Type 1 sensors. It has been found that Type 2 sensors increase the magnitude of total resistance (the real component in a Nyquist plot) as the sensors goes from vacuum to an atmosphere of dry molecular oxygen with a pressure of one third of an atmosphere.

Mechanical testing of Type 1 sensors shows some level of fragility; when scratched with a sharp object, material can be removed from the substrate. SEM pictures reveal cracks and valleys in the surface of most sensors, as well as many pores. Type 2 sensors have shown a much higher resistance to damage; however,

features that resemble craters are often found. The surface characteristics of the sensors can explain the large variation of baseline (in vacuum after desorption is completed) resistance among individual sensors, and the large number of hours required for desorption of atmospheric components to be completed. The high level of porosity observed allows the sensors to be operated with high AO fluences before they become saturated, a situation that was not observed during testing.

The sensors developed in this research have show n some advantages and disadvantages over other sensors used to measure AO flux (such as carbon and silver actinometers, and carbon and silver coated quartz microbalances). Some advantages over them are the ability for regeneration, and low cost of manufacture and operation. Another advantage is the large fluence that is required to saturate them; saturation was not achieved even with fluences one hundred times those required to saturate the thin films produced by Osborne (1999). A particular advantage of the ZnO thick films vs. silver actinometers is that the former present a linear response to AO flux for a much higher fluence than the latter, which change the slope of the response when AO diffusion assumes a more significant role in the DC resistance. Furthermore, the ZnO thick sensors do not seem to react to UV radiation, which is present in LEO.

How ever, the thick film sensors are not as robust as for example, thin ZnO films, or carbon and silver actinometers developed by other researchers. More effort needs to be spent resolving this issue before manufacturing sensors capable of space flight. Another issue is the large variation of baseline resistance between different ZnO thick film sensors of the same production batch, which is a problem other actinometers and coated quartz crystal microbalances do not normally have.

It is recommended that further work is carried out to fully understand the behavior and response of thick film sensors with a binder. More work is required to find the right percentage of binder required to provide a smooth sensor surface that in turn provides more repeatability among sensors. More impedance spectroscopy analysis should be carried out to determine the equivalent circuit that models the electrical response of sensors with a binder, and use these results to modify the ballistic model to account for the glass present in the sensors.

References

Andres-Verges, M., West, A.R., (1997), “Impedance and Modulus Spectroscopy of ZnO Varistors”, Journal of Electroceramics 1:2, pp. 125-132.

Arshak, K., Gaidan, I., (2004), “Development of a novel gas sensor based on oxide thick films”, Materials Science and Engineering B, vol. 118, pp. 44-49.

Arshak, K., Gaidan, I., Cavanagh, L., (2005), “Screen-printed Fe_2O_3/ZnO thick films for gas sensing applications”, JMEP, vol. 2, no. 1, first quarter.

Asokan, T., Freer, R., (1993), “Grain and Grain Boundary Conduction in Zinc Oxide Varistors Before and After DC Degradation”, Journal of the European Ceramic Society, vol. 11, pp. 545-550.

ASTM standard E2089-00, (2006), “Standard practices for ground laboratory atomic oxygen interaction evaluation of materials for space applications”.

Atkinson, J., et al., (1992), “Thick-Film Technology: Theory and Applications”, Short Course Notes by the Thick Film Unit of the University of Southampton.

Banks, B.A., Rutledge, S.K., Brady, J.A., (1988), “The NASA atomic oxygen effects program,” Proc. 15th Space Simulation Conference, NASA CP-3015, pp.51-65.

Bhattacharyya, P., Basu, P.K., Saha, H., Basu, S., (2007), “Fast response methane sensor using nanocrystalline zinc oxide thin films derived by sol–gel method”, Sensors and Actuators B , vol. 124. pp. 62–67.

Berman, A., (1996), “Water in Vacuum Systems”, Vacuum, Vol. 47, Number 4I, pp. 327-332.

Binesti, D., Bonnet, J.P., Onillon, M., Salmon, R., (1986), Journal de Physique, Supplement 2, vol. 47, pp. 919-923.

Caillaud, F., Smith, A., Baumard, J.F., (1991), “Effect of Oxygen Chemisorption on the Electrical Conductivity of Zinc Oxide Films Prepared by a Spray Pyrolysis Method”, Journal of the European Ceramic Society, vo. 7, pp. 379-383.

Caledonia, G.E., Krech, R.H., and Green, B.D., (1987), “A High Flux Source of Energetic Oxygen Atoms for Materials Degradation Studies,” AIAA Journal, 25, no. 1, pp 59-63.

Caledonia, G.E., (1988), “Laboratory Simulations of Energetic Atom Interactions Occurring in Low Earth Orbit,” Rarefied Gas Dynamics: Space-Related Studies, Muntz, E.P., Weaver, D.P., and Campbell, D.H., (eds), Progress in Astronautics and Aeronautics, 116, pp 129-142.

Caledonia, G.E., Holzclaw, K.W., Green, B.D., Krech, R.H., (1990), “Laboratory Investigation of Shuttle Glow Mechanisms”, Geophysical Research Letters, Vol. 17, No. 11, Pages 1881-1884.

Caledonia, G.E., Holzclaw, K.W., Krech, R.H., Sonnenfroh, D.M., (1993), “Mechanistic Investigations of Shuttle Glow”, Journal of Geophysical Research, Vol. 98, No. A3, Pages 3725-3730.

Caledonia, G.E., Krech, R.H., and Oakes, D.B., (1994), “Laboratory Studies of Fast Atom Interactions With Materials,” in Proceedings of the 6th International Symposium on Materials in a Space Environment, ESTEC, Noordwijk, The Netherlands, pp 285-290, 19th-23rd Sep. 1994.ESA SP-368.

Chandra, P., Tare, V.B., and Sinha, A.P.B, (1967), “Optical and Electrical Properties of Zinc Oxide Single Crystals,” Indian Journal of Pure and Applied Physics, 5, no. 1, pp 6-9.

Cimpoiasu, A., van der Pers, N.M., de Keyser, Th.H., Venema, A., Vellekoop, M.J., (1996), “Stress control of piezoelectric ZnO films on silicon substrates“, IOP Publishing Ltd., 0964-1726/96/060744+07.

Collins, R.H., Thomas, D.G., (1958), Phys. Review, No. 112, 388.

Comini, E., Faglia, G., Ferroni, E., Sberveglieri, G., (2007), “Gas sensing properties of zinc oxide nanostructures prepared by thermal evaporation”, Applied Physics A – Materials Science & Processing, vol. 88, pp. 45–48.

Cross, J.B., Blais, N.C., (1988), “High energy/intensity CW atomic oxygen beam source,” Rarefied Gas Dynamics: Space-Related Studies, Muntz, E.P., Weaver, D.P. and Campbell, D.H. (eds), Progress in Astronautics and Aeronautics, vol. 116, pp.143-156.

Dachun, Z., Zhongkai, Q., (1999), “Electronic structure, depth profile, and complex impedance spectroscopy of Pd doped ZnO untrafine particle films”, J. Vac. Sci. Technology, A 17(5), Sept/Oct 1999.

de Groh, K.K., Banks, B.A., (1994), “Atomic-oxygen undercutting of Long Duration Exposure Facility aluminized-Kapton multilayer insulation”, Journal of Spacecraft and Rockets, v 31, n 4, July-Aug, 1994, p 656-664, ISSN: 0022-4650.

Dhananjay, Nagaraju, J., Krupanidhi, S., (2007), “Investigations on zinc oxide thin films grown on Si (1 0 0) by thermal oxidation”, Materials Science and Engineering B, vol. 137, pp. 126-130.

Dylla, H.F., Manos, D.M., LaMarche, P.M., (1993), Vat Sci Technol A, II, 2623.

Eger, D., Goldstein, Y., and Many, A., (1975), “Oxygen Chemisorption and Photodesorption Processes on ZnO Surfaces,” RCA Review, 36, pp 509-530.

Elias, L., Ogryzlo, F.A., Schiff, H.I., (1959), Canada. J. Chem., Vol. 37, p. 1690.

Elsey, R.J., (1975), “Outgassing of vacuum materials”, Vacuum, Vol 25, page 299, and page 347.

Erhart, P., Albe, K., (2006), “First-principles study of migration mechanisms and diffusion of oxygen in zinc oxide”, Physical Review B 73, 115207.

Fortescue, P., Stark, J., Swinerd, G., (editors, 2003), “Spacecraft Systems Engineering”, Third Edition, Wiley, ISBN-10: 0471619515.

Fabricius, H., Skettrup, T., and Bisgaard, P., (1986), “Ultraviolet Detectors in Thin Sputtered ZnO Films,” Applied Optics, 25, no. 16, pp. 2764-2767.

Freer, R., Leach, C., “Local properties of grain boundaries in semiconducting ceramics”, Solid State Ionics, 173, pp. 41-50.

Fox, J.L., Goodhew, P.J., Humphreys, F.J., Beanland, R., (2000), “Red and green lines of atomic oxygen in the nightglow of Venus”, Advances in Space Research, v 10, n 5, Venus Atmosphere, 1990, p 31-36.

Gabriel, S.B., (1997), “The Feasibility of Zinc Oxide as a Detector For Atomic Oxygen”, Final report under ESA-ESTEC contract no. 11702/95/NL/PB, University of Southampton.

Gabriel, S.B., Osborne, J.J., Roberts, G.T., (1997), “Development of a Renewable Atomic Oxygen Sensor for Low Earth Orbit”, Journal of Spacecraft, vol. 35, no. 3, pp. 413-415.

Gamry Instruments, (2007), Application Note, Rev. 5.

Goncalves, G., Pimentel, A., Fortunato, E., Martins, R., Queiroz, E.L., Bianchi, R.F., Faria, R.M., (2006), “UV and ozone influence on the conductivity of ZnO thin films”, Journal of Non-Crystalline Solids, 352, pp. 1444-1447.

Harris, I.L., Chambers, A.R., Roberts, G.T., (1997), “A Low Cost Microsatellite Instrument for the in situ Measurement of Orbital Atomic Oxygen Effects”, Rev. Sci. Instrum., Vol. 68, No. 8, pp. 3220-3238.

Hedin, A.E., (1988), “Atomic oxygen modeling in the upper atmosphere,” Planetary and Space Science, Vol. 36, no. 9, pp.907-920.

Heiland, G., (1961), “Photoconductivity of Zinc Oxide”, Journal of Physics and Chemistry of Solids, vol. 22, 227 – 234.

Heiland, G., Mollwo, E., and Stöckmann, F., (1959), “Electronic Processes in Zinc Oxide,” *Solid State Physics*, **8** pp 191-323.

Hodges Jr., R.R., (2000), “Distributions of hot oxygen for Venus and Mars”, Journal of Geophysical Research, vol. 105, No. E3, pp. 6971-6981, 25 March 2000.

Hoflund, G.B., Weaver, J.F., (1994), “Performance characteristics of a hyperthermal oxygen atom generator,” Measurement Science and Technology, vol. 5, no. 3, pp.201-204.

Hong, Y.W., Kim, J.H., (2004), “Impedance and admittance spectroscopy of Mn_3O_4-doped ZnO incorporated with Sb_2O_3 and Bi_2O_3”, Ceramics International, vol. 30, pp. 1307-1311.

Huang, J.C.A., Hsu, H.S., (2005), “Inspection of magnetic semiconductor and clustering structure in CoFe-doped ZnO films by bias-dependent impedance spectroscopy”, Applied Physics Letters, vol. 87, 132503.

Hucknall, D.J., Morris, A., (2003), “Vacuum Technology”, The Royal Societey of Chemistry, ISBN 0-85404-651-8.

Jacob, A., (1975), “Detection of Atomic Oxygen and Atomic Hydrogen Beams by Semiconductors,” Journal of Applied Physics, Vol. 46, number 12, pp 5116-5121.

Jayadev Dayan, N., Sainkar, S.R., Karekar, R.N., Aiyer, R.C., (1998), “Formulation and characterization of ZnO:Sb thick-film gas sensors”, Thin Solid Films 325, pp.254-258.

Jose, J., Khadar, M.A., (2001), “Role of grain boundaries on the electrical conductivity of nanophase zinc oxide”, Materials Science and Engineering A304–306, 810–813

Kleiman, J., Iskanderova, Z., Gudimenko, Y., Horodetsky, S., (2003), “Atomic oxygen beam sources: a critical overview”, Proc. 9th Int. Symposium on Materials in a Space Environment, ESA SP-540, pp.313-324.

Kim, J., Nagy, A.F., Fox, J.L., Cravens, T.E., (1998), ‘Solar cycle variability of hot oxygen at Mars”, Journal of Geophysical Research, vol. 103, No. A12, pp.29,339-29,342.

Kohl, D., (1996), “Fundamentals and New Applications of Semiconductor Gas Sensors”, Le Vide science, technique et applications No. 279.

Komiya, S., et al., (1979), “Direct-molecular-beam method for mass selective outgassing rate measurement”, Proc. 25th Amer. Vac. Symp., J. Vac. Scie and Technol, Volume 16, p. 689.

Kopitkovas, G., Lippert, T., David, C., Wokaun, A., Gobrecht, J., (2004), “Surface micromachining of UV transparent materials”, Thin Solid Films 453 –454, pp. 31–35.

Kutzner, K., Wietzke, I., (1972), “Method for evaluating the degassing rates”, Vakuum-Technik, page 21, (in german).

Kudryavstev, N.N., Maznar,. O.A., Sukhov, A.M., (1994), “Generation of atomic oxygen beams (review)” Instruments and Experimental Techniques, Vol. 37, no. 1, part 1, pp.16-26.

Langmuir, I., (1918), “The Adsorption of Gases on Plane Surfaces of Glass, Mica and Platinum,” Journal of the American Chemical Society, 40, pp 1361-1403.

Lee, J., Hwang, J.H., Mashek, J.J., Mason, T.O., Miller, A.E., Siegel, R.W., (1995), “Impedance spectroscopy of grain boundaries in nanophase ZnO”, J. Mater. Res, vol. 10, no. 9, pp. 2295-2300.

Leger, L.J., Visentine, J.T., (1986), “Protecting Spacraft from Atomic Oxygen”, Aerospace America 24, 32.

Livshits, A.I., Gutman, E.E., Myasnikov, I.A., (1981), “Measurement of the Atomic Oxygen Profile in the Lower Thermosphere by the Method of Semiconducting Detectors”, 0010-9525/81/1903-0290807.50, Plenum Publishing Coorporation.

Masouka, F., Ooba, K., Sasaki, H., Endo, H., Chiba, S., Maeda, K., Yoneyama, H., Niikura, I., Kashiwaba, Y., (2006), “Applicability of ZnO single crystals for ultraviolet sensors”, Phys. Stat. Sol., (c) 3, No. 4, 1238-1241.

McKelvey, J., (1966), “Solid-State and Semiconductor Physics”, Harper & Row Publishers.

Mead, C.A., (1965), “Surface Barriers on ZnSe and ZnO,” Physics Letters, vol. 18, no. 3, pp 218.

Meier, M., (1994), “Crystallite Size Measurement using X-Ray Diffraction”, Department of Chemical Engineering and Materials Science Mike Meier University of California, Davis, USA. Source: *www.matsci.ucdavis.edu/MatSciLT/ EMS-162L/Files/XRD-CSize1.pdf*

Melnick, D.A., (1957), “Zinc Oxide Photoconduction, an Oxygen Adsorption Process”, Journal of Chemical Physics, No. 26, 1136.

Messer, G., Treitz, N., (1977), “Sensitive mass-selective outgassing measurements on baked stainless steel and copper samples”, Proceedings of the 7th International Vacuum Congress (Vienna), p.223.

Miller, S.K.R., Banks, B.A., Waters, D.L., (2008), “Investigation into the Differences Between Atomic Oxygen Erosion Yields of Materials in Ground-Based Facilities and LEO”, High Performance Polymers, Vol. 20, No. 4-5, pp. 523-534.

Minton, T. K., (1995), “Protocol for Atomic Oxygen Testing of Materials in Ground-Based Facilities, Version Number 2”, JPL Publication 95-17, September 1995.

Mizushima, S., (2004), “Determination of the amount of gas adsorption on SiO2/Si(100) surfaces to realize precise mass measurement”, Institute of Physics Publishin, Metrologia 4, pp.137-144.

Morrison, S.R., (1955), “Surface Barrier Effects in Adsorption, Illustrated by Zinc Oxide,” Advances in Catalysis, 7, pp 259-301.

Moseley, P.T., Tofield, B.C., (1985), “Semiconductor Gas Sensors”, Materials Science and Technology, Vol.1, pp. 505-509.

Mukhopadhyay, K., Mitra, P., Chattopadhyay, D., Maiti, H.S., (1996), “Influences of Frabrication Techniques and Doping on Hidrogen Sensitivity of Zinc Oxide Sensors”, Journal of Materials Science Letters, v 15, n 5, p 431-433.

Myasnikov, I.A., Gutman, E.E., (1986), “Physico-Chemical Basis for Detection of Active Particles and Gas Molecules by Means of Semiconductor Metal Oxides”, Proc. Of the Second Intl. Meeting on Chemical Sensors, Bordeaux.

Nahr, H., Hoinkes, H. and Wilsch, H., (1971), “New Method for the Detection of Atomic Oxygen Beams,” The Journal of Chemical Physics, 54, no. 7, pp 3022-3025.

Neumann, G., (1981), “On the Defect Structure of Zinc-Doped Zinc Oxide,” Physica Status Solidi B – Basic Research, 105, pp 605-612.

Novak, S., Pisarkiewicz, T., (1992), “Thick and thin heaters for gas sensors”, International Conference of Microelectronics, vol. 1783.

Nunes, P., Fortunato, E., Martins, R., (2001), “Thin film combustible gas sensors based on zinc oxide”, Transport and Microstructural Phenomena in Oxide Electronics Symposium, Materials Research Society Symposium Proceedings Vol.666, 2001, pF5.2.1-6, ISBN: 1 55899 602 8.

O’Hanlon, J.F.,(1980), “A User’s Guide to Vacuum Technology”, John Wiley & Sons, Inc., ISBN 0-471-01624-1.

Ohashi, N.; Kataoka, K., Ohgaki, T., Miyagi, T., Haneda, H., Morinaga, K., (2003), "Synthesis of zinc oxide varistors with a breakdown voltage of three volts using an intergranular glass phase in the bismuth-boron-oxide system", Applied Physics Letters, Volume 83, Issue 23, id. 4857.

Osborne, J.J., (1999), “A Study of Semiconductor-Based Atomic Oxygen Sensors for Ground and Satellite Applications”, Doctoral Thesis presented at the University of Southampton.

Osborne, J.J., Harris, I.L., Roberts, G.T., Chambers, A.R., (2001), “Satellite and rocket-borne atomic oxygen sensor techniques”, Review of Scientific Instruments, Volume 72, Number 11.

Osborne, J.J Roberts, G.T Chambers, A.R., Gabriel, S.B., (1999), "Initial results from ground-based testing of an atomic oxygen sensor designed for use in Earth

orbit", Review of Scientific Instruments, vol. 70, no. 5, May 1999, pp. 2500-2506.

Oura, K, Lifshits, V.G., Saranin, A.A., Zotov, A.V., Katayama, M., (2003), “Surface Science, An Introduction”, Springer, ISBN-10: 3540005455.

Packirisamy, S., Schwam, D., Litt, M.H., (1995), “Atomic oxygen resistant coatings from low earth orbit space structures”, Journal of Materials Science, Vol. 30, pp. 308-320.

Prudenziati, M., Morten, B.; De Cicco, G. (1995), “Thick Film Gas Sensors”, Proceedings of the First European School on Sensors (ESS'94). Sensors for Domestic Applications, pp. 24-36.

Reddy, M.R., (1995), “Review effect of low earth orbit atomic oxygen spacecraft materials”, J. Mater. Sci. 30, 281.

Royal, T.M., Wortman, J.J., Monteich, L.K., (1968), “An Investigation to Thin Film Oxygen Partial Pressure Sensors”, NASA CR-1182, Research Triangle Institute.
Roth, A. (1982), “Vacuum Technology”, Elsevier Science Publishers, ISBN 0-444-86027-4.

Routbort, J.L., Tomlins, G.W., (1995), “Atomic Transport of Oxygen n Nonstoichiometric Oxides”, Radiation Effects and Defects in Solids, Vol. 137, pp. 233-238.

Sahay, P.P., Tewari, S., Jha, S., Shamsuddin, M.,(2005), “Sprayed ZnO thin films for ethanol sensors”, Journal of Materials Science, vol. 40, pp. 4791-4793.

Seitz, M., Hampton, F., Richmond, W., (1983), “Influence of chemisorbed oxygen on the AC electrical behavior of polycrystalline ZnO”, Advances in Ceramics, vol. 7, Additives and Interfaces in Electronic Ceramics, ed. Yan, M.F., and Heuer, A.H., The American Ceramic Society, 1983, pp. 60-70.

Shao, R., Kalinin, S.V., Bonnell, D.A., (2003), “Local impedance imaging and spectroscopy of polycrystalline ZnO using contact atomic force microscopy”, Applied Physics Letters, volume 82, number 12, 24 March 2003, pp. 1869-1871.

Smith, R.A., (1964), “Semiconductors”, Cambridge University Press, Cambridge, UK.

Schwesinger, N., Bartsch, H., Moller, F., “Deposition of thick Zinc Oxide Films with a high resistivity“, SPIE Vol. 2639, pp. 315-323, 0-8194-2005-0, 2005.

Sizeland, E., (1994), “An investigation into the production process controlling the manufacture and operation of thick-film Tin (IV) Oxide gas sensitive devices”, Doctoral Thesis presented at the University of Southampton.

Slanger, T.G., Cosby, P.C., Huestis, D.L., Bida, T.A., (2001), “Discovery of the Atomic Oxygen Green Line in the Venus Night Airglow”, Science, vol. 291, 19 January 2001.

Smith, R.A., (1964), “Semiconductors,” Cambridge University Press, Cambridge, UK.

Soares, J.W., Steeves, D.M., Ziegler, D., DeCristofano, B.S., (2006), “Surface modification of nanocrystalline zinc oxide for bio-sensing Applications”, Nanomaterial Synthesis and Integration for Sensors, Electronics, Photonics, and Electro-Optics, Proceedings of SPIE, vol. 6370.

Somorjai, G.A., (1972), “Principles of Surface Chemistry,” Prentice-Hall, USA.

Tagawa, M., Ema, T., Kinoshita, H., Umeno, M., Ohmae, N., and Minton, T. K., (1997), “Oxidation of Room Temperature Silicon (001) Surfaces in a Hyperthermal Atomic Oxygen Beam,” in Proceedings of the 7th International Symposium on Materials in a Space Environment, Toulouse, France, pp 225-229, 16th-20th June 1997. ESA SP-399.

Takahashi, Y., Kanamori, M., Kondoh, A., Minoura, H., Ohya, Y., (1994), Jpn. Journal of Applied Physics, Vol. 33, pp. 6611-6615, part 1, No. 12A.

Thrush, B.A., (1967), “Atom Reactions in Flow Tubes”, Science, Vol. 156, pp. 470-473.

Tribble, Alan C, (1995) “The Space Environment: Implications for Spacecraft Design”, Princeton University Press.

Trivikrama Rao, G.S., Trivikrama Rao, D., (1999), “Gas sensitivity of ZnO based thick film sensor to NH_3 at room temperature”, Sensors and Actuators B, vol. 55, pp. 166-169.

Valer, J.C., (2000), “A Study of the Chemistry Between Fast Atomic Oxygen and Silver-Coated QCM Crystals”, Thesis for the Masters in Aerospace Engineering Degree presented at the University of Tennessee Space Institute.

Varfolomeev, A.E., Eryshkin, A.V., Malyshev, V.V., Razumov, A.S., Yakimov, S.S., (1994), “A Study of the Sensitivity of ZnO-based Sensors to CO, H_2, NH_3, and AsH_3”, Journal of Analytical Chemistry, Vol. 52, No. 1, pp.56-58.

Viereck, R.A., Murad, E.; Green, B.D., Joshi, P., Pike, C.P., Hieb, R., Harbaugh, G., (1991), “Origin of the Shuttle Glow”, Nature, v 354, n 6348, p 48-50I, ISSN: 0028-0836.

Viereck, R.A., Mende, S.B., Murad, E., Swenson, G.R., Pike, C.P., Culbertson, F.L., Springer, R.C., (1992), “Spectral characteristics of Shuttle glow”, Geophysical Research Letters, v 19, n 12, 19 June 1992, p 1219-22, ISSN: 0094-8276.

Viswanath, R.N., Ramasamy, S.N., (2001), “Impedance Spectroscopy Studies of Nanostructured ZnO Based Varistor Materials”, Materials Transactions, vol. 42, no. 8, pp. 1647-1652.

Wang, Y., Chen, J., Wu, X., (2001), “Preparation and gas-sensing properties of perovskite-type $SrFeO_2$ oxide”, Mater. Lett. 49, pp 361-364.

Weihs, B. and van Eesbeek, M., (1994), “Secondary VUV Erosion Effects on Polymers in the ATOX Atomic Oxygen Exposure Facility,” in Proceedings of the 6th International Symposium on Materials in a Space Environment, ESTEC, Noordwijk, The Netherlands, pp 277-283, 19th-23rd Sep. 1994. ESA SP-368.

Shen, W., Zhao, Y., Zhang, C., (2005), “The preparation of ZnO based gas-sensing thin films by ink-jet printing method”, Thin Solid Films, Vol 483, pp. 382-

387.

Tuomisto, F., Saarinen, K., Look, D.C., Farlow, G.C., (2005), “Introduction and recovery of point defects in electron-irradiated Zinc Oxide”, Physics Review B 72, 085206.

Wagh, M.S., Jain, G.H., Patil, D.R., Patil, S.A., Patil, L.A., (2006), “Modified zinc oxide thick film resistors as NH_3 gas sensor”, Sensors and Actuators B vol. 115, pp. 128–133.

White, N.M., Turner, J.D., (1996), “Thick-film sensors: past, present, and future”, Meas. Sci. Technology, vol. 8, pp. 1-20.

White, C.B., Valer, J.C., Chambers, A.R., Roberts, G.T., (2006), “Atomic Oxygen Source Calibration Issues: A Universal Approach”, 7th International Conference on “Protection of Materials and Structures from Space Environment”, Toronto, Canada, Springer, ISBN-10 1402042817.

White, C.B., Rao, J., Roberts, G.T., Chambers, A.R., Lawson, K.J., Nichols, J.R., (2003), “The Development of Carbon-Based Sensors for the Measurement of Atomic Oxygen”, Proceedings of the 9th International Symposium on Materials in a Space Environment, The Netherlands, ESA Publication SP-540.

Wolan, J.T., Hoflund, G.B., (1999), “Chemical and Structural Alterations Induced at Kapton Surfaces by Air Exposures Following Atomic Oxygen or 1 keV Ar+ Treatments”, J. Vac. Sci. Technol.A, Vol. 17, No. 2, pp. 662-664.

Wortman, J.J., Harrison, J.W., Honbarrier, H.L., Jen, J., (1972), “Thin film oxygen partial pressure sensor”, Res. Triangle Inst., Res. Triangle Park, NC, USA, NASA-CR-1941.

Yamazaki, T., Wada, S., Noma, T., Suzuki, T., (1993), “Gas sensing properties of ultrathin zinc oxide films”, Sensors and Actuators B, 13-14, pp. 594-595.